

Advances in Complex Systems, Vol. 5, No. 2 (2002) 1–144
© World Scientific Publishing Company

**CELLULAR AUTOMATA AND
LATTICE BOLTZMANN TECHNIQUES:
AN APPROACH TO MODEL AND
SIMULATE COMPLEX SYSTEMS**

BASTIEN CHOPARD,* ALEXANDRE DUPUIS,
ALEXANDRE MASSELOT and PASCAL LUTHI
*Computer Science Department, University of Geneva,
24 rue General-Dufour, 1211 Geneva 4, Switzerland*
**Bastien.Chopard@cui.unige.ch*

Received 00 Month Year
Revised 00 Month Year

We discuss the cellular automata approach and its extensions, the lattice Boltzmann and multiparticle methods. The potential of these techniques is demonstrated in the case of modeling complex systems. In particular, we consider applications taken from various fields of physics, such as reaction-diffusion systems, pattern formation phenomena, fluid flows, fracture processes and road traffic models.

Keywords: Cellular automata; lattice Boltzmann method; complex systems simulations.

1. The Cellular Automata Approach

The computational science community has always been faced with the challenge of bringing efficient numerical tools to solve problems of increasing difficulty. Nowadays, a lot of effort is devoted to investigate and understand the so-called complex systems, and to simulate all kinds of phenomena originating from the interaction of many components.

Cellular automata turns out to be a very fruitful approach to address many aspects of complex systems. They provide a framework to understand complexity, untractability, undecidability, but also offer a very efficient numerical way to model and simulate specific phenomena for which more traditional computational techniques are hardly applicable.

The goal of this article is to provide the reader with a selection of possible applications of the cellular automata approach. It is mostly based on the research made by the authors and co-workers and has not the ambition of being an exhaustive description of the field, or an attempt to establish the pros and the cons of this approach compared to other numerical tools. Yet, many bibliographical references are given in order to help in placing this work in the large framework of topics it addresses.

We try to make this paper self-consistent and we hope it will give the essential ingredients to have a in-depth understanding of the powerfulness of the cellular automata approach in very many fields of science. We invite the reader to consult the Web site <http://cui.unige.ch/~chopard/CA/Animations/img-root.html> in order to view a short movie of several of the models discussed in this review.

1.1. *Introduction*

Cellular automata (often termed CA) are an idealization of a physical system in which space and time are discrete. In addition, the physical quantities (or state of the automaton) take only a finite set of values. Since it was invented by von Neumann in the late 1940s, the cellular automata approach has been applied to a large range of scientific problems^{a,b} (see for instance 50, 61, 90, 107, 112, 137, 139 and 5, 6, 16, 33, 155, 165, 169, 186, 189).

The original motivation of von Neumann was to extract the abstract mechanisms leading to self-reproduction of the biological organisms [22]. In other words the problem is to devise a system having the capability (and the recipe) to produce another organism of equivalent complexity with only its own ressource.

Following the suggestions of S. Ulam [174], von Neumann addressed this question in the framework of a fully discrete universe made up of cells. Each cell is characterized by an internal state, which typically consists of a finite number of information bits. Von Neumann suggested that this system of cells evolves, in discrete time steps, like simple automata which only know of a simple recipe to compute their new internal state. The rule, determining the evolution of this system is the same for all cells and is a function of the states of the neighbor cells. Similarly to what happens in any biological system, the activity of the cells takes place simultaneously. However, the same clock drives the evolution of each cell and the updating of the internal state of each cell occurs synchronously.

Such a fully discrete dynamical systems (cellular space) as invented by von Neumann are now referred to as a *cellular automaton*.

After the work of von Neumann, other authors have followed the same line of research and nowadays the problem is still of interest [146] and has led to interesting developments for new computer architectures [111].

Many other applications of CA's to physical science have been considered. In 1970, the mathematician John Conway proposed his famous *game of life* [71]. His motivation was to find a simple rule leading to complex behaviors. He imagined a two-dimensional square lattice, like a checkerboard, in which each cell can be either alive (state one) or dead (state zero). The updating rule of the game of life is as follows: a dead cell surrounded by exactly three living cells gets back to life; a living cell surrounded by less than two or more than three neighbors dies of isolation

^aMinnesota IMA cellular automata bibliography. <http://www.ima.umn.edu/bibtex/ca.bib>.

^bSanta-fe cellular automata bibliography. <ftp://alife.santafe.edu/pub/topics/cas/ca-faq.bib>.

or overcrowdedness. Here, the surrounding cells corresponds to the neighborhood composed of the four nearest cells (north, south, east and west), plus the four second nearest neighbors, along the diagonals. It turns out that the game of life automaton has an unexpectedly rich behavior. Complex structures emerge out of a primitive “soup” and evolve so as to develop some skills.

As for von Neumann’s rule, the game of life is a cellular automata capable of universal computations: it is always possible to find an initial configuration of the cellular space reproducing the behavior of any electronic gate and, thus, to mimic any computation process. Although this observation has little practical interest, it is very important from a theoretical point of view since it assesses the ability of CAs to be a non-restrictive computational technique.

A very important feature of CAs is that they provide simple models of complex systems. They exemplify the fact that a collective behavior can emerge out of the sum of many, simply interacting, components. Even if the basic and local interactions are perfectly known, it is possible that the global behavior obeys new laws that are not obviously extrapolated from the individual properties, as if the whole is more than the sum of all the parts. This properties makes cellular automata a very interesting approach to model physical systems and in particular to simulate complex and non-equilibrium phenomena.

The studies undertaken by S. Wolfram in the 1980s [188, 189] clearly establishes that a CA (the famous Wolfram’s rules) may exhibits many of the behaviors encountered in continuous systems, yet in a much simpler mathematical framework. A further step is to recognize that CAs are not only behaving similarly to some dynamical processes, they can also represent an actual model of a given physical system, leading to macroscopic predictions that could be checked experimentally. This fact follows from statistical mechanics which tells us that the macroscopic behavior of many systems is quite disconnected from its microscopic reality and that only symmetries and conservation laws survives the change of observation level, it is well known that the flows of a fluid, a gas or even a granular media are very similar at a macroscopic scale, in spite of their different microscopic nature.

An interesting example is the FHP fluid model proposed by Frisch, Hasslacher and Pomeau in 1986 [67] which can be viewed as a fully discrete molecular dynamics and yet behaves as predicted by the Navier–Stokes equation when the observation time and length scales are much larger than the lattice and automaton time step.

Cellular automata fluids like the FHP model (or lattice gas automata (LGA) as these models are often termed), cannot directly compete with standard computational fluid dynamics techniques for high Reynolds flows. However, they have been very successful in modeling complex situations for which traditional computing techniques are hardly applicable. Flows in porous media [1, 26, 75], immiscible flows and instabilities [15, 74, 152], spreading of a liquid droplet and wetting phenomena [33, 52], granular flows [99, 134] microemulsion [13] erosion and transport problems [33, 181] are some examples pertaining to fluid dynamics.

Other physical situations, like pattern formation, reaction-diffusion processes [17, 39, 45], nucleation-aggregation growth phenomena, traffic process [41, 184, 185] are very well suited to the cellular automata approach.

The cellular automata paradigm presents some weaknesses inherent to its discrete nature. Lattice Boltzmann (LB) models have been proposed to remedy some of these problems, using real-valued states instead of Boolean variables. It turns out that LB models are indeed a very powerful approach which combines numerical efficiency with the advantage of having a model whose microscopic components are intuitive.

This paper is organized as follows. In the remainder of Sec. 1 a precise definition of a cellular automata is given. We present some argument to justify the approach and, finally, the advantages and drawbacks of the method are outlined. In Sec. 2, a sampler of CA rules are presented in order to illustrate the methodology and give an account of the large variety of possible applications. Section 3 shows, for the case of a fluid, how to derive rigorously the macroscopic behavior of a cellular automata model, starting from its Boolean dynamics. Section 4 discusses the lattice Boltzmann (LB) method and presents an application to compute deposition patterns in snow transport. Section 5 is devoted to reaction-diffusion systems and some examples of pattern formations. In Sec. 6 we introduce multiparticles models that concile some of the advantages of the CA and LB approaches. Finally, Sec. 7 proposes a LB model for wave propagation in heterogeneous media, as well as its application to model a fracture process and wave localization.

1.2. *Definition*

In order to give a definition of a cellular automaton, we first present a simple example. Although it is very basic, the rule we discuss here exhibits a surprisingly rich behavior. It was proposed initially by Edward Fredkin in the 1970s [7] and is defined on a two-dimensional square lattice.

Each site of the lattice is a cell which is labeled by its position $\vec{r} = (i, j)$ where i and j are the row and column indices. A function $\psi_t(\vec{r})$ is associated to the lattice to describe the state of each cell at iteration t . This quantity can be either 0 or 1.

The cellular automata rule specifies how the states ψ_{t+1} are to be computed from the states at iteration t . We start from an initial condition at time $t = 0$ with a given configuration of the values $\psi_0(\vec{r})$ on the lattice. The state at time $t = 1$ will be obtained as follows

- (1) Each site \vec{r} computes the sum of the values $\psi_0(\vec{r}')$ on the four nearest neighbor sites \vec{r}' at north, west, south and east. The system is supposed to be periodic in both i and j directions (like on a torus) so that this calculation is well defined for all sites.
- (2) If this sum is even, the new state $\psi_1(\vec{r})$ is 0 (white) and, else, it is 1 (black).

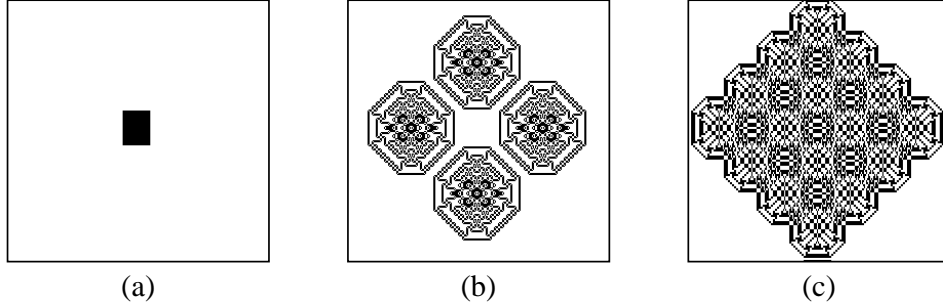


Fig. 1. The \oplus rule on a 256×256 periodic lattice. (a) initial configuration. (b) and (c) configurations after $t_b = 93$ and $t_c = 110$ iterations, respectively.

The same rule (steps 1 and 2) is repeated over to find the states at time $t = 2, 3, 4, \dots$

From a mathematical point of view, this cellular automata parity rule can be expressed by the following relation:

$$\psi_{t+1}(i, j) = \psi_t(i + 1, j) \oplus \psi_t(i - 1, j) \oplus \psi_t(i, j + 1) \oplus \psi_t(i, j - 1), \quad (1.1)$$

where the symbol \oplus stands for the exclusive OR logical operation. It is also the sum modulo 2: $1 \oplus 1 = 0 \oplus 0 = 0$ and $1 \oplus 0 = 0 \oplus 1 = 1$.

When this rule is iterated, very nice geometric patterns are observed, as shown in Fig. 1. This property of generating complex patterns starting from a simple rule is generic of many cellular automata rules. Here, complexity results from some spatial organization which builds up as the rule is iterated. The various contributions of successive iterations combine together in a specific way. The spatial patterns that are observed reflect how the terms are combined algebraically.

This example shows that despite the simplicity of the local rule, the global behavior of a CA model can be quite complex. In the present case, the mechanism yielding these complex patterns can be unraveled by working out how successive iterations combine several copies of the initial configuration, all shifted by a different amount [33].

Based on this example we now give a definition of a cellular automata. Formally a cellular automata is made of

- (i) A regular lattice of cells covering a portion of a d -dimensional space.
- (ii) A set $\Phi(\vec{r}, t) = \{\Phi_1(\vec{r}, t), \Phi_2(\vec{r}, t), \dots, \Phi_m(\vec{r}, t)\}$ of Boolean variables attached to each site \vec{r} of the lattice and giving the local state of each cell at the time $t = 0, 1, 2, \dots$
- (iii) A rule $\mathbf{R} = \{R_1, R_2, \dots, R_m\}$ which specifies the time evolution of the states $\Phi(\vec{r}, t)$ in the following way

$$\Phi_j(\vec{r}, t + \Delta_t) = R_j(\Phi(\vec{r}, t), \Phi(\vec{r} + \vec{\delta}_1, t), \Phi(\vec{r} + \vec{\delta}_2, t), \dots, \Phi(\vec{r} + \vec{\delta}_q, t)) \quad (1.2)$$

where $\vec{r} + \vec{\delta}_k$ designate the cells belonging to a given neighborhood of cell \vec{r} .

The example discussed in the previous section is a particular case in which the state of each cell consists of a single bit $\Phi_1(r, t) = \psi_t(\vec{r})$ of information and the rule is the addition modulo 2.

In the above definition, the rule \mathbf{R} is identical for all sites and is applied simultaneously to each of them, leading to a synchronous dynamics. It is important to notice that the rule is *homogeneous*, that is it cannot not depend explicitly on the cell position \vec{r} . However, spatial (or even temporal) inhomogeneities can be introduced anyway by having some $\Phi_j(\vec{r})$ systematically in some given locations of the lattice to mark particular cells on which a different rule apply. Boundary cells are a typical example of spatial inhomogeneities. Similarly, it is easy to alternate between two rules by having a bit which is 1 at even time steps and 0 at odd time steps.

The neighborhood (i.e. the spatial region around each cell used to compute the next state) is usually made of the adjacent cells of the central cell. It is often restricted to the nearest or next to nearest neighbors, otherwise the complexity of the rule is too large. For a two-dimensional cellular automaton, two neighborhoods are often considered: the von Neumann neighborhood which consists of a central cell (the one which is to be updated) and its four geographical neighbors North, West, South and East. The Moore neighborhood contains, in addition, the second nearest neighbor North-East, North-West, South-East and South-East, that is a total of nine cells.

According to the above definition, a cellular automaton is deterministic. The rule \mathbf{R} is some well defined function and a given initial configuration will always evolve identically. However, as we shall see later, it may be very convenient for some applications to have a certain degree of randomness in the rule. For instance, it may be desirable that a rule selects one outcome among several possible states, with a probability p . Cellular automata whose updating rule is driven by some external probabilities are called *probabilistic* cellular automata. On the other hand, those which strictly comply with the definition given above, are referred to as *deterministic* cellular automata.

Probabilistic cellular automata are a very useful generalization because they offer a way to adjust the parameters of a rule in a continuous range of values, despite the discrete nature of the cellular automata world. This is very convenient when modeling physical systems in which, for instance, particles are annihilated or created at some given rate.

1.3. CA as a model of the physical world

A natural way to describe a physical system is to propose a model of what we think is happening. During this process we usually retain only the ingredients we believe to be essential in order to capture the behavior we are interested in. Using an appropriate mathematical machinery, such a model can then be expressed in terms a set of equations whose solution gives the desired answers on the system. The description in terms of equations is very powerful and corresponds to a rather high

level of abstraction. For a long time, this methodology has been the only tractable way for scientists to address a problem.

Another approach which has been made possible by the advent of fast computers is to stay at the level of the model. The idea is that all the information is already contained in the model and that a computer simulation will be able to answer any possible question on the system by just running the model for some time. Thus there is no need to use a complicated mathematical tool to obtain a high level of description. We just need to express the model in a way which is suitable to an effective computer implementation. In the framework of CAs, this last step is usually very intuitive and requires little development time.

The degree of reality of the model depends on the level of description we expect. When we are interested in the global or macroscopic properties of a system (and this is the case here), we already mentioned that, except for the symmetries and conservation laws, the microscopic details are often not relevant. It is therefore a clear advantage to invent a much simpler microscopic reality, which is more appropriate to our numerical means of investigation.

A cellular automata model can be seen as a fictitious universe which has its own microscopic reality but, nevertheless, has the same macroscopic behavior as the real system we are interested in. The example we shall give in the next section will illustrate this statement.

1.4. *Limitations, advantage, drawbacks and extension*

Modeling a system at a microscopic level of description has significant advantages. The interpretation of the cellular automata dynamics in terms of simple microscopic rules offers a very intuitive and powerful approach to model phenomena that are very difficult to include in more traditional approaches (such as differential equations). For instance, boundary conditions are often naturally implemented in a cellular automata model because it has a natural interpretation at this level of description (e.g. particles bouncing back on an obstacle). For instance, the phenomena of wetting of a solid substrate by a spreading liquid illustrates the difficulty of defining appropriate boundary conditions at the level of the Navier–Stokes equation. Yet, in the framework of a CA description, this can be achieved in a simple way [33].

Numerically, an advantage of the CA approach is its simplicity and its adequacy to computer architectures and parallel machines. In addition, working with Boolean quantities prevents numerical instabilities since an exact computation is made. There is no truncation or approximation in the dynamics itself. Finally, a CA model is an implementation of an N-body system where all correlations are taken into account, as well as spontaneous fluctuations arising in a system made up of many particles.

On the other hand, cellular automata models have several drawbacks related to their fully discrete nature. An important one is the statistical noise requiring a

systematic averaging processes. Another one is the limited flexibility for adjusting parameters of a rule in order to describe a wider range of physical situations.

At the end of the 1980s, McNamara and Zanetti [121] Higuera, Jimenez and Succi [83] have shown the advantage of extending the Boolean dynamics of the automaton to directly work on real numbers representing, somehow, the probability for a cell to have a given state. This approach, called the lattice Boltzmann (LB) method, is numerically much more efficient than the Boolean dynamics and provides a new computational model much more appropriate to simulate high Reynolds flows and many other relevant applications (for instance glacier flow [4] and fracture processes). On the other hand, the LB approach re-introduces the risk of numerical instabilities and, also, requires some hypotheses of factorization of the joint probability in order to write the interaction. We will return to this approach in Sec. 4.

Another generalization of the original definition of a CA is the multiparticle method in which the number of state of each cell is infinite so that an arbitrary number of particles can stay simultaneously at each site. This offers much more flexibility to tune the parameter of the rule and reduces considerably the statistical noise. A multiparticle model goes in the same direction as the LB models but it does not need a factorization assumption and is not sensitive to numerical instability. Unfortunately, as explained in Sec. 7, it requires more implementation effort than the LB approach and is also numerically less efficient.

Finally, we should remark that the cellular automata approach is not a rigid framework but should allow for many extensions according to the problem at hand. The CA methodology is a philosophy of modeling where one seeks a description in terms of simple but essential mechanisms. Its richness and interest comes from the microscopic contents of its rule for which there is, in general, a clear physical or intuitive interpretation of the dynamics directly at the level of the cell.

2. Examples of Simple Rules

In this section we consider several CA rules in order to illustrate the ideas we have introduced in Sec. 1. Although the rules we will present here have clear physical contents, some of them should be considered as toy models because their ability to describe the macroscopic behavior of a real physical system does not withstand detailed analysis. However, our goal is to present the flavor of the CA approach but not to give a proof that the rule we propose is rigorously related to a given process.

2.1. *A growth model*

A natural class of cellular automata rules consists of the so-called *majority rules*. The updating selects the new state of each cell so as to conform to the value currently held by the majority of the neighbors. Typically, in these majority rules, the state is either 0 or 1.

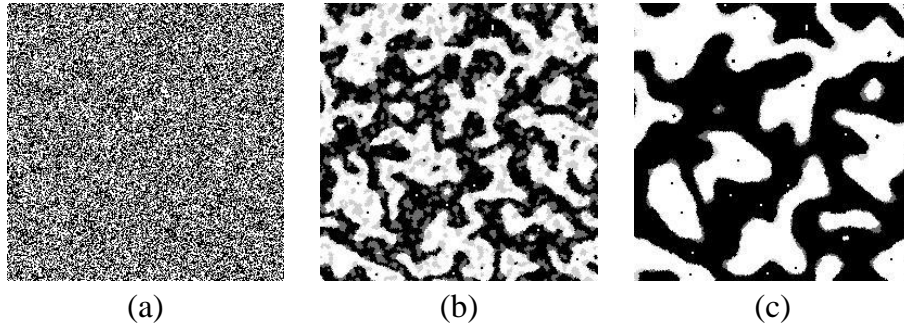


Fig. 2. Evolution of the annealing rule. The inherent “surface tension” present in the rule tends to separate the black phases $s = 1$ from the white phase $s = 0$. The snapshots (a), (b) and (c) correspond to $t = 0$, $t = 72$ and $t = 270$ iterations, respectively. The extra gray levels indicate how “capex” have been eroded and “bays” filled: dark gray shows the black regions that have been eroded during the last few iterations and light gray marks the white regions that have been filled.

A very interesting behavior is observed with the twisted majority rule proposed by G. Vichniac [176]: in two-dimensions, each cell considers its Moore neighborhood (i.e itself plus its eight nearest neighbors) and computes the sum of the cells having a value 1. This sum can be any value between 0 and 9. The new state $s_{ij}(t + 1)$ of each cell is then determined from this local sum, according to the following table

$$\begin{array}{rcccccccccc} \text{sum}_{ij}(t) & 0 & 1 & 2 & 3 & 4 & 5 & 6 & 7 & 8 & 9 \\ s_{ij}(t + 1) & 0 & 0 & 0 & 0 & 1 & 0 & 1 & 1 & 1 & 1. \end{array} \quad (2.1)$$

As opposed to the plain majority rule, here, the two middle entries of the table have been swapped. Therefore, when there is a slight majority of 1 around a cell, it turns to 0. Conversely, if there is a slight majority of 0, the cell becomes 1.

Surprisingly enough this rule describes the interface motion between two phases, as illustrated in Fig. 2. Vichniac has observed that the normal velocity of the interface is proportional to its local curvature, as required by the Allen–Cahn [77] equation. Of course, due to its local nature, the rule cannot detect the curvature of the interface directly. However, as the rule is iterated, local information is propagated to the nearest neighbors and the radius of curvature emerges as a collective effect.

This rule is particularly interesting when the initial configuration is a random mixture of the two phases, with equal concentration. Otherwise, some pathological behaviors may occur. For instance, an initial square of 1’s surrounded by zero’s will not evolve: right angles are not eroded but stable structures.

2.2. Ising-like dynamics

The Ising model is extensively used in physics. Its basic constituents are spins s_i which can be in one of two states: $s_i \in \{-1, 1\}$. These spins are organized on a regular lattice in d -dimensions and coupled in the sense that each pair (s_i, s_j) of neighbor

spins contributes an amount $-Js_i s_j$ to the energy of the system. Intuitively, the dynamics of such a system is that a spin flips ($s_i \rightarrow -s_i$) if this is favorable in view of the energy of the local configuration.

Vichniac [176], in the 1980s, has proposed a CA rule, called the Q2R, simulating the behavior of an Ising spin dynamics. The model is as follows:

We consider a two-dimensional square lattice such that each site holds a spin s_i which is either up ($s_i = 1$) or down ($s_i = 0$) (instead of ± 1). The coupling between spins is assumed to come from the von Neumann neighborhood (i.e. north, west south and east neighbors).

In this simple model, the spins will flip (or not flip) during their discrete time evolution according to a local energy conservation principle. This means we are considering a system which cannot exchange energy with its surroundings. The model will be a microcanonical cellular automata simulation of Ising spin dynamics, without a temperature but with a critical energy.

A spin s_i can flip at time t to become $1 - s_i$ at time $t + 1$ if and only if this move does not cause any energy change. Accordingly, spin s_i will flip if the number of its neighbors with spin up is the same as the number of its neighbors with spin down. However, one has to remember that the motion of all spins are simultaneous in a cellular automata. The decision to flip is based on the assumption that the neighbors are not changing. If they are allowed to flip too, (because they obey the same rule), then energy may not be conserved.

A way to cure this problem is to split the updating in two phases and consider a partition of the lattice in odd and even sites (e.g. the white and black squares of a chess-board in 2D): first, one flips the spins located at odd positions, according to the configuration of the even spins. In the second phase, the even sublattice is updated according to the odd one. The spatial structure (defining the two sublattices) is obtained by adding an extra bit b to each lattice site, whose value is 0 for the odd sublattice and 1 for the even sublattice. The flipping rule described earlier is then regulated by the value of b . It takes place only for those sites for which $b = 1$. Of course, the value of b is also updated at each iteration according to $b(t + 1) = 1 - b(t)$, so that at the next iteration, the other sublattice is considered. In two-dimensions, the Q2R rule can be expressed by the following expressions

$$s_{ij}(t + 1) = \begin{cases} 1 - s_{ij}(t) & \text{if } b_{ij} = 1 \text{ and } s_{i-1,j} + s_{i+1,j} + s_{i,j-1} + s_{i,j+1} = 2 \\ s_{ij}(t) & \text{otherwise} \end{cases} \quad (2.2)$$

and

$$b_{ij}(t + 1) = 1 - b_{ij}(t), \quad (2.3)$$

where the indices (i, j) label the Cartesian coordinates and $s_{ij}(t = 0)$ is either one or zero.

The question is now how well does this cellular automata rule perform to describe an Ising model. Figure 3 show a computer simulation of the Q2R rule, starting from an initial configuration with approximately 11% of spins $s_{ij} = 1$ (Fig. 3(a)).

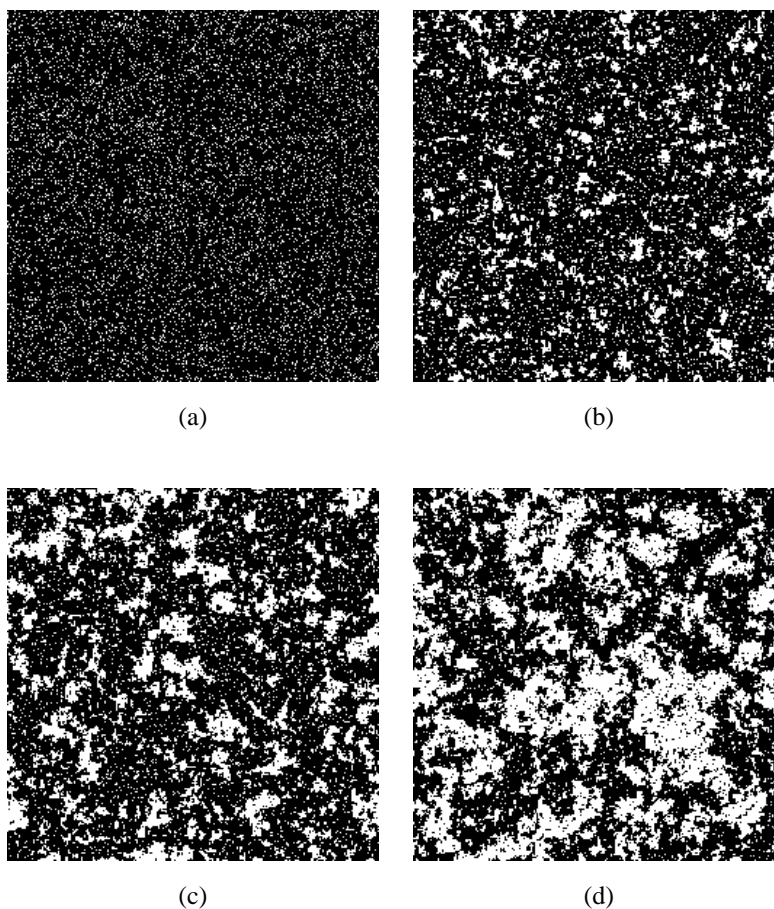


Fig. 3. Evolution of a system of spins with the Q2R rule. Black represents the spins down $s_{ij} = 0$ and white the spins up $s_{ij} = 1$. The four images (a), (b), (c) and (d) show the system at four different times $t_a = 0 < t_b < t_c \gg t_d$.

After a transient phase (Figs. 3(b) and 3(c)), the system reaches a stationary state where domains with “up” magnetization (white regions) are surrounded by domains of “down” magnetization (black regions).

In this dynamics, energy is exactly conserved because that is the way the rule is built. However, the number of spins down and up may vary. In the present experiment, the fraction of spins up increases from 11% in the initial state to about 40% in the stationary state. Since there is an excess of spins down in this system, there is a resulting macroscopic magnetization.

It is interesting to study this model with various initial fractions ρ_s of spins up. When starting with a random initial condition, similar to that of Fig. 3(a), it is observed that, for many values of ρ_s , the system evolves to a state where there is, in the average, the same amount of spin down and up, that is no macroscopic

magnetization. However, if the initial configuration presents a sufficiently large excess of one kind of spins, then a macroscopic magnetization builds up as time goes on. This means there is a phase transition between a situation of zero magnetization and a situation of positive or negative magnetization.

It turns out that this transition occurs when the total energy E of the system is low enough (a low energy means that most of the spins are aligned and that there is an excess of one species over the other), or more precisely when E is smaller than a critical energy E_c . In that sense, the Q2R rule captures an important aspect of a real magnetic system, namely a non-zero magnetization at low energy (which can be related to a low temperature situation) and a transition to a non-magnetic phase at high energy.

However Q2R also exhibits unexpected behavior that are difficult to detect from a simple observation. There is a breaking of ergodicity: a given initial configuration of energy E_0 evolves without visiting completely the region of the phase space characterized by $E = E_0$.

This is illustrated by the following simple 1D example, where a ring of four spins with periodic boundary condition are considered.

$$\begin{aligned}
 t : & \quad 1001 \\
 t + 1 : & \quad 1100 \\
 t + 2 : & \quad 0110 \\
 t + 3 : & \quad 0011 \\
 t + 4 : & \quad 1001 .
 \end{aligned}
 \tag{2.4}$$

After four iterations, the system cycles back to its original state. The configuration of this example has $E_0 = 0$. As we observed, it never evolves to 0111, which is also a configuration of zero energy. This non-ergodicity means that not only is energy conserved during the evolution of the automaton, but also another quantity which partitions the energy surface into independent regions.

2.3. Competition models and cell differentiation

In Sec. 2.1 we have discussed a majority rule in which the cells imitate their neighbors. In some sense, this corresponds to a cooperative behavior between the cells. A quite different situation can be obtained if the cells obey a competitive dynamics. For instance we may imagine that the cells compete for some resources at the expense of their nearest neighbors. A winner is a cell of state 1 and a loser a cell of state 0. No two winner cells can be neighbors and any loser cell must have at least one winner neighbor (otherwise nothing would have prevented it to also win).

It is interesting to note that this problem has a direct application in biology, to study cell differentiation. It has been observed in the development of the drosophila that about 25% of the cells forming the embryo are evolving to the state of neuroblast, while the remaining 75% does not. How can we explain this differentiation and the observed fraction since, at the beginning of the process all cells can be

assumed equivalent? A possible mechanism [109] is that some competition takes place between the adjacent biological cells. In other words, each cell produces some substance S but the production rate is inhibited by the amount of S already present in the neighboring cells. Differentiation occurs when a cell reaches a level of S above a given threshold.

The competition CA model we propose to describe this situation is the following. Due to the analogy with the biological system, we shall consider a hexagonal lattice which is a reasonable approximation of the cell arrangement observed in the drosophila'embryo. We assume that the values of S can be 0 (inhibited) or 1 (active) in each lattice cell.

- A $S = 0$ cell will grow (i.e. turn to $S = 1$) with probability p_{grow} provided that all its neighbors are 0. Otherwise, it stays inhibited.
- A cell in state $S = 1$ will decay (i.e. turn to $S = 0$) with probability p_{decay} if it is surrounded by at least one active cell. If the active cell is isolated (all the neighbors are in state 0) it remains in state 1.

The evolution stops (stationary process) when no $S = 1$ cell feels any more inhibition from its neighbor and when all $S = 0$ cells are inhibited by their neighborhood. Then, cells with $S = 1$ are those which will differentiate.

What is the expected fraction of these $S = 1$ cells in the final configuration? Clearly, the maximum value is $1/3$ which, according to the inhibition condition we imposed, is the close-packed situation on the hexagonal lattice. On the other hand, the minimal value is $1/6$, corresponding to a situation where the lattice is partitioned in blocks with one active cell surrounded by 5 inhibited cells. In practice we do not expect any of these two limits to occur spontaneously after the automaton evolution. On the contrary, we should observe clusters of close-packed active cells surrounded by defects, i.e. regions of low density of active cells (see Fig. 4).

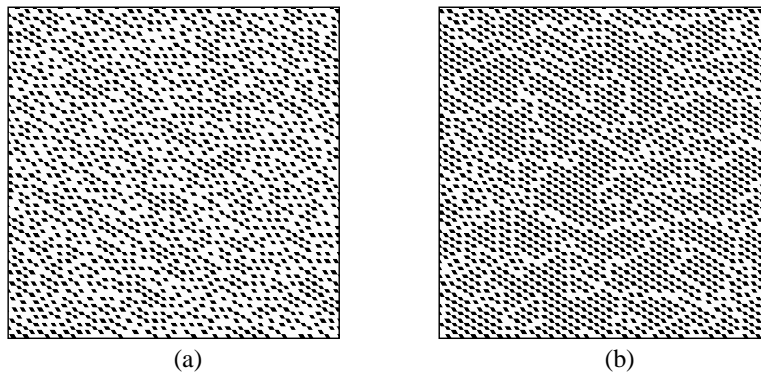


Fig. 4. Final (stationary) configuration of the competition CA model. (a) A typical situation with about 23% of active cells, obtained with almost any value of p_{anihil} and p_{growth} . (b) Configuration obtained with $p_{\text{anihil}} = 1$ and $p_{\text{growth}} = .8$ and yielding a fraction of 28% of active cells; one clearly sees the close-packed regions and the defects.

CA simulations give a very interesting result, namely that the fraction s of active cells when the stationary state is reached is

$$.23 \leq s \leq .24$$

almost irrespectively of the values chosen for p_{anihil} and p_{growth} . This is exactly what we expect from the biological observations made on the drosophila's embryo. Thus, cell differentiation can be explained by a geometrical competition without having to specify the inhibitory couplings between adjacent cell and the production rate (i.e. the values of p_{anihil} and p_{growth}): the result is quite robust against any possible choices.

In our CA model, there are, however, some pathological results when either p_{anihil} or p_{growth} equals to one. For instance for $p_{\text{anihil}} = 1$ and $p_{\text{growth}} = .8$, we obtain $s \approx .28$. This situation is illustrated in Fig. 4(b).

2.4. Traffic models

Cellular automata models for road traffic have received a great deal of interest during the past few years (see Refs. 41, 125, 126, 156, 158, 184, 185, 190 for instance).

2.4.1. One-dimensional models

One-dimensional models for single lane car motions are quite simple and elegant. The road is represented as a line of cells, each of them being occupied or not by a vehicle. All cars travel in the same direction (say to the right). Their positions are updated synchronously. During the motion, each car can be at rest or jump to the nearest neighbor site, along the direction of motion. The rule is simply that a car moves only if its destination cell is empty. This means that the drivers are short-sighted and do not know whether the car in front will move or is also stuck by another car. Therefore, the state of each cell s_i is entirely determined by the occupancy of the cell itself and its two nearest neighbors s_{i-1} and s_{i+1} . The motion rule can be summarized by the following table, where all eight possible configurations $(s_{i-1}s_i s_{i+1})_t \rightarrow (s_i)_{t+1}$ are given

$$\begin{array}{cccccccc} (111) & (110) & (101) & (100) & (011) & (010) & (001) & (000) \\ \underbrace{}_1 & \underbrace{}_0 & \underbrace{}_1 & \underbrace{}_1 & \underbrace{}_1 & \underbrace{}_0 & \underbrace{}_0 & \underbrace{}_0 \end{array} . \quad (2.5)$$

This cellular automaton rule turns out to be Wolfram's rule 184 [188, 190].

This simple dynamics captures an interesting feature of real car motion: traffic congestion. Suppose we have a low car density ρ in the system, for instance something like

$$\dots 0010000010010000010 \dots . \quad (2.6)$$

This is a *free* traffic regime in which all the cars are able to move. The average velocity $\langle v \rangle$ defined as the number of motions divided by the number of cars is then

$$\langle v_f \rangle = 1 , \quad (2.7)$$

where the subscript f indicates a free state. On the other hand, in a high density configuration such as

$$\cdots 110101110101101110 \cdots \quad (2.8)$$

only 6 cars over 12 will move and $\langle v \rangle = 1/2$. This is a partially jammed regime.

If the car positions were uncorrelated, the number of moving cars (i.e the number of particle-hole pairs) would be given by $L\rho(1-\rho)$, where L is the system size. Since the number of cars is ρL , the average velocity would be

$$\langle v_{\text{uncorrel}} \rangle = 1 - \rho. \quad (2.9)$$

However, in this model, the car occupancy of adjacent sites is highly correlated and the vehicles cannot move until a hole has appeared in front of them. The car distribution tries to self-adjust to a situation where there is one spacing between consecutive cars. For densities less than one-half, this is easily realized and the system can organize to have one car every other site.

Therefore, due to these correlations, Eq. (2.9) is wrong in the high density regime. In this case, since a car needs a hole to move to, we expect that the number of moving cars simply equals the number of empty cells [190]. Thus, the number of motions is $L(1-\rho)$ and the average velocity in the jammed phase is

$$\langle v_j \rangle = \frac{1-\rho}{\rho}. \quad (2.10)$$

A richer version of the above CA traffic model is due to Nagel and Schreckenberg [126, 184, 185]. The cars may have several possible velocities $u = 0, 1, 2, \dots, u_{\text{max}}$. Let u_i be the velocity of car i and d_i the distance, along the road, separating cars i and $i+1$. The updating rule is:

- The cars accelerate when possible: $u_i \rightarrow u'_i = u_i + 1$, if $u_i < u_{\text{max}}$.
- The cars slow down when required: $u'_i \rightarrow u''_i = d_i - 1$, if $u'_i \geq d_i$.
- The cars have a random behavior: $u''_i \rightarrow u'''_i = u''_i - 1$, with probability p_i if $u''_i > 0$.
- Finally the cars move u'''_i sites ahead.

This rule captures some important behaviors of real traffic on a highway: velocity fluctuations due to a non-deterministic behavior of the drivers, and “stop-and-go” waves observed in high density traffic regime (i.e. some cars get stopped for no specific reasons).

2.4.2. A 2D traffic model

A CA traffic model can also be defined for the situation of a street network, where several lanes may cross provided that the rule is extended to deal with cars entering the same road junction. In the case of an urban traffic, we may restrict ourselves to a one speed CA.

Our approach is to model a road intersection as a rotary. Cars in the rotary have priority over those willing to enter. It is easy to add traffic lights in such a model by blocking the entry to the rotary to a car coming from a given road. Note that road crossings may be a bottleneck limiting the traffic flow and, thus, causing congestion.

Let us consider the case of a Manhattan-like city. We assume that horizontal roads consist of two lanes, one for eastward motion and the other for westward motion. Similarly, vertical streets are composed of northbound and southbound lanes. Road junctions are formed by central points around which the traffic moves always in the same direction.

A four-corner junction is shown in Fig. 5. The four middle cells constitute the rotary. A vehicle on the rotary (like *b* or *d*) can either rotate counterclockwise or exit. A local flag t_f is used to decide the motion of a car in a rotary. If $t_f = 0$, the vehicle (like *d*) exits in the direction allowed by the color of its lane (see figure caption). If $t_f = 1$, the vehicle moves counterclockwise, like *b*. The value of the local turn flag t_f can be updated according to the modeling needs: it can be constant for some amount of time to impose a particular motion at a given junction, completely random, random with some bias to favor a direction of motion, or may change deterministically according to any user specified rule.

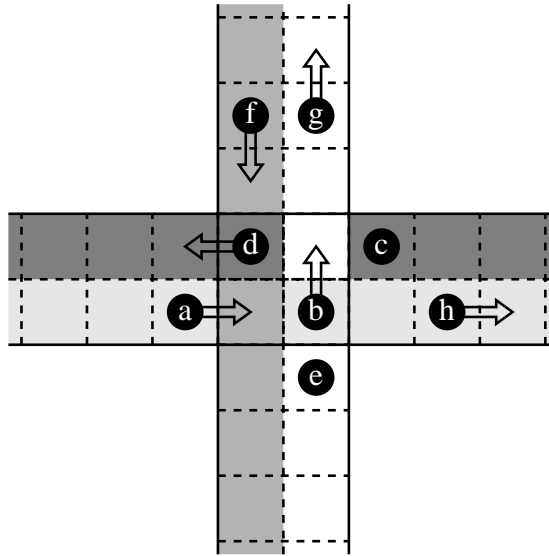


Fig. 5. Example of a traffic configuration near a junction. The four central cells represent a rotary which is traveled counterclockwise. The grey levels indicate the different traffic lanes: white is a northbound lane, light grey an eastbound lane, grey a southbound lane and, finally, dark grey is a westbound lane. The dots labeled *a*, *b*, *c*, *d*, *e*, *f*, *g* and *h* are cars which will move to the destination cell indicated by the arrows, as determined by the cell turn flag t_f . Cars without an arrow are forbidden to move.

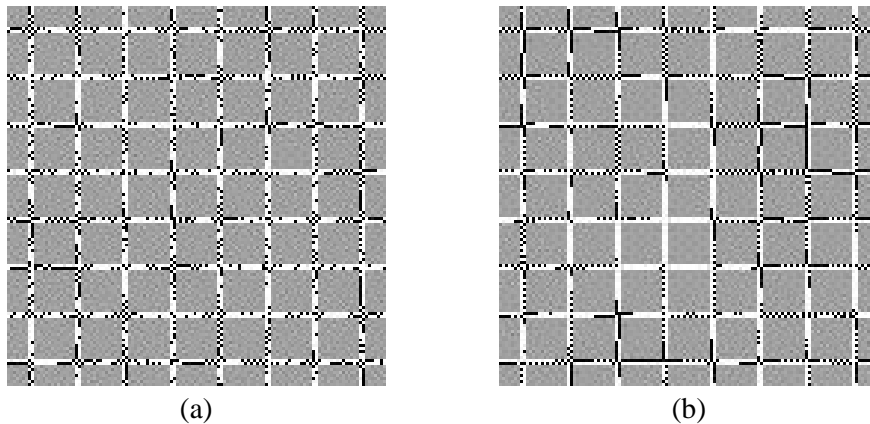


Fig. 6. Traffic configuration after 600 iterations, for a car density of 30%. Streets are white, buildings grey and the black pixels represent the cars. The Situation (a) corresponds to an equally likely behavior at each rotary junction, whereas image (b) mimics the presence of traffic lights. In the second case, queues are more likely to form and the global mobility is less than in the first case.

Figure 6 shows a typical traffic configurations. In Fig. 6(a), a vehicle has a probability $1/2$ to exit at each rotary cell. In Fig. 6(b), the turn flag t_f has an initial random distribution on the rotary. This distribution is fixed for the first 20 iterations and then flips to $t_f = 1 - t_f$ for the next 20 steps and so on. In this way, a junction acts as a kind of traffic light, which for some amount of time, allows only a given flow pattern. We observed that the global traffic pattern is different in the two cases: in case (a), the car distribution is quite homogeneous along the streets. On the other hand, in case (b), cars get queued at some junctions while some other streets remain empty.

The behavior of the above traffic model can be described analytically [41]. The first important fact is that a rotary junction has a maximum possible flow of cars. Thus, the number of vehicles able to enter a rotary per unit time cannot be larger than a given value determined by the rule of motion. Therefore, there is a critical average density ρ_1^{crit} above which the traffic is not free but constrained by this maximum rotary flow. As a result, car queues are formed at road junctions.

The second key observation is that, in the regime above ρ_1^{crit} , the system self-organizes in three different regions of fixed car densities: the queues that form before a junction, the road segments after a junction, characterized by a low traffic density and the region inside a rotary. The three densities associated to these different regions correspond to a jammed density ρ_j , a free traffic density ρ_f and a rotary density ρ_r , respectively.

As the overall car number is increased, ρ_j , ρ_f and ρ_r remains constant: the result of increasing the number of cars is to extend the length ℓ of the car queues, without changing the density in the three regions. The reason for fixed densities is that, due to the flow diagram of rule 184 [190], there are only two possible densities

18 *B. Chopard, et al.*

ρ_f and ρ_j compatible with a given traffic flow $\rho\langle v \rangle$, along a road segment. Thus, the only way to absorb an excess of cars is to increase the size of the queue.

When one keeps adding cars in the system, there is a second critical average density ρ_2^{crit} for which the length of some queues becomes larger than the distance separating two consecutive street intersections. The up-traffic rotary output gets disturbed and, from a maximum-flow traffic regime, one gets into a strongly jammed phase.

Provided that the turning decision at rotaries is random and not time correlated, one typically obtains [41]

$$\rho_f = \frac{1}{4}, \quad \rho_j = \frac{3}{4}, \quad \rho_r = \frac{1}{2}. \quad (2.11)$$

Assuming that the queue length is ℓ along all road segments and that the separation between two consecutive junctions is L (the network period), we can relate the average car density ρ to ℓ by the relation [190]

$$4(L - 2 - \ell)\rho_f + 4\ell\rho_j + 4\rho_r = 4L\rho. \quad (2.12)$$

Equation (2.12) simply reflects that the total number of cars is distributed in three regions: queues of length ℓ and density ρ_j , free traffic segments of length $L - \ell - 2$ and density ρ_f and rotaries of size four and density ρ_r .

In the case of large L , the queue length can be approximated by

$$\frac{\ell}{L} = \frac{\rho - \rho_f}{\rho_j - \rho_f}. \quad (2.13)$$

Equation (2.13) provides a way to determine the critical densities ρ_1^{crit} and ρ_2^{crit} . For $\rho < \rho_f$, ℓ is negative, which should be interpreted in the sense that no queue is formed. This is the free traffic regime. Thus, $\rho_1^{\text{crit}} = \rho_f = 1/4$ and the average velocity is $\langle v \rangle = 1$, independent of ρ .

On the other hand, for $\rho_f < \rho < \rho_j$, car queues form but their lengths are smaller than the distance between successive intersections. This is the maximum flow regime. In this case, we have $\rho\langle v \rangle = J = \text{const} = 1/4$, that is $\langle v \rangle = 1/(4\rho)$.

Finally, for $\rho > \rho_j = \rho_2^{\text{crit}}$, the queues reach their maximum length L and the rotary exits are hindered. This is the strongly jammed traffic regime. The traffic velocity is governed by the motion of holes and obeys Eq. (2.10), namely $\langle v \rangle = (1 - \rho)/\rho$. If $\langle v \rangle$ is taken as the order parameter, both of these transitions are second order.

Figure 7(a) shows the velocity-density diagram obtained from CA simulations, for the situation we just described. We have considered various road spacings for our measurements (i.e the distance L separating consecutive intersections). The larger the spacing the better the agreement with the analytical description. Note that for small L , the correlation along the lane cannot build up and $\langle v \rangle$ obeys Eq. (2.9).

In Fig. 7(b), we also show the velocity-density diagram in the case the drivers choose the rotary exit at random but stick to this decision even if the exit they have chosen is not free.

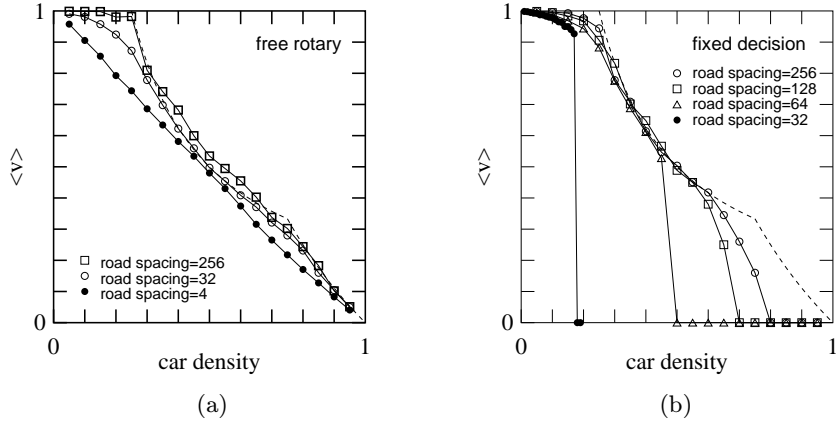


Fig. 7. Average velocity versus average density for the cellular automata street network, for (a) time-uncorrelated turning strategies and (b) a fixed driver’s decision. The different curves correspond to different distances L between successive road junctions. The dashed line is the analytical prediction. Junction deadlock is likely to occur in (b), resulting in a completely jammed state.

The present CA model can be adapted to simulate traffic in more realistic situations. We have considered the case of the city of Geneva and its suburbs [56, 35]. The simulations uses the full road network (4000 km, 3145 road segments and 1066 junctions with a number of 800765 cells) and a large set of origin and destination pairs (about 50 000) for the cars traveling during the rush hour.

The precise departure time of each vehicle is not known from observations. It is natural to assume that the distribution of these departure times is not uniform. Here we assume that this distribution has the form shown in Fig. 8 and is characterized by two parameters: (i) the duration I of the departure period and (ii) the ratio p_2/p_1 specifying the degree of non-uniformity. Empirically we choose $p_2/p_1 = 6$ and $I = 45$ minutes (so that almost all cars have arrived after 90 minutes).

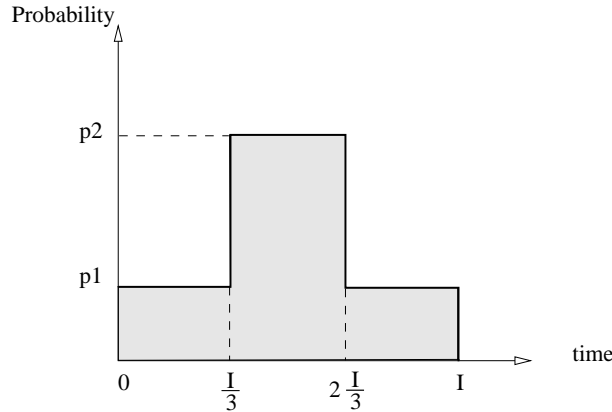


Fig. 8. Distribution of departure times used in the simulation of the city of Geneva traffic.

Due to the lack of data concerning the real evolution of the traffic state in the city of Geneva, we did not investigate systematically the effect of varying p_2/p_1 and I . Rather, we focused on the problem of measuring the time necessary for a test car to travel from a given origin A to a given destination B . This time is of direct interest to the drivers because it determines, for instance, when they must leave their house in order to be on time at their workplace. This is also a quantity which is easily compared with reality by actually driving from A to B .

The interesting fact is that the travel time is a fluctuating quantity. If one repeats the same trip under the same condition (for instance the next day, at the same time), the drive is likely to be longer or shorter. This fact is well known from everyday experience and is also well reproduced in the CA model because the probability distribution of the departure times gives the necessary randomness to produce fluctuations when the simulation is repeated.

Our main result is that the amplitude of the variations of the travel times depends very much on the departure time of the test car and on its trip. In the simulations, we studied the four trips shown in Fig. 9.

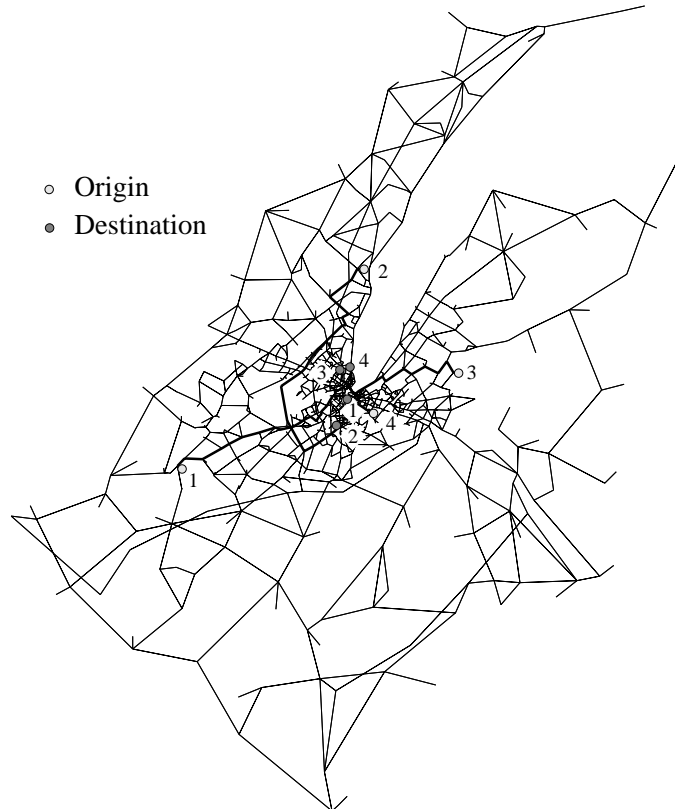


Fig. 9. The road network of Geneva used in our simulation and the four selected trips considered to measure the travel time of a test car.

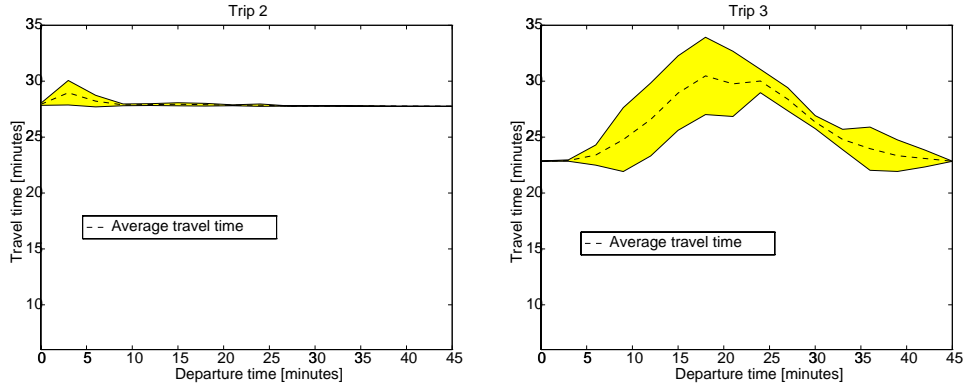


Fig. 10. Expectation time and “risk” of trips 2 and 3 of Fig. 9. The horizontal axis corresponds to the departure time of a test vehicle within interval I . The dashed line shows the average driving time and the shaded region indicates the amplitude of the variation of this time (computed as the standard deviation). Note that the times shown here are pretty realistic, thus giving an indirect validation of our simulations for the case of Geneva.

The measured times obtained from the simulation for trips 2 and 3 are shown in Fig. 10. The results for trip 1 and 4 are similar.

For trip 3, the average time needed to reach the desired destination is not constant: it is maximal if the driver leaves 15 to 20 minutes after the start of the rush hour. It is minimal if the driver leaves at the very beginning or the very end of interval I . On the other hand, the average time for trip 2 is quite stable. These two situations differ by the fact that trip 3 uses heavily loaded sections with many crossings while trip 2 uses higher capacity sections.

We also observe that, for trip 3, it is impossible to make accurate predictions on the time needed to reach the destination point. Variations of up to 30% show up. We call this variation the *risk*^c associated to the trip (for a given departure time) to describe the fact that an expected outcome is likely not to occur. In practice, for trip 3, in which the variation is high, there is a large risk to arrive late at the destination, or to be too early, which may not be acceptable either. This also means that it is not possible to establish an accurate schedule for taxis or public transportation, unless dedicated lanes are available.

Finally, Fig. 11 shows the dependence of $\langle v \rangle$, the average car velocity in the network, as a function of the average car density ρ . Since the traffic load is not stationary but concentrated within about one and a half hour, the steady-state density-velocity diagram (as shown for instance in Fig. 7) is no longer valid and must be replaced by a “dynamic” diagram which shows a significant hysteresis.

^cIn finance, the term risk is also used to describe the standard deviation of a random quantity.

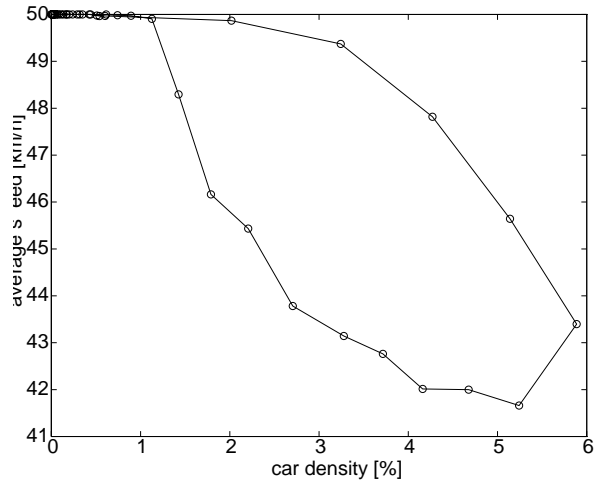


Fig. 11. Dynamical flow diagram for $p_2/p_1 = 6$. As time goes on ($t \in [0, I]$), the car density first increases and the upper branch of the diagram is formed; then, when the density decreases, the lower branch is measured.

2.5. A simple gas: the HPP model

The HPP rule is a simple example of an important class of cellular automata models: lattice gas automata (LGA). The basic ingredient of such models are point particles that move on a lattice, according to appropriate rules so as to mimic a fully discrete “molecular dynamics.”

The HPP lattice gas automata is traditionally defined on a two-dimensional square lattice. Particles can move along the main directions of the lattice, as shown in Fig. 12. The model limits to 1 the number of particles entering a given site

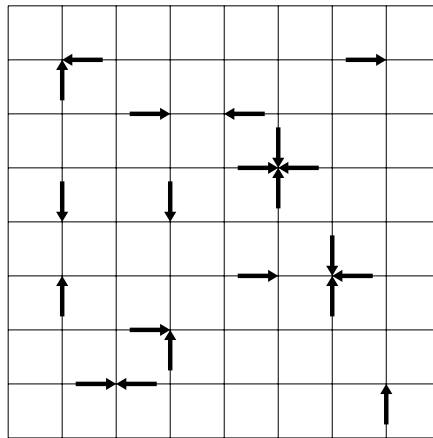


Fig. 12. Example of a configuration of HPP particles.

with a given direction of motion. This is the exclusion principle which is common in most LGA. Consequently, four bits of information in each site are enough to describe the system during its evolution. For instance, if at iteration t site \vec{r} has the following state $s(\vec{r}, t) = (1011)$, it means that three particles are entering the site along direction 1, 3 and 4, respectively.

The cellular automata rule describing the evolution of $s(\vec{r}, t)$ is often split into two steps: collision and motion (or propagation). The collision phase specifies how the particles entering the same site will interact and change their trajectories. The purpose of the HPP rule is to model a gas of colliding particles and, thus, essential features of this step are borrowed from real microscopic interactions, namely local conservation of momentum and particle number. Since the collision phase amounts to rearranging the particles in different direction, it ensures that the exclusion principle will be satisfied, provided that it was at time $t = 0$.

During the propagation phase, the particles actually move to the nearest neighbor site they are traveling to. Figure 13 illustrates the HPP rules. This decomposition into two phases is a quite a convenient way to partition the space so that the collision rule is purely local.

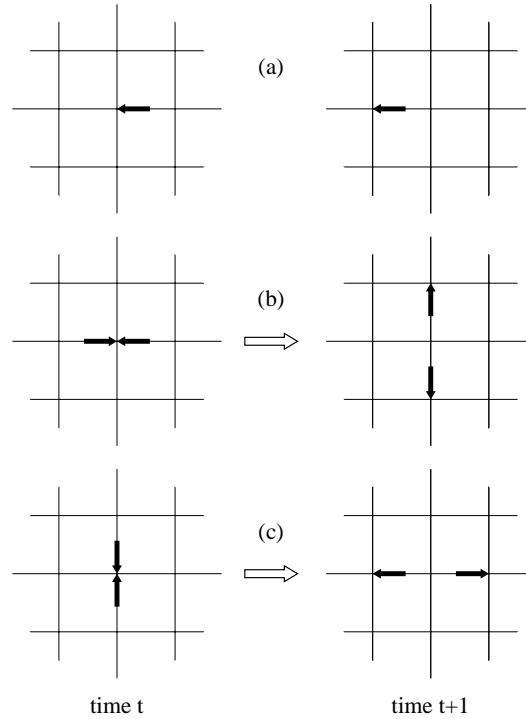


Fig. 13. The HPP rule: (a) a single particle has a ballistic motion until it experiences a collision; (b) and (c) the two non-trivial collisions of the HPP model: two particles experiencing a head on collision are deflected in the perpendicular direction. In the other situations, the motion is ballistic, that is the particles are transparent to each other when they cross the same site.

According to our Boolean representation of the particles at each site, the collision part for the two head on collisions are expressed as

$$(1010) \rightarrow (0101), \quad (0101) \rightarrow (1010) \quad (2.14)$$

all the other configurations being unchanged. During the propagation phase, the first bit of the state variable is shifted to the east neighbor cell, the second bit to the north and so on.

The aim of this rule is to reproduce some aspect of the real interactions between particles, namely that momentum and particle number are conserved during a collision. From Fig. 13, it is easily checked that these properties are obeyed: a pair of zero momentum particles along a given direction is transformed into another pair of zero momentum along the perpendicular axis.

The HPP rule captures another important ingredient of the microscopic nature of a real interaction: invariance under time reversal. Figures 13(b) and 13(c) show that, if at some given time, the directions of motion of all particles are reversed, the system will just trace back its own history. Since the dynamics of a deterministic cellular automaton is exact, this fact allows us to demonstrate the properties of physical systems to return to their original situation when all the particles reverse their velocity.

Figure 14 illustrates the time evolution of a HPP gas initially confined in the left compartment of a container. There is an aperture on the wall of the compartment and the gas particles will flow so as to fill the entire space available to them. In order to include a solid boundary in the system, the HPP rule is modified as follows: when

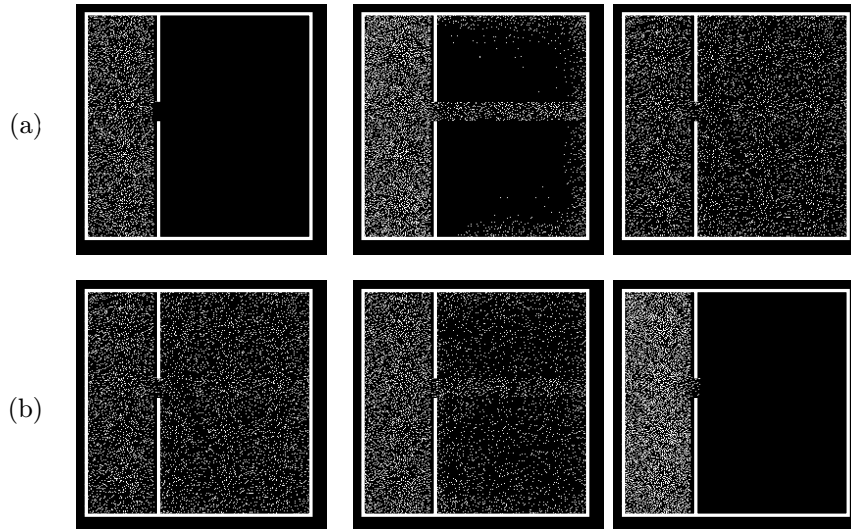


Fig. 14. Time evolution of a HPP gas. (a) From the initial state to equilibrium. (b) Illustration of time reversal invariance: in the rightmost image of (a), the velocity of each particle is reversed and the particles naturally return to their initial position.

a site is a wall (indicated by an extra bit), the particles no longer experience the HPP collision but bounce back from where they came. Therefore, particles cannot escape a region delimited by such a reflecting boundary.

If the system of Fig. 14 is evolved, it reaches an equilibrium after a long enough time and no macroscopic trace of its initial state is any longer visible. However, no information has been lost during the process (no numerical dissipation) and the system has the memory of where it comes from. Reversing all the velocities and iterating the HPP rule makes all particles go back to the compartment in which they were initially located.

This behavior is only possible because the dynamics is perfectly exact and that no numerical errors are present in the numerical scheme. If one introduces externally some errors (for instance, one can add an extra particle in the system) before the direction of motion of each particle is reversed, then reversibility is lost.

The HPP rule is important because it contains the basic ingredients of many models we are going to discuss below. However, the capability of this rule to model a real gas of particles is poor, due to a lack of isotropy and spurious invariants. We shall see in Sec. 3 that a remedy to this problem is to use a different lattice.

2.6. *Random walk*

The HPP rule we discussed in the previous section can be easily modified to produce many synchronous random walks. Instead of experiencing a mass and momentum conserving collision, each particle now selects, at random, a new direction of motion among the possible values permitted by the lattice. Since several particles may enter the same site (up to four, on a two-dimensional square lattice), the random change of directions should be such that there are never two or more particles exiting a site in the same direction. This would otherwise violate again the exclusion principle.

The solution is to shuffle the directions of motion or, more precisely, to perform a random permutation of the velocity vectors, independently at each lattice site and at each time step. Figure 15 illustrates this probabilistic evolution rule. Note that at a macroscopic level of description, the random walk rule corresponds to a diffusion process (see Sec. 6.3.1).

As an example of the use of the present random walk cellular automata rule, we discuss an application to growth processes. In many cases, growth is governed by a spatial quantity such as an electric field, a local temperature, or a particle density field [177]. Aggregation constitutes an important mechanism: like particles stick to each other as they meet and, as a result, form a complicated pattern with a branching structure.

A prototype model of aggregation is the so-called DLA model (diffusion-limited aggregation), introduced by Witten and Sander [183] in the early 1980s. Since its introduction, the DLA model has been investigated in great detail. However, diffusion-limited aggregation is a far from equilibrium process which is not described theoretically by first principles only. Spatial fluctuations that are typical of the DLA

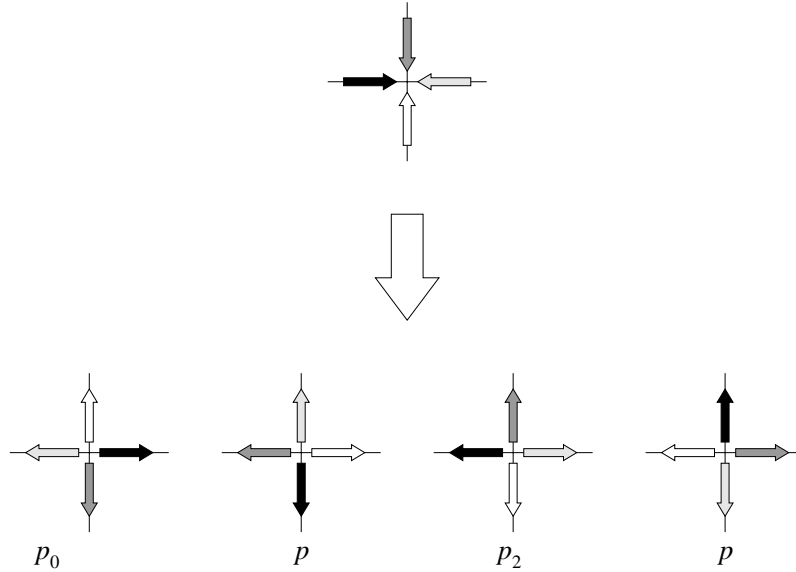


Fig. 15. How the entering particles are deflected at a typical site, as a result of the diffusion rule. The four possible outcomes occur with respective probabilities p_0 , p_1 , p_2 and p_3 . The figure shows four particles, but the mechanism is data-blind and any one of the arrows can be removed when fewer entering particles are present.

growth are difficult to take into account and a numerical approach is necessary to complete the analysis.

DLA-like processes can be readily modeled by our diffusion cellular automata, provided that an appropriate rule is added to take into account the particle-particle aggregation. The first step is to introduce rest particles to represent the particles of the aggregate. Therefore, in a two-dimensional system, a lattice site can be occupied by up to four diffusing particles, or by one “solid” particle. Our approach has some differences compared with the original Witten and Sanders model. All particles reside on a lattice and move simultaneously. They can stick to different part of the cluster and we do not launch them, one after the other, from a region far away from the cluster. For this reason, we may expect some quantitative variation from the original DLA properties.

Figure 16 shows a two-dimensional DLA-like cluster grown by the cellular automata dynamics. At the beginning of the simulation, one or more rest particles are introduced in the system to act as aggregation seeds. The rest of the system is filled with particles with average concentration ρ . When a diffusing particle becomes a nearest neighbor to a rest particle, it stops and sticks to it by transforming into a rest particle. Since several particles can enter the same site, we may choose to aggregate all of them at once (i.e. a rest particle is actually composed of several moving particles), or to accept the aggregation only when a single particle is present.

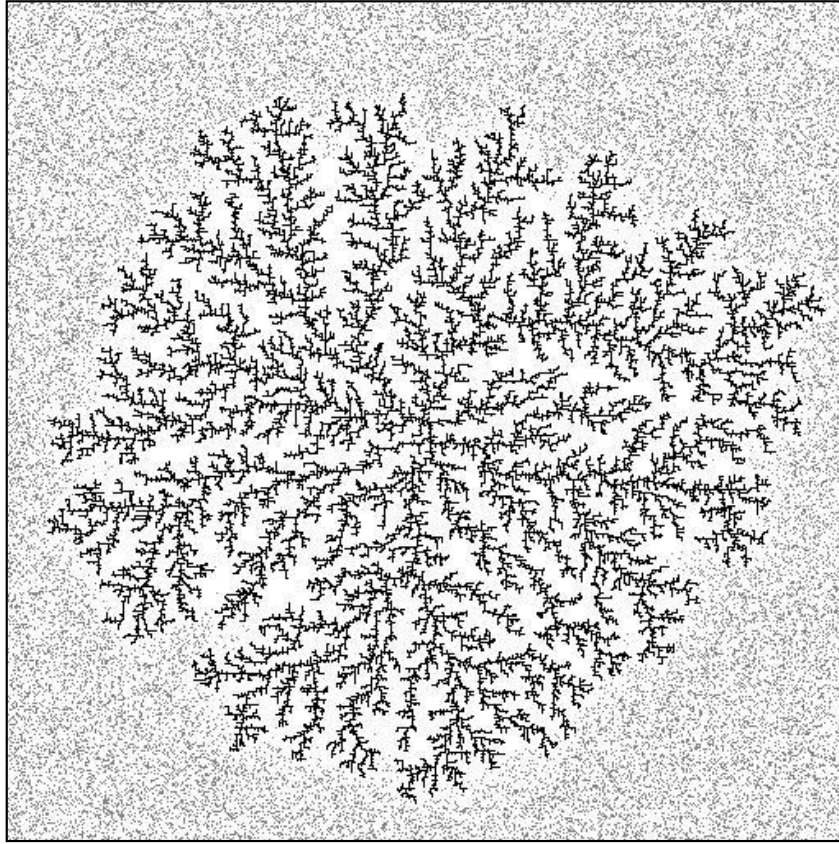


Fig. 16. Two-dimensional cellular automata DLA-like cluster (black), obtained with $p_s = 1$, an aggregation threshold of 1 particle and a density of diffusing particles of 0.06 per lattice direction. The gray dots represent the diffusing particles not yet aggregated.

In addition to this question, the sticking condition is important. If any diffusing particle always sticks to the DLA cluster, the growth is very fast and can be influenced by the underlying lattice anisotropy. It is therefore more appropriate to stick with some probability p_s . Since up to four particles may be simultaneously candidates for the aggregation, we can also use this fact to modify the sticking condition. A simple way is to require that the local density of particles be larger than some threshold (say 3 particles) to yield aggregation. The cluster shown in Fig. 16 has fractal dimension $d_f = 1.78$ which is not very different from the genuine, off-lattice DLA fractal dimension [170, 177] $d_f = 1.70$.

The cellular automata approach is also well suited to study dynamical properties such as the DLA growth rate. The standard numerical experiment is to distribute uniformly the initial diffusing particles on the lattice with a single aggregation seed in the middle. As time t goes on, more and more particles get solidified and the

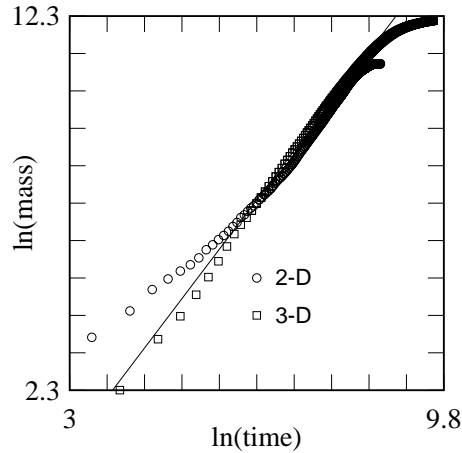


Fig. 17. Formation rate of cellular automata DLA clusters in two- and three-dimensions. The lattice has periodic boundary conditions.

cluster mass $M(t)$ increases. Our simulations indicate (see Fig. 17) that this process has an intermediate regime governed by a power law

$$M(t) \approx t^\alpha,$$

where

$$\alpha \approx 2$$

in both two and three dimensions. Although these results are not sufficient to conclude definitely that the 2-D and 3-D exponents are the same, an explanation would be that in 3-D there is more surface to stick to than in 2-D, but also more space to explore before diffusing particles can aggregate. These two effects may just compensate.

2.7. *The traveling ant*

The ant rule is a cellular automata invented by Chris Langton [164] and Greg Turk which models the behavior of a hypothetical animal (ant) having a very simple algorithm of motion. The ant moves on a square lattice whose sites are either white or grey. When the ant enters a white cell, it turns 90 degrees to the left and paints the cell in grey. Similarly, if it enters a grey cell, it paints it in white and turn 90 degree to the right.

It turns out that the motion of this ant exhibits a very complex behavior. Suppose the ant starts in a completely white space. After a series of about 500 steps where it essentially keeps returning to its initial position, it enters a chaotic phase during which its motion is unpredictable. Then, after about 10000 steps of this very irregular motion, the ant suddenly performs a very regular motion which brings it far away from where it started.

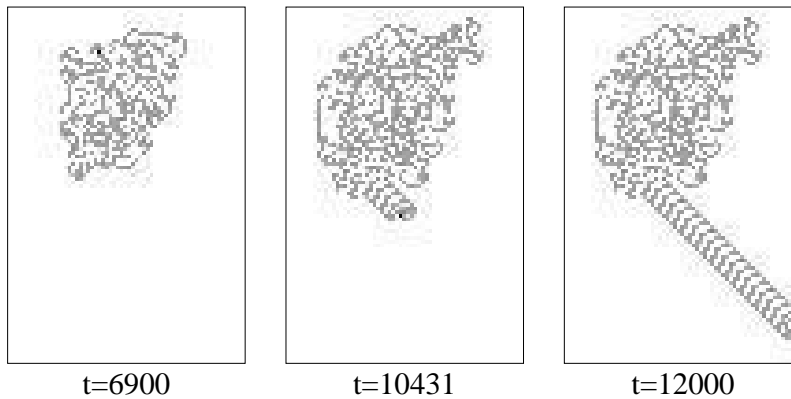


Fig. 18. The Langton's ant rule. The motion of a single ant starts with a chaotic phase of about 10000 time steps, followed by the formation of a highway. The figure shows the state of each lattice cell (gray or white) and the ant position (marked by the black dot). In the initial condition all cells are white and the ant is located in the middle of the image.

Figure 18 illustrates the ant motion. The path the ant creates to escape the chaotic initial region has been called a highway [142]. Although this highway is oriented at 45 degrees with respect to the lattice direction, it is traveled by the ant in a way which makes one very much think of a sewing machine: the pattern is a sequence of 104 steps which is repeated indefinitely.

The Langton ant is a good example of a cellular automata whose rule is very simple and yet generates a complex behavior which seems beyond our understanding. Somehow, this fact is typical of the cellular automata approach: although we do know everything about the fundamental laws governing a system (because we set up the rules ourselves!), we are often unable to explain its macroscopic behavior.

There is anyway a global property of the ant motion: the ant visits an unbounded region of space, *whatever* the initial space texture is (configuration of gray and white cells).

The proof (due to Bunimovitch and Troubetzkoy) goes as follows: supposed the region the ant visits is bounded. Then, it contains a finite number of cells. Since the number of iterations is infinite, there is a domain of cells that are visited infinitely often. Moreover, due to the rule of motion, a cell is either entered horizontally (we call it a H cell) or vertically (we call it a V cell). Since the ant turns by 90 degrees after each step, a H cell is surrounded by four V cells and conversely. As a consequence, the H and V cells tile the lattice in a fixed checkerboard pattern. Now, we consider the upper rightmost cell of the domain, that is a cell whose right and upper neighbor is not visited. This cell exists if the trajectory is bounded. If this cell is a H cell (and it is so for ever), it has to be entered horizontally from the left and exited vertically downward and, consequently becomes gray. However, after the ant has left, the cell is white and there is a contradiction. The same contradiction appears if the cell is a V cell. Therefore, the ant trajectory is not bounded.

As it has been described, the above rule is defined only when a single ant moves on the lattice. We can easily generalize it when many ants are simultaneously present so that up to four of them may enter the same site at the same time, from different sides

Following the same idea as in the HPP rule, we will introduce $n_i(\vec{r}, t)$ as a Boolean variable representing the presence ($n_i = 1$) or the absence ($n_i = 0$) of an ant entering site \vec{r} at time t along lattice direction \vec{c}_i , where $\vec{c}_1, \vec{c}_2, \vec{c}_3$ and \vec{c}_4 stand for direction right, up, left and down, respectively. If the color $\mu(\vec{r}, t)$ of the site is gray ($\mu = 0$), *all* entering ants turn 90 degrees to the right. On the other hand, if the site is white ($\mu = 1$), they all turn 90 degrees to the left. The color of each cell is modified after one or more ants have gone through. Here, we chose to switch $\mu \rightarrow 1 - \mu$ only when an odd number of ant are present.

When several ant travel simultaneously on the lattice, cooperative and destructive behaviors are observed. First, the erratic motion of several ants favors the formation of a local arrangement of colors allowing the creation of a highway. One has to wait much less time before the first highway appears. Second, once a highway is being created, other ants may use it to travel very fast (they do not have to follow the complicated pattern of the highway builder. In this way, the term “highway” is very appropriate. Third, a destructive effect occurs as the second ant gets to the highway builder. It breaks the pattern and several situations may be observed. For instance, both ants may enter a new chaotic motion; or the highway is traveled in the other direction (note that the rule is time reversal invariant) and destroyed. Figure 19 illustrates the multi-ant behavior.

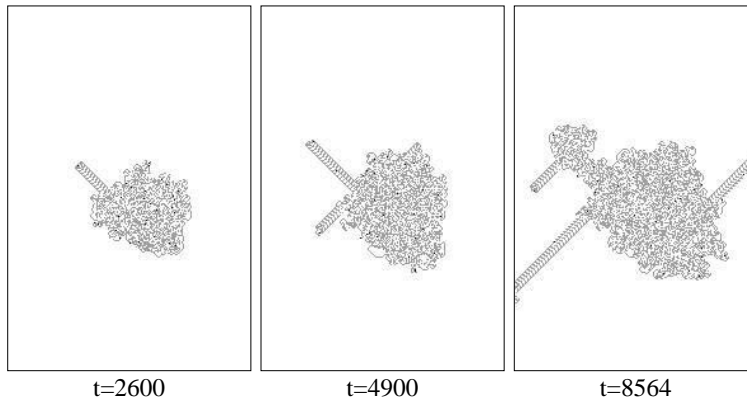


Fig. 19. Motion of several Langton’s ants. Gray and white indicate the colors of the cells at the current time. Ant locations are marked by the black dots. At the initial time, all cells are white and a few ants are randomly distributed in the central region, with random directions of motion. The first highway appears much earlier than when the ant is alone. In addition the highway can be used by other ants to travel much faster. However, the “highway builder” is usually prevented from continuing its construction as soon as it is reached by the following ants. For instance, the highway heading north-west after 4900 steps get destroyed. A new highway emerges later on from the rest, as we see from the snapshot at time $t = 8564$.

The problem of an unbounded trajectory pauses again with this generalized motion. The assumption of Bunimovitch–Troubetzkoy’s proof no longer holds in this case because a cell may be both a H or a V cell. Indeed, two different ants may enter the same cell one vertically and the other horizontally. Actually, the theorem of an unbounded motion is wrong in several cases where two ants are present. Periodic motions may occur when the initial positions are well chosen.

For instance, when the relative location of the second ant with respect to the first one is $(\Delta x, \Delta y) = (2, 3)$, the two ants returns to their initial position after 478 iterations of the rule (provided they started in an uniformly white substrate, with the same direction of motion). A very complicated periodic behavior is observed when $(\Delta x, \Delta y) = (1, 24)$: the two ant start a chaotic-like motion for several thousands of steps. Then, one ant builds a highway and escape from the central region. After a while, the second ant finds the entrance of the highway and rapidly catches the first one. After the two ants meet, they start undoing their previous paths and return to their original position. This complete cycle takes about 30000 iterations.

More generally, it is found empirically that, when $\Delta x + \Delta y$ is odd and the ants enter their site with the same initial direction, the two-ant motion is likely to be periodic. However, this is not a rule and the configuration $(\Delta x, \Delta y) = (1, 0)$ yields an unbounded motion, a diamond pattern of increasing diameter which is traveled in the same direction by the two ants.

It turns out that the periodic behavior of a two-ant configuration is not so surprising. The rule we defined is reversible in time, provided that there is never more than one ant at the same site. Time reversal symmetry means that if the direction of motion of all ants are reversed, they will move backward through their own sequence of steps, with an opposite direction of motion. Therefore, if at some point of their motion the two ants cross each other (on a lattice link, not on a site), the first ant will go through the past of the second one, and vice versa. They will return to the initial situation (the two ants being exchanged) and build a new pattern, symmetrical to the first one, due to the inversion of the directions of motion. The whole process then cycles for ever. Periodic trajectories are therefore related to the probability that the two ants will, at a some time, cross each other in a suitable way. The conditions for this to happen are fulfilled when the ants sit on a different sublattice (black or white sites on the checkerboard) and exits two adjacent sites against each other. This explain why a periodic motion is likely to occur when $\Delta x + \Delta y$ is odd.

2.8. Population dynamics

In addition to physical, chemical or biological systems, the CA approach is interesting for the study of simple population models. Several different problems can be envisaged, such as the simulation of ecosystems or the social behavior in a population of interacting individuals. Here we consider an example of the latter situation.

The social behavior of the group of persons is certainly related to the fact that each individual has its own autonomy and perception of the environment. On the

other hand, the behavior of a whole population may also reflect some “mechanical” or spontaneous response of an individual to the situation it is confronted with. We may hope that the collective behavior that may emerge from such a process could be captured by some CA model, provided that one is able to find the rule to which each individual obeys. At least it is worthwhile to check whether a given social behavior can be explained with such mechanisms before incriminating the fact that each individual is free to think and act in its own way.

Here we address the generic problem of the competing fight between two different groups over a fixed area. We present a “voter model” which describes the dynamical behavior of a population with bimodal conflicting interests and study the conditions of extinction of one of the initial groups [69].

This model can be thought of as describing the smoker–non-smoker fight: in a small group of persons, a majority of smokers will usually convince the few others to smoke and vice versa. The point is really when an equal number of smokers and non-smokers meet. In that case, it may be assumed that a social trend will decide between the two attitudes. In the US, smoking is viewed as a disadvantage whereas, in France, it is rather well accepted. In other words, there is a bias that will select the winning party in an even situation. In our example, whether one studies the French or US case, the bias will be in favor of the smokers or the non-smokers, respectively.

The same mechanism can be associated with the problem of competing standards. The choice of one or the other standard is often driven by the opinion of the majority of people one meets. But, when the two competing systems are equally represented, the intrinsic quality of the product will be decisive. Price and technological advance then play the role of a bias.

Here we consider the case of four-person confrontations in a spatially extended system in which the actors (species A or B) move randomly. Initially, the B species is present with density b_0 and the A species with density $1 - b_0$. The B individuals are supposed to have a qualitative advantage over the A s but are less numerous. The question we want to address is what is the minimal density b_0 which make the B s win over the A s (i.e. invade the entire system at the expense of the A individuals). The process of spatial contamination of opinion plays a crucial role in this dynamics.

The CA rule we propose here [69] to describe this process is derived from a model by Galam [68], in which the four individuals involved in a tournament are randomly chosen among the current population, whose composition in A or B type of persons evolves after each confrontation. The density threshold for an invading emergence of B is $b_c = 0.23$ if the B group has a qualitative bias over A . With a spatial distribution of the species, even if $b_0 < b_c$, B can still win over A provided that it strives for confrontation. Therefore a qualitative advantage is found not to be enough to win. A geographic as well a definite degree of aggressiveness are instrumental to overcome the less fitted majority.

The model we use to describe the two populations A and B influencing each other or competing for some unique resources, is based on the diffusion automaton proposed in Sec. 2.6. The particles have two possible internal states (± 1), coding for the A or B species, respectively.

The individuals move on a two-dimensional square lattice. At each site, there are always four individuals (any combination of A 's and B 's is possible). These four individuals all travel in a different lattice direction (north, east, south and west).

The interaction takes place in the form of “fights” between the four individuals meeting on the same site. At each fight, the group nature (A or B) is updated according to the majority rule, when possible, otherwise with a bias in favor of the best fitted group:

- The local majority species (if any) wins:

$$nA + mB \rightarrow \begin{cases} (n+m)A & \text{if } n > m \\ (n+m)B & \text{if } n < m \end{cases},$$

where $n + m = 4$.

- When there is an equal number of A and B on a site, B wins the confrontation with probability $1/2 + \beta/2$. The quantity $\beta \in [0, 1]$ is the bias accounting for some advantage (or extra fitness) of species B .

The above rule is applied with probability k . Thus, with probability $1 - k$ the group composition does not change because no fight occurs. Between fights both population agents perform a random walk on the lattice.

The behavior of this model is illustrated in Fig. 20. The current configuration is shown at three different time steps. We can observe the growth of dense clusters of B invading the system.

It is clear that the model richness comes from the even confrontations. If only odd fights would happen, the initial majority population would always win after some short time. The key parameters of this model are (i) k , the aggressiveness (probability of confrontation), (ii) β , the B 's bias of winning a tie and (iii) b_0 , the initial density of B .

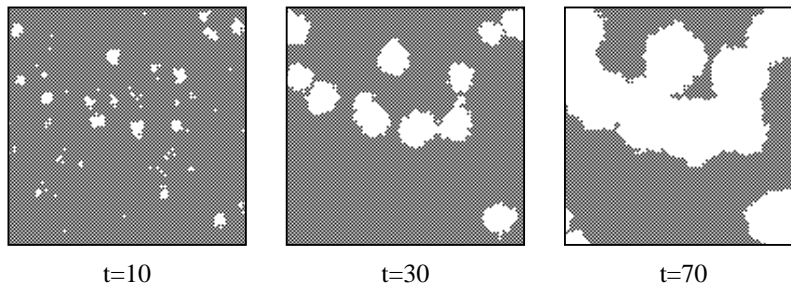


Fig. 20. Configurations of the voter CA model, at three different times. The A and B species are represented by the gray and white regions, respectively. The parameters of the simulation are $b_0 = 0.1$, $k = 0.5$ and $\beta = 1$.

The strategy according to which a minority of B 's (with yet a technical, genetic, persuasive advantage) can win against a large population of A 's is not obvious. Should they fight very often, try to spread or accept a peace agreement? We study the parameter space by running the cellular automaton.

In the limit of low aggressiveness ($k \rightarrow 0$), the particles move a long time before fighting. Due to the diffusive motion, correlation between successive fights are destroyed and B wins provided that $b_0 > 0.23$ and $\beta = 1$. This is the mean-field level of our dynamical model which corresponds to the theoretical calculations made in Ref. 68.

More generally, we observe that B can win even when $b_0 < 0.23$, provided it acts aggressively, i.e. by having a large enough k . Thus, there is a critical density $b_{\text{death}}(k) < 0.23$ such that, when $b_0 > b_{\text{death}}(k)$, all A are eliminated in the final outcome. Below b_{death} , B loses unless some specific spatial configurations of B 's are present.

Therefore the growth of species B at the expense of A is obtained by a spatial organization. Small clusters that may accidentally form act as nucleus from which the B 's can develop. In other words, above the mean-field threshold $b_c = 0.23$ there is no need to organize in order to win but, below this value only condensed regions will be able to grow. When k is too small, such an organization is not possible (it is destroyed by diffusion) and the strength advantage of B does not lead to success.

Figure 21 summarizes, as a function of b_0 and k , the regions where either A or B succeeds. It is found that the separation curve satisfies the equation $(k + 1)^7(b_0 - 0.077) = 0.153$.

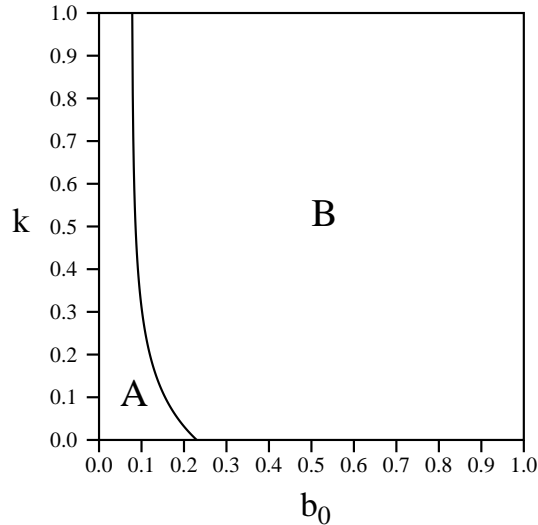


Fig. 21. Phase diagram for our socio-physical model with $\beta = 1$. The curve delineates the regions where, on the left, A wins with high probability and, on the right, B wins with probability one. The outcome depends on b_0 , the initial density of B and k , the probability of a confrontation.

It is also interesting to study the time needed to annihilate completely the loser. Here, time is measured as the number of fights per site (i.e. kt where t is the iteration time of the automaton). We observe that the dynamics is quite fast and a few units of time are sufficient to yield a collective change of opinion.

Following the same methodology, more complicated interactions between individuals can be investigated. The case of a non-constant bias is quite interesting and is described in Ref. 69. In conclusion, although this model is very simple, it abstracts the complicated behavior of real life agents by capturing some essential ingredients. For this reason, the results we have presented may shed light on the generic mechanisms observed in a social system of opinion making.

In particular we see that the correlations existing between successive fights may strongly affect the global behavior of the system and that an organization is the key feature to obtain a definite advantage over the other population. This observation is important. For instance, during a campaign against smoking or an attempt to impose a new system, it is much more efficient (and cheaper) to target the effort on small nuclei of persons rather than sending the information in an uncorrelated manner.

3. From Micro-Physics to Macro-Physics

In the previous section, we have discussed several cellular automata rules which are relevant to the description of physical processes. The question is of course how close these models are to the reality they are supposed to simulate.

In general, space and time are not discrete and, in classical physics, the state variables are continuous. Thus, it is crucial to show how a cellular automata rule is connected to the laws of physics or to the usual quantities describing the phenomena which are modeled. This is particularly important if the cellular automata is intended to be used as a numerical scheme to solve practical problems.

Lattice gas automata have a large potential of applications in hydrodynamics and reaction-diffusion processes. The purpose of this section is to present the techniques that are used to establish the connection between the macroscopic physics and the microscopic discrete dynamics of the automaton. The problem one has to address is the statistical description of a system of many interacting particles. The methods we shall discuss here are very close, in spirit, to those applied in kinetic theory: the N-body dynamics is described in terms of macroscopic quantities like the particle density or the velocity field. The derivation of a Boltzmann equation is a main step in this process.

To illustrate the method we first present the so-called FHP CA fluid model because this system features all the relevant steps of the derivation.

3.1. The FHP model

The FHP rule is a model of a two-dimensional fluid which has been introduced by Frisch, Hasslacher and Pomeau [67], in 1986. We will show here how the

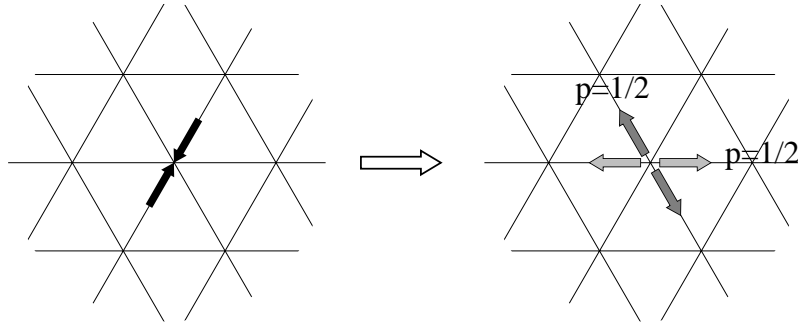


Fig. 22. The two-body collision in the FHP model. In the right part of the figure, the two possible outcomes of the collision are shown in dark and light gray, respectively. They both occur with probability one-half.

fully discrete microscopic dynamics maps onto the macroscopic behavior of hydrodynamics.

The model describes the motion of particles traveling in a discrete space and colliding with each other, very much in the same spirit as the HPP lattice gas discussed in Sec. 2.5. The main difference is that, for isotropy reasons that will become clear below, the lattice is hexagonal (i.e. each site has six neighbors, as shown in Fig. 22).

The FHP model is an abstraction, at a microscopic scale, of a fluid. It is expected to contain all the salient features of real fluid. It is well known that the continuity and Navier–Stoke equations of hydrodynamics express the local conservation of mass and momentum in a fluid. The detailed nature of the microscopic interactions does not affect the form of these equations but only the values of the coefficients (such as the viscosity) appearing in them. Therefore, the basic ingredients one has to include in the microdynamics of the FHP model is the conservation of particles and momentum after each updating step. In addition, some symmetries are required so that, in the macroscopic limit, where time and space can be considered as continuous variables, the system is isotropic.

As in the case of the HPP model, the microdynamics of FHP is given in terms of Boolean variables describing the occupation numbers at each site of the lattice and at each time step (i.e. the presence or the absence of a fluid particle). The FHP particles move in discrete time steps, with a velocity of constant modulus, pointing along one of the six directions of the lattice. The dynamics is such that no more than one particle enters the same site at the same time with the same velocity. This restriction (the exclusion principle) ensures that six Boolean variables at each lattice site are always enough to represent the microdynamics.

Interactions take place among particles entering the same site at the same time and result in a new local distribution of particle velocities. In order to conserve the number of particle and the momentum during each interaction, only a few configurations lead to a non-trivial collision (i.e a collision in which the directions of

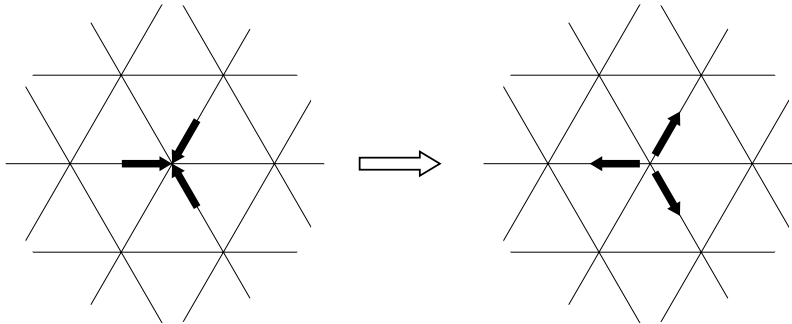


Fig. 23. The three-body collision in the FHP model.

motion have changed). For instance, when exactly two particles enter the same site with opposite velocities, both of them are deflected by 60 degrees so that the output of the collision is still a zero momentum configuration with two particles. As shown in Fig. 22, the deflection can occur to the right or to the left, indifferently. For symmetry reasons, the two possibilities are chosen randomly, with equal probability.

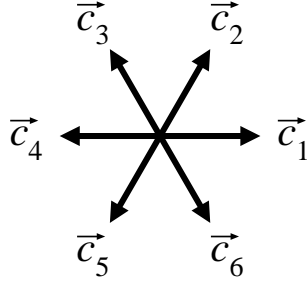
Another type of collision is considered: when exactly three particles collide with an angle of 120 degrees between each other, they bounce back (so that the momentum after collision is zero, as it was before collision). Figure 23 illustrates this rule. Several variants of the FHP model exist in the literature [50], including some with rest particles, like the FHP-II and FHP-III models.

For the simplest case we are considering here, all interactions come from the two collision processes described above. For all other configurations (i.e those which are not obtained by rotations of the situations given in Figs. 22 and 23) no collision occurs and the particles go through as they were transparent to each other.

Both two- and three-body collisions are necessary to avoid extra conservation laws. The two-particle collision removes a pair of particles with a zero total momentum and moves it to another lattice direction. Therefore, it conserves momentum along each line of the lattice. On the other hand, three-body interactions deflect particles by 180 degrees and cause the net momentum of each lattice line to change. However, three-body collisions conserve the number of particles within each lattice line.

3.2. Microdynamics

The full microdynamics of the FHP model can be expressed by evolution equations for the occupation numbers: we introduce $n_i(\vec{r}, t)$ as the number of particles (which can be either 0 or 1) entering site \vec{r} at time t with a velocity pointing along direction \vec{c}_i , where $i = 1, 2, \dots, 6$ labels the six lattice directions. The unit vectors \vec{c}_i are shown in Fig. 24.


 Fig. 24. The direction of motion \vec{c}_i .

We also define the time step as Δ_t and the lattice spacing as Δ_r . Thus, the six possible velocities \vec{v}_i of the particles are related to their directions of motion by

$$\vec{v}_i = \frac{\Delta_r}{\Delta_t} \vec{c}_i.$$

Without interactions between particles, the evolution equations for the n_i would be given by

$$n_i(\vec{r} + \Delta_r \vec{c}_i, t + \Delta_t) = n_i(\vec{r}, t), \quad (3.1)$$

which expresses that a particle entering site \vec{r} with velocity along \vec{c}_i will continue in straight line so that, at the next time step, it will enter site $\vec{r} + \Delta_r \vec{c}_i$ with still the same direction of motion. However, due to collisions, a particle can be removed from its original direction or another one can be deflected into direction \vec{c}_i .

For instance, if only n_i and n_{i+3} are 1 at site \vec{r} , a collision occurs and the particle traveling with velocity \vec{v}_i will then move with either velocity \vec{v}_{i-1} or \vec{v}_{i+1} (note that the operations on index i are wrapped onto the value $1, 2, \dots, 6$). The quantity

$$D_i = n_i n_{i+3} (1 - n_{i+1}) (1 - n_{i+2}) (1 - n_{i+4}) (1 - n_{i+5}) \quad (3.2)$$

indicates, when $D_i = 1$ that such a collision will take place. Therefore,

$$n_i - D_i$$

is the number of particles left in direction \vec{c}_i due to a two-particle collision along this direction.

Now, when $n_i = 0$, a new particle can appear into direction \vec{c}_i , as the result of a collision between n_{i+1} and n_{i+4} or a collision between n_{i-1} and n_{i+2} . It is convenient to introduce a random Boolean variable $q(\vec{r}, t)$ which decides whether the particles are deflected to the right ($q = 1$) or to the left ($q = 0$) when a two-body collision takes place. Therefore, the number of particle created into direction \vec{c}_i is

$$q D_{i-1} + (1 - q) D_{i+1}.$$

Particles can also be created into (or removed from) direction \vec{c}_i because of a three-body collision. The quantity which expresses the occurrence of a three-body collision with particles n_i , n_{i+2} and n_{i+4} is

$$T_i = n_i n_{i+2} n_{i+4} (1 - n_{i+1}) (1 - n_{i+3}) (1 - n_{i+5}). \quad (3.3)$$

As before, the result of a three-body collision is to modify the number of particles in direction \vec{c}_i as

$$n_i - T_i + T_{i+3}.$$

Thus, in full generality, the microdynamics of a LGA is written as

$$n_i(\vec{r} + \Delta_r \vec{c}_i, t + \Delta_t) = n_i(\vec{r}, t) + \Omega_i(n(\vec{r}, t)), \quad (3.4)$$

where Ω_i is called the collision term.

For the FHP model, Ω_i is defined so as to reproduce the collisions, that is

$$\Omega_i(n) = -D_i + qD_{i-1} + (1 - q)D_{i+1} - T_i + T_{i+3}. \quad (3.5)$$

Using the full expression for D_i and T_i , we obtain

$$\begin{aligned} \Omega_i(n) = & -n_i n_{i+2} n_{i+4} (1 - n_{i+1}) (1 - n_{i+3}) (1 - n_{i+5}) \\ & + n_{i+1} n_{i+3} n_{i+5} (1 - n_i) (1 - n_{i+2}) (1 - n_{i+4}) \\ & - n_i n_{i+3} (1 - n_{i+1}) (1 - n_{i+2}) (1 - n_{i+4}) (1 - n_{i+5}) \\ & + (1 - q) n_{i+1} n_{i+4} (1 - n_i) (1 - n_{i+2}) (1 - n_{i+3}) (1 - n_{i+5}) \\ & + q n_{i+2} n_{i+5} (1 - n_i) (1 - n_{i+1}) (1 - n_{i+3}) (1 - n_{i+4}). \end{aligned} \quad (3.6)$$

These equations are easy to code in a computer and yield a fast and exact implementation of the model. As an example, Fig. 25 illustrates a sound wave in the FHP gas at rest. Note that, usually, the so-called FHP-III model [66], which include a rest particle and a more complete set of collisions, is preferred when simulating a fluid, due to better physical properties.

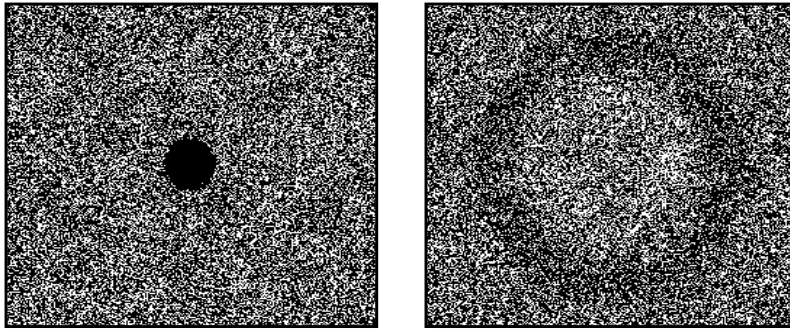


Fig. 25. Development of a sound wave in a FHP gas, due to an over particle concentration in the middle of the system.

3.3. The macroscopic variables

In a lattice gas automaton, the physical quantities of interest are not so much the Boolean variables n_i but macroscopic quantities or average values, such as, for instance, the average density of particles and the average velocity field at each point of the system. These quantities are defined from the ensemble average $N_i(\vec{r}, t) = \langle n_i(\vec{r}, t) \rangle$ of the microscopic occupation variables. $N_i(\vec{r}, t)$ is also the probability of having a particle entering site \vec{r} , at time t , with velocity $\vec{v}_i = (\Delta_r/\Delta_t)\vec{c}_i$.

In general, a LGA is characterized by the number z of lattice directions and the spatial dimensionality d . For a square lattice in $d = 2$ dimensions, we have $z = 4$, whereas, for a hexagonal lattice, $z = 6$. It is also convenient to add a $(z + 1)^{\text{th}}$ direction, $i = 0$, corresponding to a population of rest particles for which, obviously, $\vec{v}_0 = 0$.

Following the usual definition of statistical mechanics, the local density of particles is the sum of the average number of particles traveling along each direction \vec{c}_i

$$\rho(\vec{r}, t) = \sum_{i=0}^z N_i(\vec{r}, t). \quad (3.7)$$

Similarly, the particle current, which is the density ρ times the velocity field \vec{u} , is expressed by

$$\rho(\vec{r}, t)\vec{u}(\vec{r}, t) = \sum_{i=1}^z \vec{v}_i N_i(\vec{r}, t). \quad (3.8)$$

Another quantity which will play an important role in the up coming derivation is the momentum tensor Π defined as

$$\Pi_{\alpha\beta} = \sum_{i=1}^z v_{i\alpha} v_{i\beta} N_i(\vec{r}, t), \quad (3.9)$$

where the greek indices α and β label the d spatial components of the vectors. The quantity Π represents the flux of the α -component of momentum transported along the β -axis. This term will contain the pressure contribution and the effects of viscosity.

3.4. Multiscale Chapman–Enskog expansion

It is important to show that the discrete CA world is, at some appropriate scale of observation, governed by admissible equations: the physical conservation laws and the symmetry of the space are to be present and the discreteness of the lattice should not show up. The connection between the microscopic Boolean dynamics and the macroscopic, continuous world has to be established in order to assess the validity of the model.

In what follows we restrict the discussion to the case where all speeds \vec{v}_i have the same modulus and no particle at rest exists.

The starting point to obtain the macroscopic behavior of the CA fluid is to derive an equation for the N_i 's. Averaging the microdynamics (3.4) yields

$$N_i(\vec{r} + \Delta_r \vec{c}_i, t + \Delta_t) - N_i(\vec{r}, t) = \langle \Omega_i \rangle, \quad (3.10)$$

where Ω_i is the collision term of the LGA under study. It is important to notice that $\Omega_i(n)$ has some generic properties, namely

$$\sum_{i=1}^z \Omega_i = 0, \quad \sum_{i=1}^z \vec{v}_i \Omega_i = 0 \quad (3.11)$$

expressing the fact that particle number and momentum are conserved during the collision process (the incoming sum of mass or momentum equals the outgoing sum). If more conservation laws exist (e.g. energy), the collision term should reflect them. It is also expected that no extra quantities are conserved in addition to the physical ones. This is usually not the case: spurious invariants are found in several lattice models [19, 33, 94, 191, 127] and they may affect the physical behavior.

Equation (3.10) is still discrete in space and time. The N_i 's vary between 0 and 1 and, at a scale $L \gg \Delta_r$, $T \gg \Delta_t$, one can expect them to be smooth functions of the space and time coordinates. Therefore, Eq. (3.10) can be Taylor expanded up to second order and gives

$$\begin{aligned} \Delta_t \partial_t N_i + \Delta_r (\vec{c}_i \cdot \nabla) N_i + \frac{\Delta_t^2}{2} \partial_t^2 N_i + \frac{\Delta_r^2}{2} (\vec{c}_i \cdot \nabla)^2 N_i \\ + \Delta_r \Delta_t (\vec{c}_i \cdot \nabla) \partial_t N_i = \langle \Omega_i \rangle. \end{aligned} \quad (3.12)$$

The macroscopic limit of a LGA dynamics will require the solution of this equation. However, under the present form, there is little hope to solve it. Several approximations will be needed. At some point, it will be necessary to use the so-called Boltzmann assumption saying that N_i and N_j are uncorrelated if $i \neq j$, and to approximate $\langle \Omega_i(n) \rangle$ as $\Omega_i(N)$ (with all random Boolean variables replaced by their average values).

Then, we will have to solve a non-linear equation, which can be handled provided that we use a perturbation technique. For this purpose, we need a small parameter ϵ . As we said we are interested to observe the system at a macroscopic scale $L \ll \Delta_r$. Thus, we introduce a new space variable \vec{r}_1 such that

$$\vec{r}_1 = \epsilon \vec{r}, \quad \partial_{\vec{r}} = \epsilon \partial_{\vec{r}_1} \quad (3.13)$$

with $\epsilon \gg 1$.

Unfortunately, the equation we obtain by substituting into Eq. (3.12) $\partial_{\vec{r}}$ with its expression in terms of \vec{r}_1 cannot be solved with a naive perturbation method. It is necessary to introduce several time scales, otherwise divergences will occur. Following the procedure of the so-called multiscale expansion (see for instance Ref. 138), we introduce the extra time variables t_1 and t_2 , as well as new functions N_i^ϵ depending on \vec{r}_1 , t_1 and t_2

$$N_i^\epsilon = N_i^\epsilon(t_1, t_2, \vec{r}_1).$$

42 *B. Chopard, et al.*

Suppose that now we formally substitute into Eq. (3.12)

$$N_i \rightarrow N_i^\epsilon, \quad \partial_t \rightarrow \epsilon \partial_{t_1} + \epsilon^2 \partial_{t_2}, \quad \partial_r \rightarrow \epsilon \partial_{\vec{r}_1} \quad (3.14)$$

together with the corresponding expressions for the second order derivatives. Rigorously, we have no reason to consider only two time scales. However this will be enough here and, from a physical standpoint, we may anticipate that t_1 will be the scale giving the convective phenomena, while t_2 will describe dissipative processes.

After substitution in Eq. (3.14), we then obtain new equations for the new functions N_i^ϵ . The advantage is that, now, these equations can be solved by a perturbation method and the divergences removed [138]. Thus, we may write

$$N_i^\epsilon = N_i^{(0)} + \epsilon N_i^{(1)} + \epsilon^2 N_i^{(2)} + \dots \quad (3.15)$$

In addition we notice that, on the region,

$$t_1 = \epsilon t, \quad t_2 = \epsilon^2 t,$$

we precisely have the equality

$$\partial_t = \epsilon \partial_{t_1} + \epsilon^2 \partial_{t_2} \quad (3.16)$$

and our new equations have for solutions

$$N_i^\epsilon(\epsilon t, \epsilon^2 t, \epsilon \vec{r}_1) = N_i(t, \vec{r}).$$

From now on, we shall omit the superscript ϵ on N_i because we are only interested in what happens when $t_1 = \epsilon t$ and $t_2 = \epsilon^2 t$.

3.5. Chapman–Enskog procedure

The Chapman–Enskog method is the standard procedure used in statistical mechanics to solve an equation like Eq. (3.12) with a perturbation parameter ϵ . Assuming that $\langle \Omega_i(n) \rangle$ can be factorized into $\Omega_i(N)$, we write the contributions of each order in ϵ . According to multiscale expansion (3.15), the right-hand side of Eq. (3.12) reads

$$\Omega_i(N) = \Omega_i(N^{(0)}) + \epsilon \sum_{j=1}^z \left(\frac{\partial \Omega_i(N^{(0)})}{\partial N_j} \right) N_j^{(1)} + O(\epsilon^2).$$

Using expressions (3.15), (3.16) and (3.13) for N_i , ∂_t and ∂_r in the left-hand side of (3.12) yields the following conditions for the first two orders in ϵ

$$O(\epsilon^0) : \quad \Omega_i(N^{(0)}) = 0 \quad (3.17)$$

and

$$O(\epsilon^1) : \quad \partial_{t_1} N_i^{(0)} + \partial_{1\alpha} v_{i\alpha} N_i^{(0)} = \frac{1}{\Delta t} \sum_{j=1}^z \left(\frac{\partial \Omega_i(N^{(0)})}{\partial N_j} \right) N_j^{(1)}, \quad (3.18)$$

where the subscript 1 in spatial derivatives (e.g. $\partial_{1\alpha}$) indicates a differential operator expressed in the variable \vec{r}_1 .

The first equation determines the $N_i^{(0)}$'s. Once they are known, they can be substituted into the second equation in order to obtain a solution for the $N_i^{(1)}$. Unfortunately, this procedure is not as simple as it first looks, because the matrix $(\partial\Omega/\partial N)$ (whose elements are $\partial\Omega_i/\partial N_j$) is not invertible, due to the conservation laws (3.11). Indeed

$$\sum_i \left(\frac{\partial\Omega_i}{\partial N_j} \right) = \frac{\partial}{\partial N_j} \sum_i \Omega_i = 0$$

and, similarly

$$\sum_i v_{i\alpha} \left(\frac{\partial\Omega_i}{\partial N_j} \right) = 0.$$

Thus, the columns of the matrix $(\partial\Omega/\partial N)$ are linear combinations of each other and the determinant is zero. The above two equations can also be written as:

$$\left(\frac{\partial\Omega}{\partial N} \right)^T E_0 = 0, \quad \left(\frac{\partial\Omega}{\partial N} \right)^T E_\alpha = 0, \quad 1 \leq \alpha \leq d, \quad (3.19)$$

where the quantities E_0 and E_α are called the *collisional invariants* and are vectors of \mathbf{R}^z defined as:

$$\begin{aligned} E_0 &= (1, \dots, 1), \\ E_\alpha &= (v_{1\alpha}, \dots, v_{z\alpha}). \end{aligned} \quad (3.20)$$

The reason the E_α are called collisional invariants is because they described the conserved quantities of the dynamics, namely

$$N \cdot E_0 = \rho, \quad N \cdot E_\alpha = \rho u_\alpha, \quad (3.21)$$

where \cdot denotes the scalar product in \mathbf{R}^z .

In order for Eq. (3.18) to have a solution, it is necessary that $\partial_{t_1} N_i^{(0)} + \partial_{1\alpha} v_{i\alpha} N_i^{(0)}$ be in the image space of $(\partial\Omega/\partial N)$. It is well known from linear algebra that the image of a matrix is orthogonal (in the sense of the scalar product) to the kernel of its transpose

$$\text{Im} \left(\frac{\partial\Omega}{\partial N} \right) = \left[\text{Ker} \left(\frac{\partial\Omega}{\partial N} \right)^T \right]^\perp. \quad (3.22)$$

Therefore, the solubility condition of Eq. (3.18) requires that $\partial_{t_1} N_i^{(0)} + \partial_{1\alpha} v_{i\alpha} N_i^{(0)}$ be orthogonal to E_0 , E_1 and E_2 . We shall see in the next section that this condition is satisfied (Eqs. 3.25) and (3.26)).

Finally, note that when a solution to Eq. (3.18) exists, it is not unique (again, due to the fact that $(\partial\Omega/\partial N)$ is not invertible). For this reason, we also impose the extra conditions that the macroscopic quantities ρ and $\rho\vec{u}$ are entirely given by the zero order of expansion (3.15)

$$\rho = \sum_{i=1}^z N_i^{(0)}, \quad \rho\vec{u} = \sum_{i=1}^z \vec{v}_i N_i^{(0)} \quad (3.23)$$

44 *B. Chopard, et al.*

and, therefore

$$\sum_{i=1}^z N_i^{(\ell)} = 0, \quad \sum_{i=1}^z \vec{v}_i N_i^{(\ell)} = 0, \quad \text{for } \ell \geq 1. \quad (3.24)$$

In other words, this amounts to asking that the solution $N^{(1)}$ is also orthogonal to the collisional invariants and belongs to $\text{Im}(\partial\Omega/\partial N)$.

3.6. Balance equations

Before we solve equations (3.17) and (3.18), remember that we are interested in the behavior of the macroscopic quantities ρ and $\rho\vec{u}$. Conservation laws (3.11) imply some important balance equation for these variables.

Summing Eq. (3.12) over i yields zero for the right-hand side. The same is true if we first multiply (3.12) with \vec{v}_i before summing. If, again, we express (3.12) in terms of \vec{r}_1 , t_1 , t_2 and $N_i^{(\ell)}$ we obtain (using Eq. (3.23)) the following result at order ϵ :

$$O(\epsilon) : \quad \partial_{t_1} \rho + \text{div}_1 \rho \vec{u} = 0 \quad (3.25)$$

and

$$O(\epsilon) : \quad \partial_{t_1} \rho u_\alpha + \partial_{1\beta} \Pi_{\alpha\beta}^{(0)} = 0. \quad (3.26)$$

The quantity $\Pi_{\alpha\beta}^{(0)} = \sum_i \vec{v}_{i\alpha} \vec{v}_{i\beta} N_i^{(0)}$ is the zero order approximation of the momentum tensor defined in Eq. (3.9). One recognizes in Eq. (3.25) the usual continuity equation, while Eq. (3.26) expresses momentum conservation and corresponds to the Euler's equation of hydrodynamics, in which dissipative effects are absent.

The same calculation can be repeated for the order $O(\epsilon^2)$. Remembering relations (3.24), we find

$$\partial_{t_2} \rho + \frac{\Delta_t}{2} \partial_{t_1}^2 \rho + \frac{\Delta_t}{2} \partial_{1\alpha} \partial_{1\beta} \Pi_{\alpha\beta}^{(0)} + \Delta_t \partial_{t_1} \partial_{1\alpha} \rho u_\alpha = 0 \quad (3.27)$$

and

$$\partial_{t_2} \rho u_\alpha + \partial_{1\beta} \Pi_{\alpha\beta}^{(1)} + \frac{\Delta_t}{2} \partial_{t_1}^2 \rho u_\alpha + \frac{\Delta_t}{2} \partial_{1\beta} \partial_{1\gamma} S_{\alpha\beta\gamma}^{(0)} + \Delta_t \partial_{t_1} \partial_{1\beta} \Pi_{\alpha\beta}^{(0)} = 0, \quad (3.28)$$

where S is the third-order tensor

$$S_{\alpha\beta\gamma} = \sum_{i=1}^z v_{i\alpha} v_{i\beta} v_{i\gamma} N_i. \quad (3.29)$$

These last two equations can be simplified using relations (3.25) and (3.26). Let us first consider the case of Eq. (3.27). One has

$$\frac{\Delta_t}{2} \partial_{t_1}^2 \rho = -\frac{\Delta_t}{2} \partial_{t_1} \partial_{1\alpha} \rho u_\alpha \quad (3.30)$$

and, therefore

$$\begin{aligned} \frac{\Delta_t}{2} \partial_{t_1}^2 \rho + \frac{\Delta_t}{2} \partial_{1\alpha} \partial_{1\beta} \Pi_{\alpha\beta}^{(0)} + \Delta_t \partial_{t_1} \partial_{1\alpha} \rho u_\alpha \\ = \frac{\Delta_t}{2} \partial_{1\alpha} \left[\partial_{t_1} \rho u_\alpha + \partial_{1\beta} \Pi_{\alpha\beta}^{(0)} \right] = 0. \end{aligned} \quad (3.31)$$

Thus, Eq. (3.27) reduces to

$$\partial_{t_2} \rho = 0. \quad (3.32)$$

Similarly, since

$$\frac{\Delta_t}{2} \partial_{t_1}^2 \rho u_\alpha = -\frac{\Delta_t}{2} \partial_{t_1} \partial_{1\beta} \Pi_{\alpha\beta}^{(0)},$$

Eq. (3.28) becomes

$$\partial_{t_2} \rho u_\alpha + \partial_{1\beta} \left[\Pi_{\alpha\beta}^{(1)} + \frac{\Delta_t}{2} \left(\partial_{t_1} \Pi_{\alpha\beta}^{(0)} + \partial_{1\gamma} S_{\alpha\beta\gamma}^{(0)} \right) \right] = 0. \quad (3.33)$$

This last equation contains the dissipative contributions to the Euler equation (3.26). The first contribution is $\Pi_{\alpha\beta}^{(1)}$ which is the dissipative part of the momentum tensor. The second part, namely $\frac{\Delta_t}{2} \left(\partial_{t_1} \Pi_{\alpha\beta}^{(0)} + \partial_{1\gamma} S_{\alpha\beta\gamma}^{(0)} \right)$ comes from the second order terms of the Taylor expansion of the discrete Boltzmann equation. These terms account for the discreteness of the lattice and have no counterpart in standard hydrodynamics. As we shall see, they will lead to the so-called *lattice viscosity*.

The order ϵ and ϵ^2 can be grouped together to give the general equations governing our system. Summing Eqs. (3.33) and (3.26) with the appropriate power of ϵ as factor gives

$$\partial_t \rho u_\alpha + \frac{\partial}{\partial r_\beta} \left[\Pi_{\alpha\beta} + \frac{\Delta_t}{2} \left(\epsilon \partial_{t_1} \Pi_{\alpha\beta}^{(0)} + \frac{\partial}{\partial r_\gamma} S_{\alpha\beta\gamma}^{(0)} \right) \right] = 0, \quad (3.34)$$

where we have used that $\partial_t = \epsilon \partial_{t_1} + \epsilon^2 \partial_{t_2}$ and $\partial_\alpha = \epsilon \partial_{1\alpha}$. Similarly, Eqs. (3.25) and (3.32) yield

$$\partial_t \rho + \text{div } \rho \vec{u} = 0 \quad (3.35)$$

which is the standard continuity equation. Equation (3.34) corresponds to the Navier–Stokes equation. With the present form, it is not very useful because the tensors Π and S are not given in terms of the quantities ρ and \vec{u} . To go further, we will have to solve Eqs. (3.17) and (3.18) to find an expression for $N_i^{(0)}$ and $N_i^{(1)}$ as a function of ρ and \vec{u} . However, for the time being, it is important to remember that the derivation of the continuity equation (3.35) and the Navier–Stokes equation (3.34) are solely based on very general considerations, namely that $\sum \Omega_i = \sum \vec{v}_i \Omega_i = 0$. The specific collision rules of the LGA under study (FHP for instance) do not affect the structure of these balance equations. However, the details of the collision rule will play a role for the explicit expression of Π and S .

3.7. Local equilibrium

We now turn to the problem of solving Eq. (3.17), together with conditions (3.23) in order to find $N_i^{(0)}$ as a function of ρ and $\rho\vec{u}$.

The solutions $N_i^{(0)}$ which make the collision term Ω vanish are known as the local equilibrium solutions. Physically, they correspond to a situation where the rate of each type of collision equilibrates. Since the collision time Δ_t is much smaller than the macroscopic observation time, it is reasonable to expect, in first approximation, that an equilibrium is reached locally.

Provided that the collision behaves reasonably, it is found [66] that the generic solution is

$$N_i^{(0)} = \frac{1}{1 + \exp(-A - \vec{B} \cdot \vec{v}_i)}. \quad (3.36)$$

This expression has the form of a Fermi–Dirac distribution. This is a consequence of the exclusion principle we have imposed in the cellular automata rule (no more than one particle per site and direction). This form is explicitly obtained for the FHP model by assuming that the rate of direct and inverse collisions are equal, namely

$$T_i(N^{(0)}) = T_{i+3}(N^{(0)})$$

and

$$\frac{1}{2}D_i(N^{(0)}) = \frac{1}{2}D_{i+1}(N^{(0)}), \quad \frac{1}{2}D_i(N^{(0)}) = \frac{1}{2}D_{i-1}(N^{(0)}).$$

The quantities A and \vec{B} in Eq. (3.36) are functions of the density ρ and the velocity field \vec{u} and are to be determined according to Eqs. (3.23). In order to carry out this calculation, $N_i^{(0)}$ is Taylor expanded, up to second order in the velocity field \vec{u} (i.e. second order in the Mach number). One obtains (see Ref. 33 for full details in the case the FHP model).

$$N_i^{(0)} = a\rho + \frac{b\rho}{v^2}\vec{v}_i \cdot \vec{u} + \frac{\rho G(\rho)}{v^4}Q_{i\alpha\beta}u_\alpha u_\beta, \quad (3.37)$$

where $v = \Delta_r/\Delta_t$ and

$$Q_{i\alpha\beta} = v_{i\alpha}v_{i\beta} - \frac{v^2}{d}\delta_{\alpha\beta}. \quad (3.38)$$

The coefficients entering this expression can be determined from (3.23). First we assume that the lattice velocities have the following important properties

$$\sum_{i=1}^z \vec{v}_i = \mathbf{0}, \quad (3.39)$$

$$\sum_{i=1}^z v_{i\alpha}v_{i\beta} = v^2 C_2 \delta_{\alpha\beta}, \quad (3.40)$$

$$\sum_{i=1}^z v_{i\alpha} v_{i\beta} v_{i\gamma} = 0, \quad (3.41)$$

$$\sum_{i=1}^z v_{i\alpha} v_{i\beta} v_{i\gamma} v_{i\delta} = v^4 C_4 (\delta_{\alpha\beta} \delta_{\gamma\delta} + \delta_{\alpha\gamma} \delta_{\beta\delta} + \delta_{\alpha\delta} \delta_{\beta\gamma}), \quad (3.42)$$

These conditions express the isotropy of tensors up to fourth order on the lattice. These properties are necessary in order for the CA fluid flow to be isotropic (i.e. independent of a specific lattice orientation), up to order u^2 . They hold for the hexagonal lattice with $C_2 = 3$ and $C_4 = 3/4$ (see Refs. 33, 187), but Eq. (3.42) is wrong for a 2-D square lattice and that is the reason why the FHP model is defined on a hexagonal lattice.

From Eq. (3.40), one has $\sum_i v_{i\alpha} v_{i\alpha} = v^2 C_2 \delta_{\alpha\alpha} = v^2 d C_2$. On the other hand, if all \vec{v}_i have same modulus v , a direct calculation gives $\sum_i v_{i\alpha} v_{i\alpha} = z v^2$. Thus

$$C_2 = \frac{z}{d}.$$

Similarly, using Eq. (3.42),

$$\sum_{i=0}^z v_{i\alpha} v_{i\beta} v_{i\gamma} v_{i\gamma} = v^4 C_4 (d \delta_{\alpha\beta} + \delta_{\alpha\beta} + \delta_{\alpha\beta}) = v^4 (d+2) C_4 \delta_{\alpha\beta}.$$

Again, if all \vec{v}_i are of same length, $\sum_{i=0}^z v_{i\alpha} v_{i\beta} v_{i\gamma} v_{i\gamma} = v^2 \sum_{i=0}^z v_{i\alpha} v_{i\beta}$ and, from Eq. (3.40), it is equal to $v^4 C_2$. Therefore,

$$C_4 = \frac{C_2}{d+2} = \frac{z}{d(d+2)}.$$

Using the above properties, it is easy to see that $\sum_i Q_{i\alpha\beta} = \sum_i Q_{i\alpha\beta} v_{i\gamma} = 0$. Thus the determination of the values of a and b is straightforward from Eq. (3.23);

$$\rho = \sum_{i=1}^z N_i^{(0)} = a z \rho, \quad \rho \vec{u}_\alpha = \sum_{i=1}^z \vec{v}_{i\alpha} N_i^{(0)} = b C_2 \rho u_\alpha.$$

Hence,

$$a = \frac{1}{z}, \quad b = \frac{1}{C_2} = \frac{d}{z}.$$

The function G is obtained from the fact that $N_i^{(0)}$ is the Taylor expansion of a Fermi-Dirac distribution. For FHP, it is found that [33, 66]

$$G(\rho) = \frac{2(3-\rho)}{3(6-\rho)}.$$

The fact that $G(p)$ is not equal to 1 and depends on ρ expresses the lack of Galilean invariance of the CA fluid. Note that adding several rest particles to the model is a way to restore gradually this invariance.

48 *B. Chopard, et al.*

We may now compute the local equilibrium part of the momentum tensor, $\Pi_{\alpha\beta}^{(0)}$. This calculation requires multiplying Eq. (3.37) by $v_{i\alpha}v_{i\beta}$ and summing over i .

$$\begin{aligned}\Pi_{\alpha\beta}^{(0)} &= \sum_i N_i^{(0)} v_{i\alpha} v_{i\beta} \\ &= \rho a C_2 v^2 \delta_{\alpha\beta} - \frac{C_2 \rho}{d} G(\rho) u^2 \delta_{\alpha\beta} + C_4 \rho G(\rho) (u^2 \delta_{\alpha\beta} + 2u_\alpha u_\beta) \\ &= \left(a C_2 v^2 \rho - \left[\frac{C_2}{d} - C_4 \right] \rho G(\rho) u^2 \right) \delta_{\alpha\beta} + 2C_4 \rho G(\rho) u_\alpha u_\beta.\end{aligned}\quad (3.43)$$

The quantity

$$p = \left(a C_2 v^2 \rho - \left[\frac{C_2}{d} - C_4 \right] \rho G(\rho) u^2 \right) \quad (3.44)$$

is called the pressure term and $2C_4 G(\rho) \rho u_\alpha u_\beta$ the convective part of the momentum tensor. Thus the microdynamics gives an explicit expression for the pressure. The term $a C_2 v^2 \rho$ corresponds to a perfect gas contribution, at fixed temperature. It is usually written as

$$p = \rho c_s^2, \quad (3.45)$$

where c_s is the speed of sound. From this relation, we may identify

$$c_s^2 = a C_2 v^2 = v^2/d.$$

The other term, containing a u^2 dependence is not physical and imply a spurious behavior. This contribution can be suppressed in LB models (see Sec. 4).

Note that in the FHP model, the temperature is not defined and the balance equation for the kinetic energy is identical to the mass conservation equation, since all particles have the same velocities. Temperature has been introduced in multi-speed lattice gas models, through the equipartition theorem [32, 73, 49].

3.8. Correction to local equilibrium

The next step is to compute the terms involved in the Navier–Stokes equation (3.34)

$$\partial_t \rho u_\alpha + \frac{\partial}{\partial r_\beta} \left[\Pi_{\alpha\beta}^{(0)} + \epsilon \Pi_{\alpha\beta}^{(1)} + \frac{\Delta_t}{2} \left(\epsilon \partial_{t_1} \Pi_{\alpha\beta}^{(0)} + \frac{\partial}{\partial r_\gamma} S_{\alpha\beta\gamma}^{(0)} \right) \right] = 0. \quad (3.46)$$

We shall restrict ourselves to first order in the velocity field u .

The lattice viscosity: From Eq. (3.43) we have

$$\Pi_{\alpha\beta}^{(0)} = c_s^2 \rho \delta_{\alpha\beta} + O(u^2).$$

Since $\partial_{t_1} \rho = -\text{div}_1 \rho \vec{u}$ (from Eq. (3.25)), one has $\epsilon \partial_{t_1} \rho = -\text{div} \rho \vec{u}$ and

$$\frac{\Delta_t}{2} \frac{\partial}{\partial r_\beta} \epsilon \partial_{t_1} \Pi_{\alpha\beta}^{(0)} = \frac{\Delta_t c_s^2}{2} \frac{\partial}{\partial r_\beta} \epsilon \partial_{t_1} \rho \delta_{\alpha\beta} = -\frac{\Delta_t c_s^2}{2} \frac{\partial \text{div} \rho \vec{u}}{\partial r_\alpha}. \quad (3.47)$$

To compute the term involving

$$S_{\alpha\beta\gamma}^{(0)} = \sum_{i=1}^z v_{i\alpha} v_{i\beta} v_{i\gamma} N_i^{(0)},$$

we first notice that the only contribution to $N_i^{(0)}$ given by Eq. (3.37) will be $N_i^{(0)} = [\rho b/v^2] \vec{v}_i \cdot \vec{u}$ because the other terms contain an odd number of \vec{v}_i . Thus, using Eq. (3.42),

$$S_{\alpha\beta\gamma}^{(0)} = v^2 C_4 b \rho (\delta_{\alpha\beta} u_\gamma + \delta_{\alpha\gamma} u_\beta + \delta_{\beta\gamma} u_\alpha)$$

and

$$\frac{\Delta_t}{2} \frac{\partial^2}{\partial r_\beta \partial r_\gamma} S_{\alpha\beta\gamma}^{(0)} = \frac{\Delta_t v^2}{2} C_4 b \nabla^2 \rho u_\alpha + \Delta_t v^2 C_4 b \frac{\partial}{\partial r_\alpha} \operatorname{div} \rho \vec{u}. \quad (3.48)$$

Substituting the results (3.47) and (3.48) into the Navier–Stokes equation (3.46) yields

$$\begin{aligned} \partial_t \rho u_\alpha + \frac{\partial}{\partial r_\beta} \Pi_{\alpha\beta}^{(0)} &= -\frac{\partial}{\partial r_\beta} \epsilon \Pi_{\alpha\beta}^{(1)} - \frac{\Delta_t v^2}{2} C_4 b \nabla^2 \rho u_\alpha \\ &\quad - \Delta_t \left[v^2 C_4 b - \frac{c_s^2}{2} \right] \frac{\partial}{\partial r_\alpha} \operatorname{div} \rho \vec{u}. \end{aligned} \quad (3.49)$$

The last term vanishes since $v^2 C_4 b - c_s^2/2 = 0$ and the other term has the form of a viscous effect $\nu_{\text{lattice}} \nabla^2 \rho \vec{u}$, where

$$\nu_{\text{lattice}} = -C_4 b \frac{\Delta_t v^2}{2} = -\frac{\Delta_t v^2}{2(d+2)}. \quad (3.50)$$

where ν_{lattice} is a *negative* viscosity. The origin of this contribution is the discreteness of the lattice ($S_{\alpha\beta\gamma}^{(0)}$ and $\partial_{t_1} \Pi_{\alpha\beta}^{(0)}$ comes from the Taylor expansion). For this reason, this term is referred to as a lattice contribution to the viscosity. The fact that it is negative is of no consequence because the last contribution $-\partial_\beta \epsilon \Pi_{\alpha\beta}^{(1)}$ which we still have to calculate will be positive and larger than the present one.

The collisional viscosity: The usual contribution to viscosity is due to the collision between the fluid particles. This contribution is captured by the term $\partial_\beta \epsilon \Pi_{\alpha\beta}^{(1)}$ in Eq. (3.49). In order to compute it, we first have to solve Eq. (3.18) for $N_i^{(1)}$. To lowest order in the velocity flow \vec{u} , we have

$$\begin{aligned} \frac{1}{\Delta_t} \sum_{j=1}^z \left(\frac{\partial \Omega_i(N^{(0)})}{\partial N_j} \right) N_j^{(1)} \\ &= \partial_{t_1} N_i^{(0)} + \partial_{1\alpha} v_{i\alpha} N_i^{(0)} \\ &= -\frac{\partial N_i^{(0)}}{\partial \rho} \operatorname{div}_1 \rho \vec{u} - \frac{\partial N_i^{(0)}}{\partial \rho u_\alpha} \partial_{1\beta} \Pi_{\alpha\beta}^{(0)} + \partial_{1\alpha} v_{i\alpha} N_i^{(0)}, \end{aligned} \quad (3.51)$$

50 *B. Chopard, et al.*

where we have expressed the time derivative of $N_i^{(0)}$ in terms of the derivatives with respect to ρ and ρu_α

$$\partial_{t_1} N_i^{(0)} = \frac{\partial N_i^{(0)}}{\partial \rho} \partial_{t_1} \rho + \frac{\partial N_i^{(0)}}{\partial \rho u_\alpha} \partial_{t_1} \rho u_\alpha \quad (3.52)$$

and used Eqs. (3.25) and (3.26) to express $\partial_{t_1} \rho$ and $\partial_{t_1} \rho u_\alpha$. These substitutions will ensure that the right-hand side of Eq. (3.51) is the image of $(\partial\Omega/\partial N)$.

As we did for the lattice viscosity, we shall only consider the first order in the velocity flow \vec{u} . The omitted terms are expected to be of the order $O(u^3)$. From the expressions (3.37) and (3.43), we have for the lowest order in \vec{u}

$$N_i^{(0)} = a\rho + \frac{b}{v^2} v_{i\alpha} \rho u_\alpha \quad \text{and} \quad \Pi_{\alpha\beta}^{(0)} = c_s^2 \rho \delta_{\alpha\beta}.$$

Thus

$$\frac{\partial N_i^{(0)}}{\partial \rho} = a \quad \text{and} \quad \frac{\partial N_i^{(0)}}{\partial \rho u_\alpha} = \frac{b v_{i\alpha}}{v^2},$$

and we can rewrite Eq. (3.51) as

$$\begin{aligned} \frac{1}{\Delta_t} \sum_{j=1}^z \left(\frac{\partial \Omega_i(N^{(0)})}{\partial N_j} \right) N_j^{(1)} &= -a \operatorname{div}_1 \rho \vec{u} - \frac{b v_{i\alpha}}{v^2} \partial_{1\beta} \Pi_{\alpha\beta}^{(0)} + \partial_{1\alpha} v_{i\alpha} N_i^{(0)} \\ &= \frac{b}{v^2} \left(v_{i\alpha} v_{i\beta} - \frac{v^2}{d} \delta_{\alpha\beta} \right) \partial_{1\beta} \rho u_\alpha \\ &= \frac{b}{v^2} Q_{i\alpha\beta} \partial_{1\beta} \rho u_\alpha. \end{aligned} \quad (3.53)$$

From this result, it is now clear that Eq. (3.51) will have a solution since, as noticed previously, the z -dimensional vectors $Q_{\alpha\beta}$ of component $Q_{i\alpha\beta}$ are orthogonal to the collisional invariants E_0 and E_γ . Since E_0 and E_α are in the kernel of $(\partial\Omega/\partial N)^T$, then $Q_{\alpha\beta}$ is in the image space of $(\partial\Omega/\partial N)$ (see Eq. (3.22)).

We now consider the left-hand side of Eq. (3.51), for $\vec{u} = 0$ (remember that we want to obtain the first contribution to $N_i^{(1)}$).

An interesting observation is that, in general, the vectors $Q_{\alpha\beta}$ are eigenvectors of the matrix $(\partial\Omega/\partial N)$. Thus we write

$$\left(\frac{\partial \Omega(N^{(0)})}{\partial N} \right)_{\vec{u}=0} Q_{\alpha\beta} = -\Lambda Q_{\alpha\beta},$$

where $-\Lambda$ is the associated eigenvalue (for FHP, it is found that $\Lambda = 3s(1-s)^3$, with $s = \rho/6$). This yields immediately the solution for $N^{(1)}$ as a multiple of $Q_{\alpha\beta}$. Since $Q_{\alpha\beta}$ is orthogonal to the collisional invariants, $N^{(1)}$ will clearly satisfy the extra conditions (3.24). Thus we have

$$N_i^{(1)} = -\frac{\Delta_t b}{\Lambda v^2} Q_{i\alpha\beta} \partial_{1\beta} \rho u_\alpha. \quad (3.54)$$

We may now compute the correction $\epsilon\Pi^{(1)}$ to the momentum tensor. Since $\epsilon\partial_{1\beta} = \partial_\beta$, we get

$$\begin{aligned}\epsilon\Pi_{\alpha\beta}^{(1)} &= \epsilon \sum_i N_i^{(1)} v_{i\alpha} v_{i\beta} \\ &= \frac{\Delta_t v^2 b}{\Lambda} \left[\frac{C_2}{d} \operatorname{div} \rho \vec{u} \delta_{\alpha\beta} - C_4 (\delta_{\alpha\beta} \delta_{\gamma\delta} + \delta_{\alpha\gamma} \delta_{\beta\delta} + \delta_{\alpha\delta} \delta_{\beta\gamma}) \partial_\gamma \rho u_\delta \right] \\ &= \Delta_t v^2 \frac{b}{\Lambda} \left[\left(\frac{C_2}{d} - C_4 \right) \operatorname{div} \rho \vec{u} \delta_{\alpha\beta} - C_4 (\partial_\alpha \rho u_\beta + \partial_\beta \rho u_\alpha) \right].\end{aligned}\quad (3.55)$$

3.9. The Navier–Stokes equation

We can now rewrite (to first order in ϵ and second order in the velocity flow \vec{u}), the Navier–Stokes equation (3.49). Using expression (3.43) for $\Pi_{\alpha\beta}^{(0)}$, we get

$$\begin{aligned}\partial_t \rho u_\alpha + \partial_\beta (\rho 2C_4 G(\rho) u_\alpha u_\beta) \\ = -\nabla p - \frac{\Delta_t v^2}{2} C_4 b \nabla^2 \rho u_\alpha \\ - \partial_\beta \left[\Delta_t v^2 \frac{b}{\Lambda} \left(\frac{C_2}{d} - C_4 \right) (\delta_{\alpha\beta} \operatorname{div} \rho \vec{u} - C_4 (\partial_\alpha u_\beta + \partial_\beta u_\alpha)) \right],\end{aligned}\quad (3.56)$$

where the pressure p is given by relation (3.44)

In the limit of low Mach number, the density can be assumed to be a constant, except in the pressure term [171]. From the continuity equation (3.35), we then get $\operatorname{div} \rho \vec{u} = 0$ and

$$\begin{aligned}\frac{1}{\rho} \partial_\beta \epsilon \Pi_{\alpha\beta}^{(1)} &= -\frac{1}{\rho} \Delta_t v^2 \frac{b C_4}{\Lambda} [\partial_\alpha \partial_\beta \rho u_\beta + \rho \partial_\beta^2 u_\alpha] \\ &= -\nu_{\text{coll}} \nabla^2 u_\alpha\end{aligned}\quad (3.57)$$

with

$$\nu_{\text{coll}} = \Delta_t v^2 \frac{b C_4}{\Lambda}.$$

Within this approximation, equation (3.56) can be cast into

$$\partial_t \vec{u} + 2C_4 G(\rho) (\vec{u} \cdot \nabla) \vec{u} = -\frac{1}{\rho} \nabla p + \nu \nabla^2 \vec{u}.\quad (3.58)$$

The quantity ν is the kinematic viscosity of our discrete fluid, whose expression is composed of the lattice and collisional viscosities

$$\nu = \Delta_t v^2 b C_4 \left(\frac{1}{\Lambda} - \frac{1}{2} \right) = \frac{\Delta_t v^2}{d+2} \left(\frac{1}{\Lambda} - \frac{1}{2} \right).\quad (3.59)$$

The presence of the coefficient C_4 for the viscosity indicates that our results relies on the isotropy of the fourth order tensor $\sum_i v_{i\alpha} v_{i\beta} v_{i\gamma} v_{i\delta}$. Thus, for a 2D square lattice (e.g. the HPP model), a viscosity cannot be defined, even in the first order in \vec{u} .

For the FHP model, the viscosity depends strongly on the density ($\Lambda = (\rho/2)[1 - (\rho/6)]^3$) and may become arbitrarily large for the limiting values $\rho = 0$ and $\rho = 6$. Its minimal value is obtained for $\rho = 3/2$.

Whereas the form of Eq. (3.58) depends little on the type of collision the particles experience, the expression (3.59) is very sensitive to the collision processes, through the value of Λ . In a lattice gas dynamics, the viscosity is intrinsic to the model and is not an adjustable parameter. In order to change the viscosity, collision rules should be modified. This is why the FHP model has been extended to obtain the FHP-III model with the lowest intrinsic viscosity.

Up to the factor of $2C_4G(\rho)$, Eq. (3.58) is the standard Navier–Stokes equation. The fact that the coefficient of the convective term $(\vec{u} \cdot \nabla)\vec{u}$ is different from 1 is an indication of the non-Galilean invariance of the model. However, if we assume that $\rho \simeq \text{const}$, this factor can be absorbed in a renormalization of the time and the lattice dynamics is described by the usual hydrodynamic equation.

In Sec. 4 we shall see that Galilean invariance can be restored in a more general way when using a lattice Boltzmann dynamics. Also, viscosity will be an adjustable parameter.

3.10. A two-phase CA fluid

The ability of a cellular automata fluids, like FHP, to model a real fluid depends very much on the application one considers. It is not appropriate to simulate high Reynolds flows (because the viscosity is too high), but can be very useful to describe situations with complicated boundary conditions (porous media) and multi-phase or reactive flows (see for instance Refs. 24, 76, 86, 153, 155).

In this section we consider a two-phase cellular automata fluid. Each particle of the fluid can be in two possible states, say $s = 1$ or $s = -1$. If we call this extra degree of freedom a *spin*, this fluid can be compared with an Ising system in which, the spins can move according to some hydrodynamics rules.

We consider an interaction between nearest neighbors similar to that found in classical dynamical Ising models. This will produce a surface tension effect at the interface between the two phases. The introduction of such an interaction requires real-valued fields (like the temperature) and, thus, the present model goes beyond a simple, fully discrete cellular automaton.

It is interesting to remark that, in addition to being a binary fluid model, this system has some of the ingredients of a ferrofluid [151], if the spin is interpreted as the magnetization carried by the particles.

The collision rule: Before we define more precisely the spin interaction, let us return to the particle motion. A collision rule which conserves mass, momentum and *spin* can be defined in analogy with the FHP rule described in Sec. 3.1.

We denote by $s_i(\vec{r}, t) \in \{-1, 0, 1\}$ the state of the automaton along lattice direction i at site \vec{r} and time t ($s_i = 0$ means an absence of particles). Clearly the

presence of a particle is characterized by $s_i^2 = 1$, regardless of its spin. Thus, the collision term can be obtained by using s_i^2 as an occupation number.

When a collision takes place, the particles are redistributed among the lattice directions but the same number of spin +1 and -1 particles should be present in the output state as there were in the input state. A way to guarantee this spin conservation is to assume that the particles are distinguishable, at least for what concerns their spin.

Therefore the full collision of a Ising fluid obeying FHP-like collision reads

$$\begin{aligned}
 s_i(\vec{r} + \Delta_r \vec{c}_i, t + \Delta_t) &= s_i - s_i s_{i+2}^2 s_{i+4}^2 (1 - s_{i+1}^2)(1 - s_{i+3}^2)(1 - s_{i+5}^2) \\
 &\quad + s_{i+3} s_{i+1}^2 s_{i+5}^2 (1 - s_i^2)(1 - s_{i+2}^2)(1 - s_{i+4}^2) \\
 &\quad - s_i s_{i+3}^2 (1 - s_{i+1}^2)(1 - s_{i+2}^2)(1 - s_{i+4}^2)(1 - s_{i+5}^2) \\
 &\quad + p q s_{i+1} s_{i+4}^2 (1 - s_i^2)(1 - s_{i+2}^2)(1 - s_{i+3}^2)(1 - s_{i+5}^2) \\
 &\quad + p(1 - q) s_{i+4} s_{i+1}^2 (1 - s_i^2)(1 - s_{i+2}^2)(1 - s_{i+3}^2)(1 - s_{i+5}^2) \\
 &\quad + (1 - p)(1 - q) s_{i+2} s_{i+5}^2 (1 - s_i^2)(1 - s_{i+1}^2)(1 - s_{i+3}^2)(1 - s_{i+4}^2) \\
 &\quad + (1 - p) q s_{i+5} s_{i+2}^2 (1 - s_i^2)(1 - s_{i+1}^2)(1 - s_{i+3}^2)(1 - s_{i+4}^2), \quad (3.60)
 \end{aligned}$$

where p and q are random Boolean variables that are 1 with probability 1/2, independently at each site and time step. These quantities select one of the two possible outcomes in the two-body collisions.

Spin interaction: An important part of this Ising fluid model is the interaction between spins at the same sites and spins sitting on adjacent lattice sites. This interaction produces the surface tension and can be adjusted through a parameter which corresponds to the temperature of the system (which is assumed to be uniform here).

The interaction we propose here does not conserve the number of spins of each sign. It only conserves the number of particles and, for this reason, does not represent two different fluids but two possible states of the same fluid. Of course, the miscibility or immiscibility of the two phases can be tuned through the temperature.

The updating rule for the spin dynamics is taken from the Monte-Carlo method [11], using the so-called Glauber transition rule. The main idea is that a spin flips (changes sign) if it can lower the local energy of the system. The energy of the pair of spin s_i and s_j is computed as $E = -J_1 s_i s_j$ if the two spins are nearest neighbors on the hexagonal lattice and $E = -J_0 s_i s_j$ if they both sit on the same site (remember that up to six particles can populate a given site).

However, a spin can flip even if this results in a local increase of energy. But, then, the change is accepted only with a probability $W(s \rightarrow -s)$ which depends on the temperature. In the Glauber dynamics, this probability is given by

$$W(s_i \rightarrow -s_i) = \frac{1}{2}(1 - s_i \tanh(E_i)),$$

54 *B. Chopard, et al.*

where E_i is the energy before the flip

$$E_i = \frac{1}{k_B T} (J_0 m_i + J_1 M_i) s_i$$

and $m_i = \sum_{j \neq i} s_j$ is the on-site “magnetization” seen by spin s_i and $M_i = \sum_{\langle ji \rangle} s_j$ is the “magnetization” carried by all the particles j on the neighboring sites of spin i . The quantity T is the temperature and k_B the Boltzmann constant that we can set to 1 when working with an arbitrary temperature scale. When more than one particle is present at a site, only one of them, chosen at random, is checked for such a spin flip.

The above transition rule is obtained from the detailed balance condition, namely

$$\frac{W(s_i \rightarrow -s_i)}{W(-s_i \rightarrow s_i)} = \frac{\exp\left(-\frac{E(-s_i)}{(k_B T)}\right)}{\exp\left(-\frac{E(s_i)}{(k_B T)}\right)},$$

where $E(\pm s_i)$ denotes the Ising energy as a function of s_i and it has the properties to drive an ergodic system to thermodynamic equilibrium.

As opposed to the standard the Monte-Carlo approach, where the lattice sites are visited sequentially and in a random way, here we update synchronously all the sites belonging to a given sub-lattice. Indeed, for the coherence of the dynamics it is important not to update simultaneously any two spins that are neighbors on the lattice. This is for the same reason as explained in Sec. 2.2 when we discussed the Q2R rule.

In a hexagonal lattice, it is easy to see that the space can be partitioned into three sub-lattices so that all the neighbors of one sub-lattice always belong to the two others (see Fig. 26).

Therefore, the spin interaction rule described above cycles over these three sub-lattices and alternate with the FHP particle motion given by Eq. (3.60).

It is of course possible to vary the relative frequency of the two rules (Glauber and FHP). For instance we can perform n successive FHP steps followed by m successive steps of the Ising rule in order to give more or less importance to the particle motion with respect to the spin flip. When $n = 0$ we have a pure Ising model on an hexagonal lattice but with possibly a different number of spins per site.

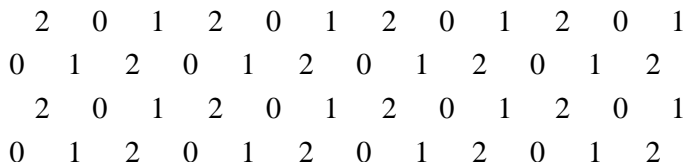


Fig. 26. The three sub-lattices on the hexagonal lattice used for the synchronous spin update. The values 0, 1, 2 label the sites according to the sub-lattice they belong to.

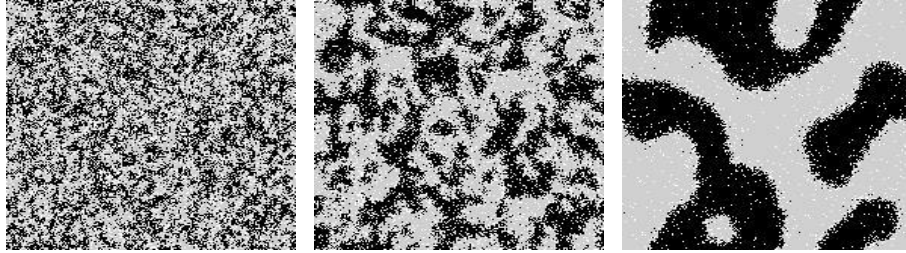


Fig. 27. Three snapshots of the evolution of the Ising FHP model below the critical temperature. Particles with spin +1 are shown in black while gray points show particles with -1. White cells indicate empty sites.

If the temperature is large enough and periodic boundary conditions are imposed, the system evolves to a configuration where, on average, there are the same amount of particles with spins up and down. Of course, the situation is not frozen and the particles keep moving and spins continuously flip. As in regular Ising systems, there is a critical temperature below which we can observe a global magnetization and the growth of domains containing one type of spin. This situation is illustrated in Fig. 27 and corresponds to the case $n = m = 1$, namely one spin update cycle followed by one step of FHP motion. It is observed that the critical temperature depends on the update frequency n and m .

Another interesting situation corresponds to the simulation of a Rayleigh–Taylor instability (see Fig. 28). Two immiscible fluids are on the top of each other and the heavier is above the lighter. Due to gravity, the upper fluid wants to penetrate

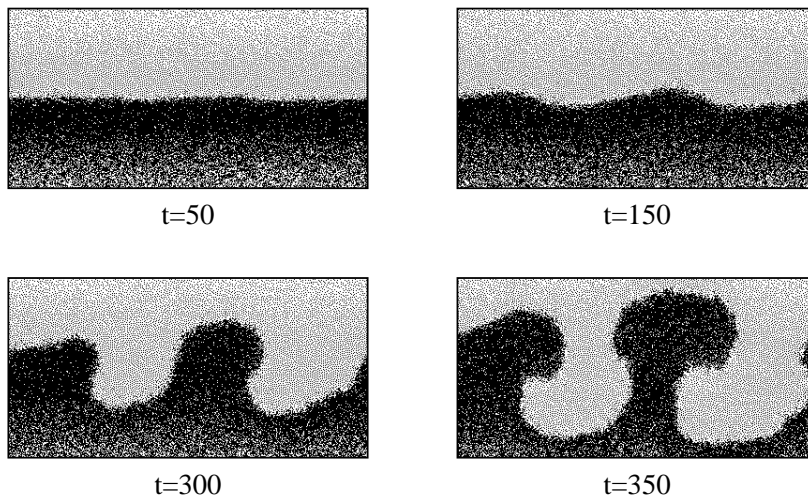


Fig. 28. Rayleigh–Taylor instability of the interface between two immiscible fluids. Particles with spin +1 are shown in black and are “lighter” than gray particles with having spin -1. An approximate immiscibility is obtained by choosing a low temperature in the model.

through the lower one. Since the two fluids are immiscible, the interface between them becomes unstable and, as time goes on, gives rise to a mushroom-like pattern.

An external force like gravity can be added to our model by deflecting with some probability (and when possible) the trajectory of particles in a given direction. Two immiscible fluids can be modeled by having a low temperature T in the Glauber dynamics so as to produce the necessary surface tension. The upper fluid layer is initialized with only particles of spin -1 , whereas the lower layer contains only spins $+1$. Gravity is adjusted so that “light” particles go up and heavy particles go down. After a few iterations, the flat interface destabilizes as shown in the last panel of Fig. 28.

4. The Lattice Boltzmann Method

Cellular automata fluids, such as those discussed in the previous section, represent idealized N-body systems. Their time evolution can be performed exactly on a computer, without many of the approximations usually done when computing numerically the motion of a fluid. In particular, there is no need, in a CA simulation to assume some factorization of the many-body correlation functions into a product of one-particle density functions.

Of course, the cellular automata model may be inadequate to represent a real situation but it includes naturally the intrinsic fluctuations present in any system composed of many particles. This feature is out of reach of most tractable numerical techniques. In many physical situations, spontaneous fluctuations and many-particle correlations can be safely ignored. This is however not always the case and, in Secs. 7.3 and 7.5, we shall see some examples of systems where intrinsic fluctuations are crucial.

On the other hand, a cellular automata simulation is very noisy (because it deals with Boolean quantities). In order to obtain the macroscopic behavior of a system (like the streaklines in a flow past an obstacle), one has to average the state of each cell over a rather large patch of cells (for instance a 32×32 square) and over several consecutive time steps. This requires larger systems and longer simulation times. Therefore, the benefit of the cellular automata approach over more traditional numerical techniques gets blurred [131] when simulating pure fluid flows in simple geometries.

In addition, due to its Boolean nature, cellular automata models offer little flexibility to finely adjust external parameters. Many tunings are done through probabilities, which is not always the most efficient way.

4.1. From Boolean to real-valued fields

When correlations can be neglected and the Boltzmann molecular chaos hypothesis is valid, it may be much more effective to directly simulate on the computer the lattice Boltzmann equation

$$N_i(\vec{r} + \Delta_r \vec{c}_i, t + \Delta_t) = N_i(\vec{r}, t) + \Omega_i(N) \quad (4.1)$$

with Ω_i given, for instance, by Eq. (3.6) with q replaced by $1/2$. It is more advantageous to average the microdynamics *before* simulating it rather than *after* doing it. The quantities of interest N_i are no longer Boolean variables but probabilities of presence which are continuous variable ranging in the interval $[0, 1]$.

A direct simulation of the lattice Boltzmann dynamics has been first considered by McNamara and Zanetti [121]. It considerably decreases the statistical noise that plague cellular automata models and considerably reduces the computational requirements. The main drawback of this approach is that it neglects many-body correlations and may become numerically unstable.

The lattice Boltzmann (LB) method has been widely used for simulating various fluid flows [144] and is believed to be a very serious candidate to overcome traditional numerical techniques of CFD (Computational Fluid Dynamics). Their microscopic level of description provide a natural interpretation of the numerical scheme and permits intuitive generalizations to complex flow problems (two-phase flow [74, 76, 155], magnetohydrodynamics [167], flow in porous media [1, 75] or thermohydrodynamics [2]).

The main weakness of current LB models is that they are defined on a regular lattices, while CFD techniques can deal with arbitrary irregular meshes. For some applications where the geometry cannot be fitted by a regular lattice, this is a strong limitation. Some efforts are now devoted to extend LB models to irregular lattices [166]. The succesful approach is probably to assume an underlying discrete velocity Boltzmann equation and express its evolution on a coarse grain discrete spatial mesh. As a tentative example, Sec. 6.3.3 shows a simple LB diffusion model in polar coordinates.

In a lattice Boltzmann fluid, the most natural way to define the collision term Ω_i , is to average the microdynamics of a given underlying cellular automata fluid and factorize it into a product of average quantities, as we did in Sec. 3 to get the Boltzmann approximation. However, as one considers more sophisticated lattice gas fluid (like FHP-III [50]) or 3-D models [66]), the collision term requires a very large number of floating point operations at each lattice site and time step. Even on a massively parallel computer, in which every cell is computed simultaneously, this may not be acceptable.

The first solution to this problem is to consider the same approximation as we used with the Chapman–Enskog expansion when deriving the macroscopic behavior of the FHP fluid. The idea is to linearize the collision term around its local equilibrium solution. This approach has been proposed by Higuera and coworkers [83] and considerably reduces the complexity of the operations involved.

4.2. BGK models

Following the same idea, a further simplification can be considered [84]: the collision term need not be related to an existing cellular automata microdynamics, as long as

particle and momentum are conserved. In its simplest form, the lattice Boltzmann dynamics can be written as a relaxation equation [143, 25]

$$f_i(\vec{r} + \Delta_t \vec{v}_i, t + \Delta_t) - f_i(\vec{r}, t) = \Omega_i(f) = \frac{1}{\tau} \left(f_i^{(0)}(\vec{r}, t) - f_i(\vec{r}, t) \right), \quad (4.2)$$

where $f_i(\vec{r}, t)$ denotes the probability that, at time t , a particle is entering site \vec{r} along lattice direction i (note that here, we use the notation f_i instead of N_i). The quantity τ is a relaxation time, which is a free parameter of the model. It actually will determine the fluid viscosity.

Equivalently, Eq. (4.2) reads

$$f_i(\vec{r} + \Delta_t \vec{v}_i, t + \Delta_t) = \frac{1}{\tau} f_i^{(0)}(\vec{r}, t) + \left(1 - \frac{1}{\tau} \right) f_i(\vec{r}, t), \quad (4.3)$$

which is the appropriate form for a numerical implementation.

The local equilibrium solution $f_i^{(0)}$ is a function of the actual density $\rho = \sum f_i$ and velocity flow $\rho \vec{u} = \sum f_i \vec{v}_i$. Therefore, when implementing Eq. (4.3) on a computer, one first computes at each site, ρ and \vec{u} from the current values of the f_i 's and then one may compute $f_i^{(0)}(\rho, \vec{u})$. In general, $f^{(0)}$ is a non-linear function of ρ and \vec{u} and thus, Eq. (4.3) is non-linear in the f_i 's.

It is important to notice that $f^{(0)}$ is model dependent and can be adjusted so as to produce a given, expected, behavior. In particular, the lack of Galilean invariance that plagues cellular automata fluid can be cured, as well as the spurious velocity contribution appearing in expression (3.44) of the pressure term. In a more general context, $f_i^{(0)}$ could include other physical features, such as a local temperature [2, 147] and can be tuned to describe other physical situations, as shown in Sec. 8.

Equation (4.2) is referred to as the lattice BGK method [143] (BGK stands for Bhatnager, Gross and Krook [10] who first considered a collision term with a single relaxation time, in 1954). Equation (4.2) is studied by several authors [87, 144], due to its ability to deal with high Reynolds number flows. However, one difficulty of this approach are the numerical instabilities which may develop when large velocity gradients are present.

4.3. *Lattice Boltzmann fluids*

In this section we define the generic dynamics of LB fluid models (precisely BGK models) and derive the corresponding macroscopic behavior.

A common example of LB fluid is the so-called D2Q9 model (see Ref. 144) defined in two dimensions (D2) with nine variables, or quantities per sites (Q9). This lattice and its possible directions of motion are shown in Fig. 29. Note that a 9th direction $i = 0$ is defined to describe a population $f_0(\vec{r}, t)$ of particles at rest (i.e. having $\vec{v}_0 = 0$). The isotropy problems inherent to square lattices in 2-D are solved by weighting differently the eight possible directions of motion. Here we interpret these weights as masses m_i associated to the particles traveling

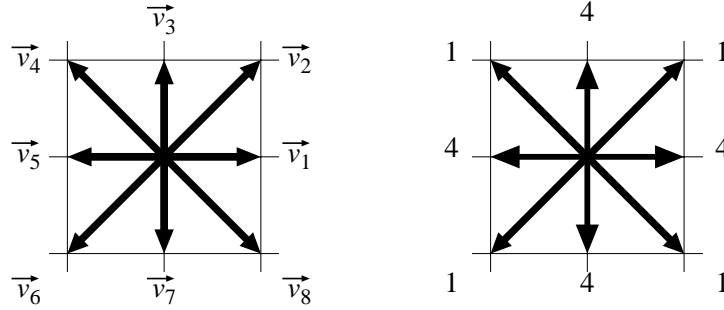


Fig. 29. The eight velocities in the D2Q9 lattice Boltzmann model of a two-dimensional fluid (on the left) and the mass associated to each of these directions (on the right).

along each direction. Figure 29 (right) gives the appropriate masses for the D2Q9 model.

In a general $DdQ(z+1)$ LB fluid, the macroscopic quantities, such as the local density ρ or the velocity flow \vec{u} are defined as usual as

$$\rho = \sum_{i=0}^z m_i f_i, \quad \rho \vec{u} = \sum_{i=0}^z m_i f_i \vec{v}_i, \quad (4.4)$$

where z is again the number of non-zero velocities in the model.

We set $v = \Delta_r / \Delta_t$ and assume that the lattice has the following properties

$$\sum_{i=1}^z m_i = C_0, \quad \sum_{i=1}^z m_i v_{i\alpha} v_{i\beta} = C_2 v^2 \delta_{\alpha\beta} \quad (4.5)$$

and

$$\sum_{i=1}^z m_i v_{i\alpha} v_{i\beta} v_{i\gamma} v_{i\delta} = C_4 v^4 (\delta_{\alpha\beta} \delta_{\gamma\delta} + \delta_{\alpha\gamma} \delta_{\beta\delta} + \delta_{\alpha\delta} \delta_{\beta\gamma}). \quad (4.6)$$

Note, also, that odd tensors are supposed to vanish. For the D2Q9 model, we have $m_i = 1$ for diagonal motions, $m_i = 4$ for horizontal and vertical motions and (see Ref. 33)

$$C_0 = 20, \quad C_2 = 12, \quad C_4 = 4.$$

For the D2Q7 (hexagonal lattice in two dimensions) one has $m_i = 1$ for all i and

$$C_0 = 6, \quad C_2 = 3, \quad C_4 = \frac{3}{4},$$

The next step is to define the local equilibrium distribution $f_i^{(0)}$ as a function of the macroscopic quantities ρ and \vec{u} . A natural choice is to adopt a similar expression as obtained for the FHP model, namely Eq. (3.37). Accordingly, we define

$$\begin{aligned} f_i^{(0)} &= a\rho + \frac{b}{v^2} \rho \vec{v}_i \cdot \vec{u} + \rho e \frac{u^2}{v^2} + \rho \frac{h}{v^4} v_{i\alpha} v_{i\beta} u_\alpha u_\beta \quad i \geq 1, \\ f_0^{(0)} &= a_0 \rho + \rho e_0 \frac{u^2}{v^2}, \end{aligned} \quad (4.7)$$

60 *B. Chopard, et al.*

where a , a_0 , b , e , e_0 and h are coefficients which will now be determined, first using mass and momentum conservation, and second by matching the form of the momentum tensor with the standard expression of hydrodynamics.

Mass and momentum conservation impose

$$\sum_{i=0}^z m_i \Omega_i = 0 \quad \text{and} \quad \sum_{i=0}^z m_i \vec{v}_i \Omega_i = 0.$$

This implies that

$$\sum_{i=0}^z m_i f_i^{(0)} = \rho \quad \text{and} \quad \sum_{i=0}^z m_i \vec{v}_i f_i^{(0)} = \rho \vec{u}, \quad (4.8)$$

because ρ and $\rho \vec{u}$ are defined through relations (4.4). Using relations (4.5) and (4.6), we obtain from (4.7)

$$\begin{aligned} \sum_{i=0}^z m_i f_i^{(0)} &= (m_0 a_0 + C_0 a) \rho + (m_0 e_0 + C_0 e + C_2 h) \rho \frac{u^2}{v^2}, \\ \sum_{i=0}^z m_i \vec{v}_i f_i^{(0)} &= C_2 b \rho \vec{u}. \end{aligned} \quad (4.9)$$

As in the case of a CA fluid (see Sec. 3) we assume here that the LB dynamics can be solved by a multiscale Chapman–Enskog expansion. Thus, we write

$$f_i = f_i^{(0)} + \epsilon f_i^{(1)} + \dots$$

and the zeroth order of the momentum tensor is

$$\begin{aligned} \Pi_{\alpha\beta}^{(0)} &= \sum_{i=0}^8 m_i v_{i\alpha} v_{i\beta} f_i^{(0)} \\ &= C_2 v^2 \left[a + \left(e + \frac{C_4 h}{C_2} \right) \frac{u^2}{v^2} \right] \rho \delta_{\alpha\beta} + 2C_4 h u_\alpha u_\beta. \end{aligned} \quad (4.10)$$

In a real fluid, when the dissipative terms are disregarded (Euler equation) one has the following expression for the momentum tensor

$$\Pi_{\alpha\beta}^{(0)} = c_s^2 \rho \delta_{\alpha\beta} + \rho u_\alpha u_\beta, \quad (4.11)$$

where c_s is the sound speed.

By comparing Eq. (4.8) with (4.9) and Eq. (4.11) with (4.10) we obtain the following conditions

$$a = \frac{1}{C_2} \frac{c_s^2}{v^2}, \quad m_0 a_0 = 1 - \frac{C_0}{C_2} \frac{c_s^2}{v^2}$$

and

$$b = \frac{1}{C_2}, \quad e = -\frac{1}{2C_2}, \quad m_0 e_0 = \frac{C_0}{2C_2} - \frac{C_2}{2C_4}, \quad h = \frac{1}{2C_4}.$$

Where the sound speed is considered as an adjustable parameter. With the above result, we can rewrite Eq. (4.7) as

$$\begin{aligned} f_i^{(0)} &= \rho \left[\frac{1}{C_2} \frac{c_s^2}{v^2} + \frac{1}{C_2} \frac{\vec{v}_i \cdot \vec{u}}{v^2} + \frac{1}{2C_4 v^4} \left(v_{i\alpha} v_{i\beta} - v^2 \frac{C_4}{C_2} \delta_{\alpha\beta} \right) u_\alpha u_\beta \right], \\ m_0 f_0^{(0)} &= \rho \left[1 - \frac{C_0}{C_2} \frac{c_s^2}{v^2} + \left(\frac{C_0}{2C_2} - \frac{C_2}{2C_4} \right) \frac{u^2}{v^2} \right]. \end{aligned} \quad (4.12)$$

4.4. The Navier–Stokes equation

In Eq. (3.34), we have obtained the following result

$$\partial_t \rho u_\alpha + \partial_\beta \left[\Pi_{\alpha\beta} + \frac{\Delta t}{2} \left(\epsilon \partial_{t_1} \Pi_{\alpha\beta}^{(0)} + \partial_\gamma S_{\alpha\beta\gamma}^{(0)} \right) \right] = 0, \quad (4.13)$$

where $t = t_1/\epsilon + t_2/\epsilon^2$ and $\vec{r} = \vec{r}_1/\epsilon$ take into account the different time scales of the problem (see Eqs. (3.13) and (3.16)).

The derivation of (4.13) only relies on the fact that $\sum m_i \Omega_i = 0$ and $\sum m_i \Omega_i \vec{v}_i = 0$ and, thus, this equation is still valid here.

We have already obtained $\Pi^{(0)}$ in the previous section. We still need to compute $S_{\alpha\beta\gamma}^{(0)}$ and $\Pi^{(1)}$. The quantity $f^{(1)}$ is defined by a similar equation as obtained in relation (3.18), namely

$$\frac{1}{\Delta t} \sum_{j=0}^z \left(\frac{\partial \Omega_i(f^{(0)})}{\partial f_j} \right) f_j^{(1)} = \partial_{t_1} f_i^{(0)} + \partial_{1\alpha} v_{i\alpha} f_i^{(0)}.$$

Since $\Omega_i = \frac{1}{\tau} \left(f_i^{(0)}(\vec{r}, t) - f_i(\vec{r}, t) \right)$, the above equation simply reads

$$\begin{aligned} -\frac{1}{\Delta t \tau} f_i^{(1)} &= \partial_{t_1} f_i^{(0)} + \partial_{1\alpha} v_{i\alpha} f_i^{(0)} \\ &= -\frac{\partial f_i^{(0)}}{\partial \rho} \operatorname{div}_1 \rho \vec{u} - \frac{\partial f_i^{(0)}}{\partial \rho u_\alpha} \partial_{1\beta} \Pi_{\alpha\beta}^{(0)} + \partial_{1\alpha} v_{i\alpha} f_i^{(0)} \end{aligned} \quad (4.14)$$

with $\operatorname{div}_1 = \sum_\alpha \partial_{1\alpha}$. We shall now compute $f_i^{(1)}$ to the first order in \vec{u} . We have

$$f_i^{(0)} = a\rho + \frac{b}{v^2} \rho v_{i\alpha} u_\alpha, \quad f_0^{(0)} = a_0 \rho$$

and

$$\Pi_{\alpha\beta}^{(0)} = c_s^2 \rho \delta_{\alpha\beta}. \quad (4.15)$$

Thus,

$$\frac{\partial f_i^{(0)}}{\partial \rho} = a, \quad \frac{\partial f_i^{(0)}}{\partial \rho u_\alpha} = \frac{b}{v^2} v_{i\alpha}, \quad \frac{\partial f_0^{(0)}}{\partial \rho} = a_0, \quad \frac{\partial f_0^{(0)}}{\partial \rho u_\alpha} = 0$$

and we obtain

$$f_i^{(1)} = -\Delta t \tau \frac{1}{C_2 v^2} (v_{i\gamma} v_{i\delta} - c_s^2 \delta_{\gamma\delta}) \partial_{1\gamma} \rho u_\delta \quad \text{and} \quad f_0^{(1)} = -\Delta t \tau a_0 \operatorname{div}_1 \rho \vec{u}.$$

62 *B. Chopard, et al.*

Using that $\epsilon \partial_{1\gamma} = \partial_\gamma$, the order $O(\epsilon)$ contribution to Π reads

$$\begin{aligned} \epsilon \Pi_{\alpha\beta}^{(1)} &= \epsilon \sum_{i=0}^z m_i f_i^{(1)} v_{i\alpha} v_{i\beta} \\ &= \Delta_t v^2 \tau \left[\left(\frac{c_s^2}{v^2} - \frac{C_4}{C_2} \right) \delta_{\alpha\beta} \operatorname{div} \rho \vec{u} - \frac{C_4}{C_2} (\partial_\beta \rho u_\alpha + \partial_\alpha \rho u_\beta) \right]. \end{aligned} \quad (4.16)$$

Thus

$$\partial_\beta \epsilon \Pi_{\alpha\beta}^{(1)} = -\Delta_t v^2 \tau \left[\left(2 \frac{C_4}{C_2} - \frac{c_s^2}{v^2} \right) \partial_\alpha \operatorname{div} \rho \vec{u} + \frac{C_4}{C_2} \partial_\beta^2 \rho u_\alpha \right]. \quad (4.17)$$

From this expression, we get two viscosity coefficients (shear and bulk viscosity), as usual in compressible fluids.

The final step is the calculation of the lattice viscosity. The first term in Eq. (4.13) giving a contribution to the lattice viscosity is $\partial_\beta (\Delta_t \epsilon / 2) \partial_{t_1} \Pi_{\alpha\beta}^{(0)}$. With $\Pi_{\alpha\beta}^{(0)} = c_s^2 \rho \delta_{\alpha\beta} + O(u^2)$, we have

$$\frac{\Delta_t \epsilon}{2} \partial_{t_1} \Pi_{\alpha\beta}^{(0)} = \Delta_t \frac{c_s^2}{2} \epsilon \partial_{t_1} \rho \delta_{\alpha\beta} = -\Delta_t \frac{c_s^2}{2} \delta_{\alpha\beta} \operatorname{div} \rho \vec{u},$$

where we have used that $\partial_{t_1} \rho + \operatorname{div}_1 \rho \vec{u} = 0$ (see Eq. (3.25)) and the definition of the length scale $\epsilon \operatorname{div}_1 = \operatorname{div}$. Therefore

$$\frac{\Delta_t \epsilon}{2} \partial_\beta \partial_{t_1} \Pi_{\alpha\beta}^{(0)} = -\Delta_t \frac{c_s^2}{2} \partial_\alpha \operatorname{div} \rho \vec{u}. \quad (4.18)$$

Similarly, we must compute the contribution due to $S_{\alpha\beta\gamma}^{(0)}$ in equation (4.13)

$$\begin{aligned} S_{\alpha\beta\gamma}^{(0)} &= \sum_{i=0}^z m_i v_{i\alpha} v_{i\beta} v_{i\gamma} f_i^{(0)} \\ &= v^2 \frac{C_4}{C_2} \rho (u_\gamma \delta_{\alpha\beta} + u_\beta \delta_{\alpha\gamma} + u_\alpha \delta_{\beta\gamma}). \end{aligned} \quad (4.19)$$

Consequently, we obtain the dissipative lattice contributions

$$\frac{\Delta_t}{2} \partial_\beta \left(\epsilon \partial_{t_1} \Pi_{\alpha\beta}^{(0)} + \partial_\gamma S_{\alpha\beta\gamma}^{(0)} \right) = \frac{\Delta_t v^2}{2} \left[\frac{C_4}{C_2} \nabla^2 (\rho u_\alpha) + \left(\frac{2C_4}{C_2} - \frac{c_s^2}{v^2} \right) \partial_\alpha \operatorname{div} \rho \vec{u} \right]. \quad (4.20)$$

Finally, after substitution of Eqs. (4.20), (4.17) and (4.15) into Eq. (4.13), we obtain

$$\begin{aligned} \partial_t \rho u_\alpha + \rho u_\beta \partial_\beta u_\alpha + u_\alpha \operatorname{div} \rho \vec{u} &= -c_s^2 \partial_\alpha \rho + \Delta_t v^2 \frac{C_4}{C_2} \left(\tau - \frac{1}{2} \right) \nabla^2 \rho u_\alpha \\ &\quad + \Delta_t v^2 \left(\tau - \frac{1}{2} \right) \left[2 \frac{C_4}{C_2} - \frac{c_s^2}{v^2} \right] \partial_\alpha \operatorname{div} \rho \vec{u}. \end{aligned} \quad (4.21)$$

In the case of an incompressible fluid (at low Mach number, for instance) one has $\operatorname{div} \rho \vec{u} = 0$ and one recovers the usual Navier–Stokes equation

$$\partial_t \vec{u} + (\vec{u} \cdot \nabla) \vec{u} = -\frac{1}{\rho} \nabla p + \nu_{\text{lb}} \nabla^2 \vec{u}, \quad (4.22)$$

where $p = c_s^2 \rho$ is the scalar pressure and ν_{lb} is the kinematic viscosity

$$\nu_{\text{lb}} = \Delta_t v^2 \frac{C_4}{C_2} \left(\tau - \frac{1}{2} \right). \quad (4.23)$$

As we see from this result, there are two free physical quantities in this model, c_s^2 and τ , and three parameters C_0 , C_2 and C_4 depending of the specific lattice chosen for the simulation.

Changing c_s within acceptable limits will modify the sound speed (or the temperature, since $p = c_s^2 \rho$). Clearly $c_s^2 < (C_2/C_0)v^2$ otherwise a_0 becomes negative.

Also, the relaxation time τ can be tuned to adjust the viscosity within some range. We can see that when τ is small, relaxation to $f^{(0)}$ is fast and viscosity small. This means that the collision between the particles are quite effective to restore the local equilibrium.

However, τ cannot be made arbitrarily small since $\tau < 1/2$ would imply a negative viscosity. Practically, more restrictions are expected, because the dissipation length scale should be much larger than the lattice spacing. The value $\tau = 1/2$ yields numerical instability and the smaller acceptable value depends on the velocity gradients.

Figure 30 illustrates the behavior of the LB fluid in a simulation of a flow past a plate leading to a von Karman street pattern.

4.5. Body force

In many applications it is desirable to include an external force in the dynamics of the density distribution f_i . This is an effective way to accelerate a fluid, as for instance to produce a channel flow, or to represent some gravity effects. This type

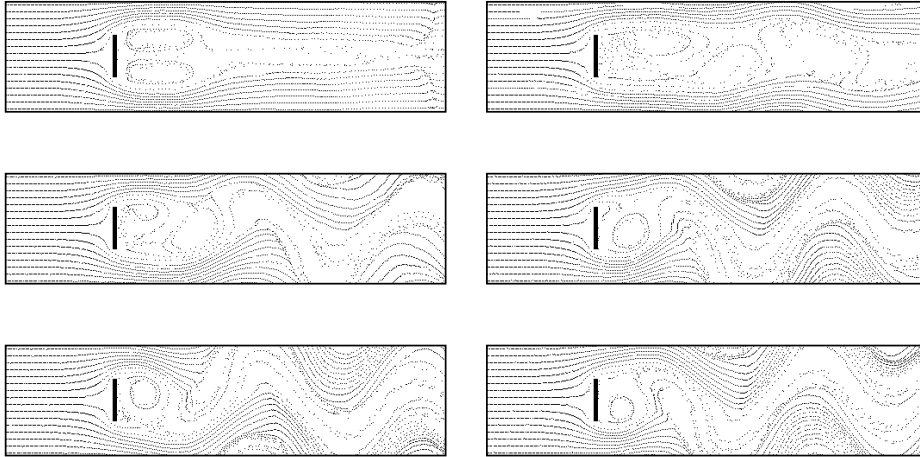


Fig. 30. Non-stationary flow past a plate obtained with the D2Q8 lattice Boltzmann model. System size is 512×128 , $\tau = 1$, and the entry speed is $u_\infty = 0.025$. From left to right and top to bottom, the figure shows the different stages of evolution.

64 *B. Chopard, et al.*

of force is termed body force because it acts at each site of the fluid, as a force per unit of volume.

The most common way to include a body force \vec{F} in the LB equation is to include an additive term

$$f_i(\vec{r} + \Delta_t \vec{v}_i, t + \Delta_t) = \frac{1}{\tau} f_i^{(0)}(\vec{r}, t) + \left(1 - \frac{1}{\tau}\right) f_i(\vec{r}, t) + \frac{\Delta_t}{v^2 C_2} \vec{v}_i \cdot \vec{F}. \quad (4.24)$$

The body force term is such that it preserves mass (since $\sum_i m_i \vec{v}_i = 0$) and adds a momentum contribution $\Delta_t \vec{F}$ after each iteration. Indeed, since $\sum_i m_i \vec{v}_i (f_i^{(0)} - f_i) = 0$ Eq. (4.24) gives

$$\begin{aligned} & \sum_i m_i v_{i\alpha} f_i(\vec{r} + \Delta_t \vec{v}_i, t + \Delta_t) - \sum_i m_i v_{i\alpha} f_i(\vec{r}, t) \\ &= + \frac{\Delta_t}{v^2 C_2} \sum_i m_i v_{i\alpha} v_{i\beta} F_\beta = \Delta_t F_\alpha. \end{aligned}$$

Note that other terms could be added to Eq. (4.24) to produce the same mass and momentum balance. For instance, an extra contribution

$$G_{i\alpha\beta} = G_{\alpha\beta} (v_{i\alpha} v_{i\beta} - a \delta_{\alpha\beta}), \quad G_{0\alpha\beta} = -b G_{\alpha\beta} \delta_{\alpha\beta},$$

where $G_{\alpha\beta}$ is any tensor quantity, has the property that $\sum_i m_i G_{i\alpha\beta} v_{i\gamma} = 0$ because it contains an odd number of \vec{v}_i factors. In addition,

$$\sum_i m_i G_{i\alpha\beta} = G_{\alpha\beta} (v^2 C_2 - a C_0 - b) \delta_{\alpha\beta}.$$

Thus, if the constant a and b are well chosen, $\sum_i m_i G_{i\alpha\beta} = 0$. For instance, a possible choice is

$$a = c_s^2 \quad \text{and} \quad b = v^2 C_2 \left[1 - \frac{c_s^2 C_0}{v^2 C_2} \right].$$

The continuity and Navier–Stokes equations for ρ and \vec{u} resulting from the inclusion of a body force can be obtained from the multiscale Chapman–Enskog formalism introduced above. The calculation shows that the effect of the body force introduced in Eq. (4.24) is not as simple as expected. The continuity equation reads

$$\partial_t \rho + \text{div} \rho \vec{u} = -\frac{\Delta_t}{2} \text{div} \vec{F}. \quad (4.25)$$

Thus, although mass is microscopically conserved, this equation indicates that $\rho \vec{u}$ is no longer the correct definition of mass current if the body force has a spatial dependence. The mass current could be better represented by $\rho \vec{u} + (\Delta_t/2) \vec{F}$ in order to remove the right hand side of Eq. (4.25).

Similarly, the Navier–Stokes equation has some unexpected contributions when the external force depends on time

$$\begin{aligned} & \partial_t \rho u_\alpha + \rho u_\beta \partial_\beta u_\alpha + u_\alpha \operatorname{div} \rho \vec{u} \\ &= -c_s^2 \partial_\alpha \rho + \nu_{\text{lb}} \nabla^2 \rho u_\alpha + \Delta_t v^2 \left(\tau - \frac{1}{2} \right) \left[2 \frac{C_4}{C_2} - \frac{c_s^2}{v^2} \right] \partial_\alpha \operatorname{div} \rho \vec{u} + F_\alpha - \frac{\Delta_t}{2} \partial_t F_\alpha. \end{aligned} \quad (4.26)$$

As a result, the spurious term $\partial_t F_\alpha$ is expected to produce artificial time lag effects (typically half a time step Δ_t for low frequencies).

We refer the reader to Ref. 78 for a more detailed discussion of the problem and ways to solve it.

Let us now mention a simple application of the body force. As discussed previously, the body force can be used to represent some gravity effects, or drive the flow. As an example we shall consider the case of a 2-D channel flow with a horizontal driving force along the x -axis and a vertical gravity force along the y -axis. Two horizontal walls prevent the fluid from moving vertically. Horizontally, we assume periodic boundary conditions. Thus, we choose

$$\vec{F} = \rho \vec{g},$$

where g_y is the gravity field and g_x the driving force.

In the stationary regime, $\partial_t \vec{u} = \partial_t \rho = 0$ and the symmetry of the problem imposes that

$$\rho = \rho(y), \quad u_x = u_x(y), \quad u_y = 0.$$

With these assumptions the Navier–Stokes equation reduces to

$$\begin{aligned} 0 &= \nu \partial_y^2 [\rho u_x] + \rho g_x, \\ 0 &= -c_s^2 \partial_y \rho + \rho g_y. \end{aligned}$$

The boundary conditions are

$$u_x(0) = u_x(L) = 0, \quad \int_0^L \rho(y) dy = L \rho_0, \quad (4.27)$$

where L is the channel width and ρ_0 the average density.

The solutions for the density is the barometric expression

$$\rho(y) = \rho_0 \frac{L g_y}{c_s^2} \frac{\exp \left[-\frac{g_y}{c_s^2} (L - y) \right]}{1 - \exp \left[-\frac{g_y}{c_s^2} L \right]} \quad (4.28)$$

and the velocity field is obtained as

$$u_x(y) = \frac{g_x}{g_y} \frac{c_s^2}{\nu} \frac{c_s^2}{g_y} \left[\frac{\rho(0)}{\rho(y)} - 1 - \frac{\rho(0) - \rho(L)}{\rho(y)} \frac{y}{L} \right]. \quad (4.29)$$

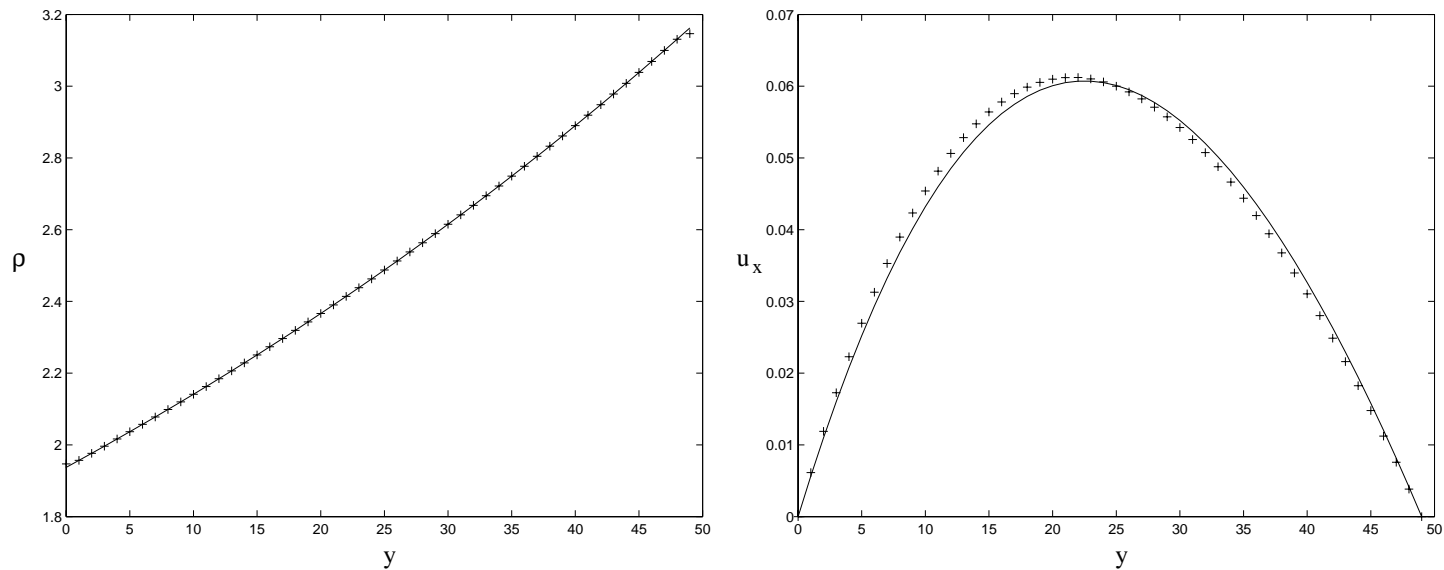


Fig. 31. Channel flow with gravity and driving forces proportional to the local fluid density. The average density is $\rho_0 = 2.5$, $g_x/c_s^2 = 0.0001$ and $g_y/c_s^2 = 0.01$. The system size is 100×50 , the relaxation time is $\tau = 1$ and the system is observed after 30 000 iterations. Simulation results are shown with dots and the analytical solution is the solid line. The left panel shows the density variation along the y -axis and the right one, the x -component of the velocity. It is interesting to note that in this case, the velocity profile is no longer a parabola, although it looks like a parabola.

Figure 31 shows the comparison of the analytical solutions (4.29) with the result of a D2Q9 simulation of Eq. (4.24). Note that in the simulation we used the no-slip velocity boundary condition mentioned in Sec. 4.6. We see that there is a perfect agreement for the density but a small systematic deviation for the velocity. This aspect is not fully understood yet but is probably due to an observed non-zero component u_y , related to the inconsistency of the definition of \vec{u} when there is a body force.

It is also possible to have a body force \vec{F} which does not depend on the local fluid density ρ . It is probably less physical but can be convenient. Indeed, when modeling an incompressible fluid like water, it is undesirable to have a pressure field $p(y) = c_s^2 \rho(y)$ which depends exponentially with the vertical location. A constant body force produces a linear pressure increase along the vertical direction, which corresponds to the usual hydrostatic situation.

With $\vec{F} = (F_x, F_y)$ and the same geometry as before, the Navier–Stokes equation becomes

$$0 = \nu \partial_y^2 [\rho(y) u_x(y)] + F_x, \quad 0 = -c_s^2 \partial_y \rho(y) + F_y.$$

With the above boundary conditions (4.27), the solutions are

$$\rho(y) = \rho_0 + \frac{F_y}{c_s^2} \frac{L}{2} + \frac{F_y}{c_s^2} (y - L)$$

and

$$u_x(y) = \frac{F_x}{2\nu\rho(y)} [y(L - y)]. \quad (4.30)$$

This situation is illustrated in Fig. 32. A perfect agreement is found between theory and simulation for the density solution whereas, again, a slight bias can be seen for the velocity profile.

Finally, note that a constant body force may easily produce negative populations. Indeed, the term

$$\vec{v}_i \cdot \vec{F} \neq 0$$

even if the f_i themselves are null. Thus, positive and negative populations are created which sum up to zero but can nevertheless propagate in the fluid. This may produce numerical instabilities. Also, in the case of a two-fluid system it is quite undesirable to have such a body force acting on the lattice sites that are unoccupied by the fluid subject to this force.

When the fluid is incompressible, the density is constant and including or not the density in the body force does not make a big difference: the effect is just to renormalize the amplitude of the force. Ultimately, the choice of $\vec{F} = (F_x, F_y)$ or $\vec{F} = \rho(g_x, g_y)$ depends on the physics of the problem.

It turns out that accelerating a fluid with a body force usually require a lot of iterations before reaching a steady state. Imposing the velocity at some location is usually numerically more efficient, but can also produce undesirable effects [57].

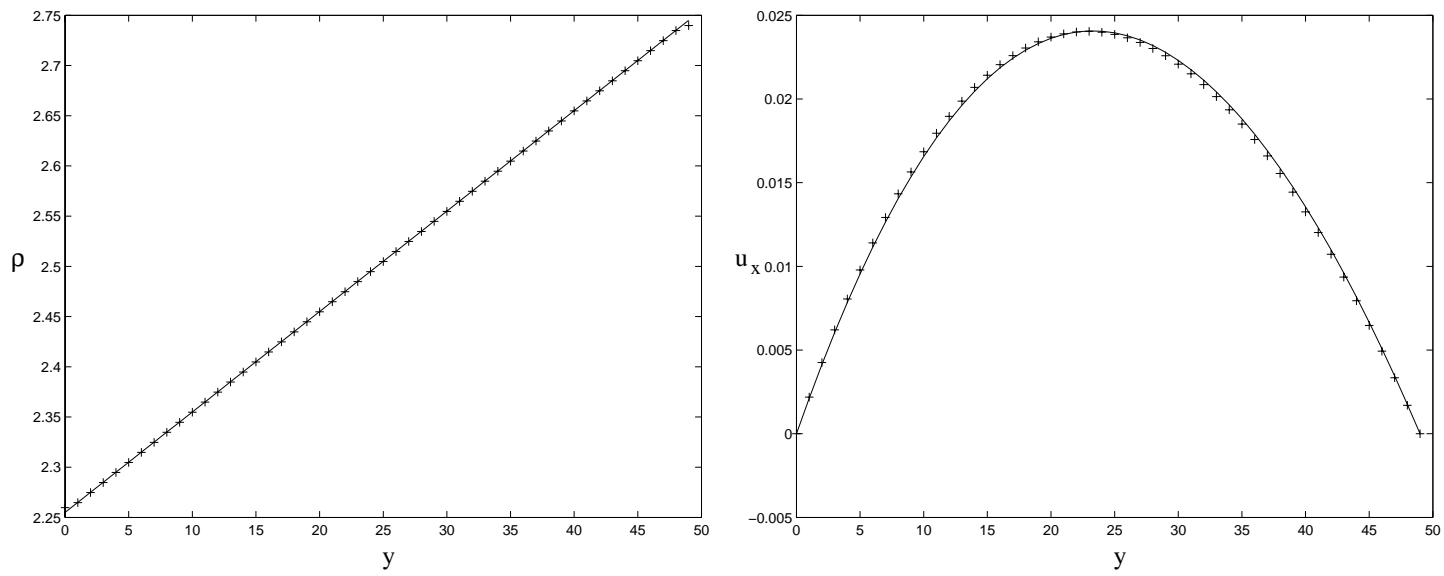


Fig. 32. Channel flow with gravity and driving forces independent of the local fluid density. The average density is $\rho_0 = 2.5$, $F_x/c_s^2 = 0.0001$ and $F_y/c_s^2 = 0.01$. The system size is 100×50 , the relaxation time is $\tau = 1$ and the systems observed after 30 000 iterations. Simulation results are shown with dots and the analytical solution is the solid line. The left panel shows the density variation along the y -axis and the right one, the x -component of the velocity.

The time to reach a stationary regime can be estimated from Eq. (4.26) which, in a channel flow geometry, with constant body force and an incompressible regime reads

$$\partial_t u_x = \nu \nabla^2 u_x + \frac{F_x}{\rho}. \tag{4.31}$$

By writing $u_x(y, t) = (F_x/(2\nu\rho))[y(L - y)] + \psi(y, t)$, we obtain that $\psi(y, t)$ obeys

$$\partial_t \psi = \nu \nabla^2 \psi.$$

In a Fourier representation, $\nabla^2 \psi$ behaves as $-k^2 \psi_k$ where k is the wave number. Small k modes are the slowest to relax and we may assume that the most relevant value of k will be $2\pi/L$, with L the channel width. The solution of Eq. (4.31) is

$$\psi_{\frac{2\pi}{L}}(t) = \psi_{\frac{2\pi}{L}}(0) \exp\left[-\frac{4\pi^2}{L^2} \nu t\right].$$

Therefore, we expect that the asymptotic regime will settle in time T proportional to L^2 . This is confirmed by the numerical simulations shown in Fig. 33. In this figure we plot T versus the Reynolds number $Re = u_\infty L/\nu$. From Eq. (4.30) $u_\infty = u_x(L/2) = (L^2 F_x)/(8\nu\rho)$ and, thus $Re = (L^3 F_x)/(8\nu^2\rho)$. In the simulation, the Reynolds number has been increased by increasing L and reducing the force as $F_x \propto 1/L^2$ to keep the same Mach number for all system sizes L . Therefore, $Re \propto L$ and the relation between T and Re should be a parabola. Note that Ref. 95, proposes a way to speed up this convergence process.

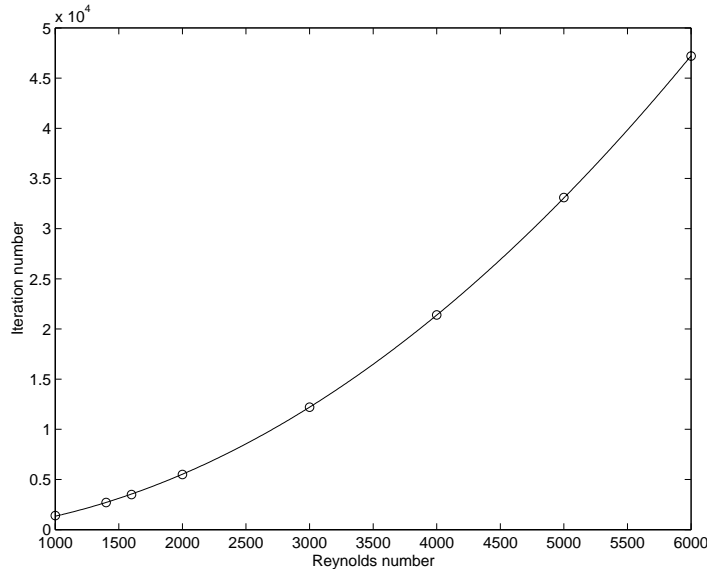


Fig. 33. Time T needed to reach a stationary regime when a body force is applied to a channel flow situation. The dependence $T \propto L^2$ is seen from the fact that $Re \propto L$.

4.6. *Boundary conditions*

Boundary conditions are an important issue in LB simulations. We refer the reader to Refs. 57, 63, 122, 165 for more information. Here we only give some essential ideas.

When the system cannot be made periodic, it is necessary to limit the computational domain with walls. There are several ways to choose the dynamics of the f_i at the wall and, thus, specify the boundary conditions. Roughly speaking we can divide the LB boundary conditions into three categories:

Bounce back rules: This is the simplest way to deal with a wall and does not require any knowledge of its shape. It is enough to know that a given site is a wall. When particles reach such a solid site, they just bounce back from where they came. This is always a direction which is valid since particles have just arrived from that direction. Bounce back can be implemented as **full-way** bounce back or **half-way** bounce back.

In the first case, one allows the f_i to reach the wall site. Then, during the collision phase, the f_i is moved to $f_{i'}$, where i' is the direction opposite to i . During the propagation phase, the particles are thus sent back to their originating site. The round trip takes two iterations.

In the half-way case, the directions i in which a wall is present are marked. The particles that, after the collision, point in such a wall direction i are not propagated but copied into the opposite direction for future use at the next collision step. Therefore, in the half-way bounce-back, the wall site are not needed in the computational domain and particles return to their originating site after one time step only.

The half-way bounce back seems better than the full-way bounce-back. In some situation it produces a second order accurate solution, whereas the full-way bounce-back is only found to be first order accurate in term of the lattice spacing. However, this observation depends on the geometry of the flow and cannot be generalized [57].

With the full way bounce back, the collision is modified but the propagation remains identical for all lattice sites. On the contrary, in the half-way bounce back, the collision is performed as prescribed by the collision rule but the propagation is changed. This may also explain why the two methods do not perform identically.

Note that the bounce back family clearly conserves mass as it reinjects into the system the particles hitting a wall. The fact that the particles return from where they came is an attempt to produce a zero velocity at the wall. This is not always very effective and a so-called slip velocity (which depends on the viscosity) is often observed along a wall [79].

Collision-at-wall: We term the second class of boundary conditions “collision-at-wall”. Their goal is to suppress the slip velocity mentioned above. The wall is part of the simulation domain and a regular collision is applied on wall sites. However, at a wall site, there are valid and non-valid entering directions and valid and non-valid

exiting directions. The non-valid out-directions are those which do not point toward a fluid site, whereas the non-valid in-directions are those coming from the outside of the system.

In the “collision-at-wall” rules, the non-valid out-fields f_i produced after the collision phase are forgotten during the propagation phase. However, in order to perform the collision step, the non-valid in-fields f_k must be defined properly. The indices k of these fields do depend on the local geometry of the wall and are different whether the wall is flat, or a convex/concave corner.

Different authors have proposed different ways to assign a value to these non-valid incoming f_k 's. The problem simply amounts to solving a set of linear equations for these unknown fields. Usually, the equations reflect the desired velocity at the wall, and sometimes mass conservation [57]. There are usually more unknown than equations, which requires some appropriate way to limit the freedom.

A simple method is the so-called modified bounce-back rule [79] where the missing f_k 's are set to $f_{k'}$. This works rather well for a flat boundary but not for some corner configurations. A more general technique is the so-called *mass conserving boundary condition* proposed in Ref. 57, where the missing density distributions are computed so as to ensure no-slip at the boundary and mass conservation (i.e. no creation or destruction of mass at the wall). This technique is second order accurate in a Poiseuille flow, as shown in Fig. 34 and offer a way to impose the stress tensor at the wall.

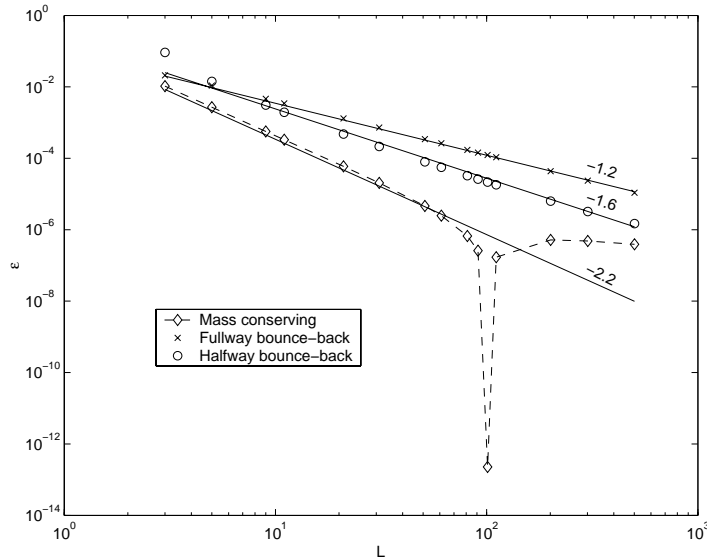


Fig. 34. Error e between the analytical, parabolic profile and the simulation data in a simple Poiseuille flow as the grid refinement (i.e. the number of grid points L) is increased. The values indicated over the lines are the exponents α found when assuming $e \propto L^{-\alpha}$. Thus the value of α gives the accuracy of the scheme. The drop at $L = 100$ for the mass-conserving scheme corresponds here to a relaxation time $\tau = 1$, for which extra accuracy is obtained.

Inamuro's approach is well known [89] and gives machine accuracy in a Poiseuille flow. It assumes that the unknown fields are expressed with a local equilibrium expression with velocity \vec{u}' and density ρ' that needs to be determined. This approach reduces the number of unknowns in a clever way. Note however that in Inamuro's scheme the LB collision is not performed at the wall. This method can be generalized to 2-D flat planes but is difficult to apply with non-flat walls [57].

To illustrate the accuracy of the above boundary conditions, Fig. 34 shows the distance between the analytical profile and the simulation data in a simple Poiseuille flow, as the lattice spacing is reduced but both Re and Mach numbers are kept constant (note that many authors, when studying LB accuracy, change Re or Mach numbers as they change the number of grid points).

Interpolation scheme: A third way to implement boundary conditions is to use an interpolation method [63, 122]. This has the advantage of being applicable to off-lattice walls and has an expected second order accuracy if the interpolation scheme is good enough. However, its numerical implementation is more tedious than the two previous approaches. The idea is the following. When the wall is off-lattice, some lattice links are cut by the wall. Thus, no f_i will ever come out of the wall along these links. These missing fields can be reconstructed by interpolation. A solution is to use the field that bounced back on the wall along that same link and which is at some well defined off-lattice location. Another solution is to compute the missing f_i from the corresponding values measured at the nearest sites by a linear or quadratic interpolation.

4.7. A short summary of LB models

This section summarizes the main finding of the above discussion, in order to highlight the important steps necessary to implement on a computer a LB fluid simulation.

(i) The system is described in terms of $z+1$ quantities $f_i(\vec{r}, t)$ giving the probability of presence of a particle entering lattice site \vec{r} with velocity \vec{v}_i , at time t . The field f_0 corresponds to a population of rest particles, with $\vec{v}_0 = 0$. The other possible velocities \vec{v}_i depend on the lattice under consideration. Usually, one has slow and fast velocities. The former ones have modulus $v = \Delta_r/\Delta_t$ where Δ_r is the lattice spacing and Δ_t the time step. The modulus of fast velocities are lattice-dependent.

The physical quantities are the density ρ and velocity field \vec{u} defined as

$$\rho = \sum_{i=0}^z m_i f_i, \quad \rho \vec{u} = \sum_{i=1}^z m_i f_i \vec{v}_i,$$

where m_0 can be set to 1 without loss of generality, and the other m_i are chosen so as to ensure the isotropy of the fourth order tensor $\sum_{i=1}^z m_i v_{i\alpha} v_{i\beta} v_{i\gamma} v_{i\delta}$. Usually, the value of m_i depends on whether \vec{v}_i is a fast or slow velocity.

(ii) For lattice sites not corresponding to a boundary of the system, the dynamics is given by Eq. (4.3)

$$f_i(\vec{r} + \Delta_t \vec{v}_i, t + \Delta_t) = \frac{1}{\tau} f_i^{(0)}(\vec{r}, t) + \left(1 - \frac{1}{\tau}\right) f_i(\vec{r}, t), \quad (4.32)$$

For boundary sites, a no-slip condition is enforced by bouncing back the incoming f_i , or by applying a more sophisticated boundary condition, as discussed in Sec. 4.6.

The local equilibrium distribution is given by Eq. (4.12). From a numerical point of view, it make sense to compute directly $m_i f_i$ and $m_i f_i^{(0)}$. Thus

$$m_i f_i^{(0)} = \rho \left(\frac{m_i c_s^2}{C_2 v^2} \right) \left[1 + \frac{\vec{v}_i \cdot \vec{u}}{c_s^2} + \frac{C_2}{2C_4 v^2 c_s^2} \left(v_{i\alpha} v_{i\beta} - v^2 \frac{C_4}{C_2} \delta_{\alpha\beta} \right) u_\alpha u_\beta \right],$$

$$m_0 f_0^{(0)} = \rho \left[\left(1 - \frac{C_0 c_s^2}{C_2 v^2} \right) - \frac{C_2}{2C_4} \left(1 - \frac{C_0 C_4}{C_2 C_2} \right) \frac{u^2}{v^2} \right],$$

where ρ and \vec{u} are computed from the current values of f_i , as explained in step 1.

Traditionally, the coefficients entering the above relations are termed t_i , that is

$$t_i = \left(\frac{m_i c_s^2}{C_2 v^2} \right) \quad \text{for } i \neq 0$$

and

$$t_0 = \left(1 - \frac{C_0 c_s^2}{C_2 v^2} \right).$$

Choosing $c_s^2 = v^2 C_4 / C_2$ makes the t_i very appropriate quantities to express the local equilibrium distributions.

When a body force is added, and one works directly $m_i f_i$, the term $\frac{\Delta_t}{C_2 v^2} \vec{F} \cdot \vec{v}_i$ of Eq. (4.24) gets multiplied by m_i and become a contribution

$$\frac{\Delta_t t_i}{c_s^2} \vec{F} \cdot \vec{v}_i.$$

(iii) The coefficients C_0 , C_2 and C_4 are defined in Eqs. (4.5) and (4.6), i.e.

$$\sum_{i=1}^z m_i = C_0, \quad \sum_{i=1}^z m_i v_{i\alpha} v_{i\beta} = C_2 v^2 \delta_{\alpha\beta}$$

and

$$\sum_{i=1}^z m_i v_{i\alpha} v_{i\beta} v_{i\gamma} v_{i\delta} = C_4 v^4 (\delta_{\alpha\beta} \delta_{\gamma\delta} + \delta_{\alpha\gamma} \delta_{\beta\delta} + \delta_{\alpha\delta} \delta_{\beta\gamma}).$$

These quantities are lattice dependent and are given in Table 1 for some standard lattices. Note that there is some arbitrariness in the choice of the m_i . The important point is to keep the correct ratio between the slow and fast masses. Then, if all m_i , $m_i \geq 1$ are multiplied by the same factor, then C_0 , C_2 and C_4 are modified proportionally and it is easy to check that $m_0 f_0^{(0)}$ and $m_i f_i^{(0)}$ are invariant under such a scaling of mass.

74 *B. Chopard, et al.*

Table 1. The geometrical coefficients necessary to compute the local equilibrium distribution in a LB simulation.

Model	Slow velocities	Fast velocities	C_0	C_2	C_4	Geometry
D1Q3	$ v_i = v, m_i = 1$		2	2	2/3	linear lattice
D2Q9	$ v_i = v, m_i = 4$	$ v_i = \sqrt{2}v, m_i = 1$	20	12	4	square lattice
D2Q7	$ v_i = v, m_i = 1$		6	3	3/4	hex lattice
D3Q15	$ v_i = v, m_i = 1$	$ v_i = \sqrt{3}v, m_i = 1/8$	7	3	1	cubic lattice
D3Q19	$ v_i = v, m_i = 2$	$ v_i = \sqrt{2}v, m_i = 1$	24	12	4	cubic lattice

The coefficients τ determines the fluid viscosity as:

$$\nu_{\text{lb}} = \Delta_t v^2 \frac{C_4}{C_2} \left(\tau - \frac{1}{2} \right)$$

and c_s can be tuned to select the sound speed. The maximal value is limited by

$$c_s^2 < (C_2/C_0)v^2.$$

A commonly chosen value is $c_s^2 = v^2(C_4/C_2)$.

Remember that numerical instabilities may develop in LB fluid models (see Sec. 4.8).

(iv) Up to order $O(u^2)$, the above numerical scheme solves the continuity equation

$$\partial_t \rho + \text{div } \rho \vec{u} = 0$$

and Navier–Stokes equation

$$\begin{aligned} & \partial_t \rho u_\alpha + \rho u_\beta \partial_\beta u_\alpha + u_\alpha \text{div } \rho \vec{u} \\ & = -c_s^2 \partial_\alpha \rho + \nu_{\text{lb}} \nabla^2 \rho u_\alpha + \Delta_t v^2 \left(\tau - \frac{1}{2} \right) \left[2 \frac{C_4}{C_2} - \frac{c_s^2}{v^2} \right] \partial_\alpha \text{div } \rho \vec{u}. \end{aligned} \quad (4.33)$$

This equation simplifies when $(u/c_s) \ll 1$ since, at low Mach number one may assume that $\text{div } \rho \vec{u} = 0$.

(v) In the formulation we gave of the LB formalism, space and time units are taken into account in the lattice spacing Δ_r and time step Δ_t . These quantities can in principle take any values, but their unit (meter, centimeter, second, ...) should be specified in order to make the connection with a real situation. In the simulation, one usually takes $\Delta_r = 1$, $\Delta_t = 1$, and the velocity field is then given in lattice units.

The case of the density ρ requires some explanation. In the formalism, $m_i f_i$ is a dimensionless number and the quantity $\rho = \sum_i m_i f_i$ has not the meaning of a mass per unit of volume. However, it should be noticed that the actual values of the f_i 's can be freely multiplied by any positive constant $\hat{\rho}$ having the usual units of mass over volume. Indeed, with $f_i \rightarrow \hat{\rho} f_i$, one has $\rho \rightarrow \hat{\rho} \rho$ and $f_i^{(0)} \rightarrow \hat{\rho} f_i^{(0)}$.

Therefore, this scaling does not affect the dynamics by more than a global scaling $\hat{\rho}$ and this freedom may be used to renormalize the density ρ of the simulation to any desired physical density.

4.8. Subgrid models

The LB fluid model has been extensively validated in the literature [12, 27, 51, 165] and is known to reproduce correctly the time-dependent Navier–Stokes equation. An important class of applications in hydrodynamics is high Reynolds number flows. A simple way to reach high Reynolds numbers is to reduce the viscosity by making τ close to $1/2$. Unfortunately, numerical instabilities may develop in this case, due to velocity gradients. To alleviate this problem, one can have recourse to the so-called Smagorinsky subgrid model. This is a standard approach in computational fluid dynamics and was first proposed for LBGK models by Hou *et al.* [87]. One assumes that a turbulent viscosity (ν_t) results from the unresolved scales, that is the scales below the lattice spacing Δ_r . These scales are thus filtered. The main idea is to increase locally the relaxation time τ by defining a space and time variable relaxation time τ_{tot} .

Then the total viscosity is split as

$$\nu_{\text{tot}} = \nu + \nu_t,$$

where ν is the original viscosity given by Eq. (4.23) with the original relaxation time τ . The new contribution ν_t is the so-called turbulent viscosity resulting from the filtered scales. In the Smagorinsky model [162], it is expressed as

$$\nu_t = (C_{\text{smago}}\Delta)^2 |S|, \quad (4.34)$$

where Δ is the filter size, whose magnitude usually corresponds to the grid spacing and $|S| = \sqrt{2S_{\alpha\beta}S_{\alpha\beta}}$ is the magnitude of the strain-rate tensor $S_{\alpha\beta} = 1/2(\partial_\beta u_\alpha + \partial_\alpha u_\beta)$. Thus, the larger the $|S|$ the larger the turbulent viscosity, so that the total viscosity is more important in regions close to obstacles.

In the LB scheme, the quantity $S_{\alpha\beta}$ can be computed locally, without taking extra derivatives, by only considering the non-equilibrium momentum tensor, as can be seen from Eq. (4.16).

$$S_{\alpha\beta} = -\frac{1}{2\rho\Delta_t\tau_{\text{tot}}}\frac{C_2}{C_4}\Pi_{\alpha\beta}^{(1)} = -\frac{1}{2\rho\Delta_t\tau_{\text{tot}}}\frac{C_2}{C_4}\sum_i m_i v_{i\alpha} v_{i\beta} (f_i - f_i^{(0)}). \quad (4.35)$$

Thus, from Eq. (4.34) and (4.35), the turbulent viscosity can be expressed as

$$\nu_t = \frac{1}{\tau_{\text{tot}}\sqrt{2\rho}\Delta_t}\frac{C_2}{C_4}(C_{\text{smago}}\Delta)^2\sqrt{Q^2}, \quad (4.36)$$

where $Q^2 = \Pi_{\alpha\beta}^{(1)}\Pi_{\alpha\beta}^{(1)}$. From Eq. (4.23), one has

$$\tau_{\text{tot}} = \frac{\Delta_t}{\Delta_r^2}\frac{C_2}{C_4}(\nu + \nu_t) + \frac{1}{2}. \quad (4.37)$$

76 *B. Chopard, et al.*

Considering that also

$$\frac{\Delta_t}{\Delta_r^2} \frac{C_2}{C_4} \nu + \frac{1}{2} = \tau$$

and replacing Eq. (4.36) into Eq. (4.37), one can solve the resulting second order equation and then express the local relaxation time as

$$\tau_{\text{tot}} = \frac{1}{2} \left(\sqrt{\tau^2 + \frac{1}{\Delta_r^2} (C_{\text{smago}} \Delta)^2 \left(\frac{C_2}{C_4} \right)^2 \frac{\sqrt{8Q^2}}{\rho}} + \tau \right). \quad (4.38)$$

The quantity C_{smago} (typically smaller than 0.5) tunes the effect of the subgrid model and should be adjusted empirically depending on the desired flow pattern.

The problem of adjusting correctly C_{smago} remains open. In order to model the boundary layer near a wall, one may expect that the value of C_{smago} is zero at the boundary of an obstacle and then increases to reach its bulk value as one gets away from the wall. No obvious theory describes how this variation should be and the simulation we performed did not show a real change on the main features of the flow when C_{smago} varies. Therefore, we assume that the simplified procedure of having a constant non-zero is enough in the present case.

As an illustration, we present in Fig. 35 the velocity pattern we obtain within this framework in the case of the flow around a pipeline sitting on a flat surface.

The flow we consider is turbulent ($\text{Re} = 7000$) and for this reason, we plot the stationary average streamlines and average horizontal velocity profile. This simulation compares well with the experiment by Jensen [93]. In addition, this flow is generic (with respect of the size of the main eddies and reattachment points) of the situations considered in laboratory experiments when studying the scour formation process [21, 102].

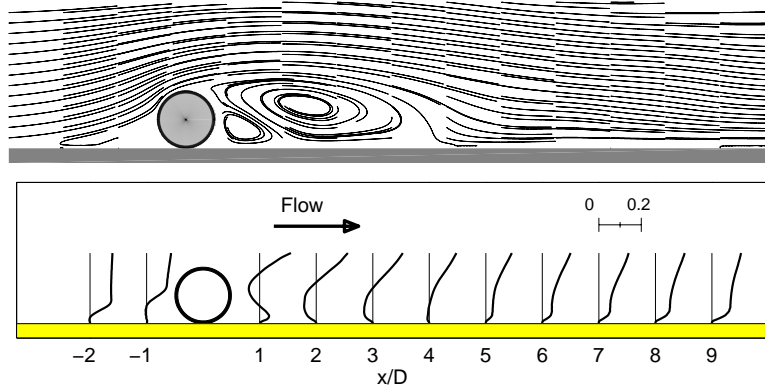


Fig. 35. Average flow pattern around a pipe in a turbulent regime, as obtained with the LB method. The Reynolds number is $\text{Re} = 7000$, obtained with $\tau = 0.5023$, $(C_{\text{smago}} \Delta)^2 = 0.4 \Delta_r^2$. The entry speed is $u_{\text{entry}} = 0.1 \Delta_r / \Delta_t$ and the cylinder diameter $D = 20 \Delta_r$. The upper panel shows the streamlines and the lower one the horizontal velocity profile at several locations. Distances are given in pipe diameters and velocities in lattice units.

4.9. Pattern formation in particles erosion and transport problems

The dynamics of solid particles erosion, transport and deposition due to the action of a streaming fluid plays a crucial role in sand dune formation, sedimentation problems and snow transport. This field remains rather empirical compared to other domains of science and experts do not all agree on the mechanisms involved in these processes. The CA and LB approach give a new and promising way to address these difficult problems.

In this section we explain the most important features of our model. We consider a mixed LB and CA approach (see for instance Refs. 43, 57, 58, 59, 116, 117, 118 for a general description of the method).

The fluid-particle system is described in terms of a mesoscopic dynamics: a LB fluid, as described above, plus sediment particles moving on the same regular lattice, synchronously at discrete time steps. An interaction is defined among the particles simultaneously present at the same lattice site. The granular material moves under the combined effect of the local fluid velocity and gravity.

When reaching the ground, the solid particles pile up and topple if necessary, changing in this way the boundary conditions for the fluid. The fluid particles bounce back on the deposited granular material. At the top of the deposition layer, erosion takes place and, if the fluid flows fast enough, it can pick up solid particles and transport them further away.

4.9.1. The sediment model

Apart from the fluid component, which we take here exactly as the LB model described in Sec. 4, sediments (typically snow or sand particles) are the new ingredient of the model. They are represented by an integer $n(\vec{r}, t) \geq 0$ indicating how many solid particles are present at site \vec{r} and time t . Sediments move on the same lattice as the fluid particles and interact with them. Since $n(\vec{r}, t)$ can take any positive value, we term our model a multiparticle CA [33].

It is important to remember that in our mesoscopic approach, we do not try to represent a specific granular material. We rather want to capture the generic features of the erosion-deposition process.

Transport Rule: After each time step, the particles jump to a nearest-neighbor site, under the action of the local fluid flow and gravity force. Gravity is taken into account by imposing a falling speed \vec{u}_{fall} on the particles. Therefore, our suspensions are passive particles since their presence does not modify the flow field, except when they form a solid deposit, i.e. a boundary.

If the local fluid velocity at site \vec{r} is $\vec{u}(\vec{r}, t)$, the particles located at that site will move to site $\vec{r} + \Delta_s(\vec{u} + \vec{u}_{fall})$, where Δ_s is the time unit associated with the motion of the granular particles. Unfortunately, this new location is usually not a lattice site. The solution to this problem is then to consider a stochastic motion [43, 116]: each of the $n(\vec{r}, t)$ particles jumps to a neighboring site $\vec{r} + \Delta_t \vec{v}_i$ with a probability

78 *B. Chopard, et al.*

p_i proportional to the projection of $\Delta_s(\vec{u} + \vec{u}_{fall})$ on the lattice direction $\Delta_t \vec{v}_i$. The quantity Δ_s is adjusted so as to maximize the probability of motion, while ensuring that the jumps are always smaller than a lattice constant.

Deposition Rule: Under the combined effect of motion and gravity, suspended particles will eventually land on a solid site (e.g. the bottom of the system or the top of the deposition layer). Motion is no longer possible and particles start piling up. In our model, up to N_{thres} particles can accumulate on a given site (N_{thres} gives a way to specify the spatial scale of the granular particles with respect to the fluid system). When this limit is reached, the site solidifies and new incoming particles pile up on the site directly above. These solid sites form new obstacles on which the fluid particles bounce back from where they came. Thus, this solidification process implies a dynamically changing boundary condition for the fluid.

Note that the rest particles are no longer subject to the suspension transport rule. Only the erosion mechanism discussed below can move them away.

Toppling rule: As sediment particles do not have infinite cohesion, we introduce a toppling rule. When a lattice site contains an excess of δN deposited particles with respect to its left or right neighbor (in 2D), toppling occurs. During this process, all unstable sites send a portion (c_t) of their grains in excess to the less occupied neighbors, see Fig. 36. With this rule, the stable configuration may not be reached in one time step. Notice that the toppling and transport processes may take place at different time scales.

The quantities δN and N_{thres} give a simple way to adjust the angle of repose of a pile. In the stable state, the model tolerates a maximum difference of δN particles between two adjacent sites. Two solidified sites are at least horizontally separated by k sites where $k = \lceil N_{thres}/\delta N \rceil$. Hence, the angle of repose α_{rep} satisfies $\tan \alpha_{rep} = 1/k$, as shown in Fig. 37.

Erosion: Finally, the erosion process is implemented as follows: with probability $p_{erosion}$ each particle belonging to the upper N_{thres} particles of the deposition layer (either a solid site or the rest particles that have accumulated directly above) is ejected vertically so as to reach the site just above it.

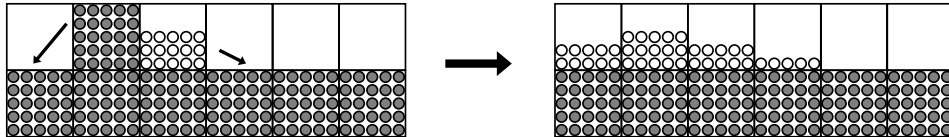


Fig. 36. Illustration of the toppling rule with $\delta N = 5$ and $N_{thres} = 20$. Gray particles indicate a solid site.

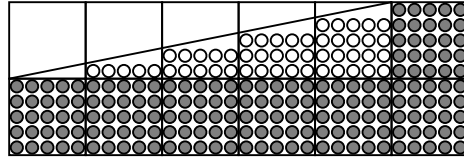


Fig. 37. The angle of repose can be adjusted from the relation $\tan \alpha = (\delta N / N_{\text{thres}})$. Here, $\delta N = 5$ and $N_{\text{thres}} = 20$.

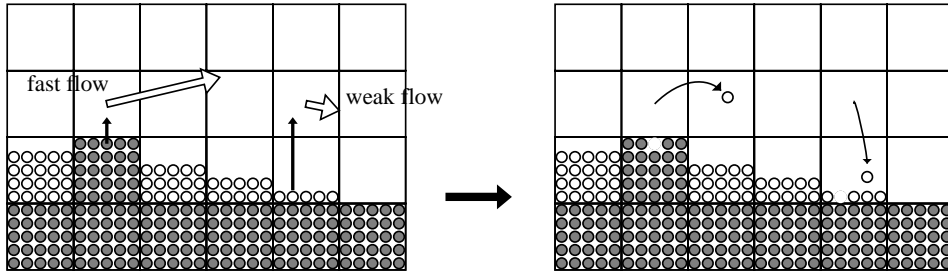


Fig. 38. Erosion rule. Eroded particles are pushed on the upper lattice site, where they are again subject to the transport rule.

If the local fluid velocity is fast enough, the particle will be picked up and moved further away due to our transport rule. Otherwise, if the flow is slow, the resulting motion will be to land again on the same site where the particle started off, see Fig. 38.

4.9.2. Validation

To validate the erosion and transport rules in a simple situation, we first consider the case of the jump length distribution described in Fig. 39. This problem has been studied outdoors experimentally in the case of snow transport by Kobayashi [103]. The experiment consists in collecting the amount of snow transported by wind and landing in successive boxes placed along its path. The same experiment can be performed with our computer model [116]. The result shown in Fig. 39 shows the very good agreement with experimental findings.

As the next validation of the model, we present a simulation of scour formation underneath a submarine pipe subject to a steady water current. This is a well-studied problem, due to its practical importance in marine engineering [182].

The scenario of the process is sketched in Fig. 40. The scour which forms under the pipe occurs as follows. First both vortices in front of and behind the pipe dig up a hole. When these holes meet each other under the pipe, water starts to flow underneath and the main erosion stage takes place.

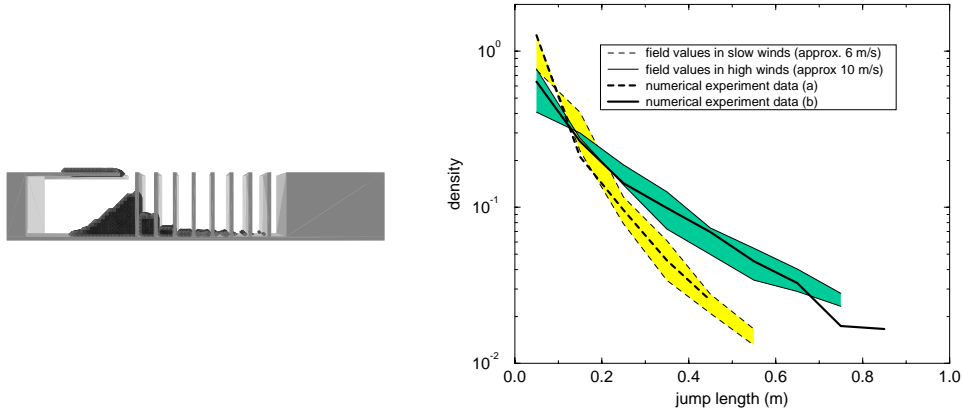


Fig. 39. Comparison of jump length distribution of snow particles in field experiment and the corresponding numerical simulations. The upper panel shows the setting used for the simulation, and the graph reports the quantity of snow gathered as a function of the distance to the source of snow, for a weak and a strong wind. Shaded areas indicate the values obtained in field measurements.

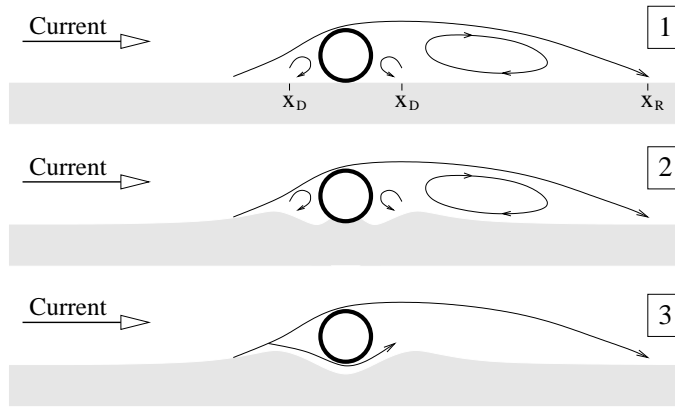


Fig. 40. Three main stages of the scour onset process under unidirectional current. (1) Due to the current, three main vortices appear in the pipe neighborhood. (2) The two small vortices up and downstream the pipe start to dig a hole. (3) After a while, the holes meet each other below the pipe and the scour formation process breaks out. x_D and x_R denote reattachment points.

Various laboratory experiments (see for example Ref. 182 and references therein) show that the equilibrium depth of the scour depends essentially on the pipe diameter D and that the ratio between the scour depth and the pipe diameter should be comprised between 0.2 and 1.0. These features are well captured by our LB-CA approach. Figure 41 shows the result of numerical simulations and compares the predicted scour profile with laboratory experiments [113]. As can be seen, the model and the experiment are in good agreement. More details can be found in Ref. 58.

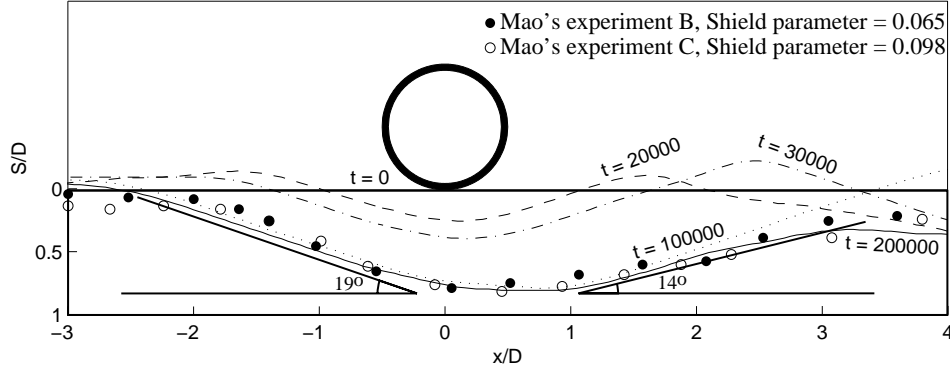


Fig. 41. Numerical simulation of the scour under a submarine pipe. The black and white dots are laboratory profiles.

5. Remarks on Lattice Boltzmann Fluids

5.1. Thermal and compressible models

LB fluids (as well as CA fluids) are intrinsically compressible. However, as with any Newtonian fluid, density variations can be neglected (except in the pressure term) if the Mach number M is small enough [171]. Therefore, for small \vec{u} and without gravity type forces, one observes an incompressible regime. Also, for small \vec{u} , terms of order u^3 can be safely ignored in the mathematical derivation of the Navier–Stokes equation from the LB dynamics. When u increases to reach the compressible domain, terms of order $O(u^3)$ are no longer negligible in the local equilibrium. A possible solution is to add new terms [29], of order u^4 , which may be needed in expression (4.7).

The same problem holds for thermal models because terms up to $O(M^4)$ are required. Increasing the lattice isotropy and expanding $f^{(0)}$ to fourth order in u is also a possible solution to remove spurious non-linear deviations [29]. Another suggested approach [147] is to consider primary and secondary local equilibrium functions. First, the ratios of the local equilibria corresponding to different energy levels are computed from the standard Maxwell–Boltzmann distribution. Then, the $f_i^{(0)}$ are expressed in terms of these ratios and the physical quantities ρ , \vec{u} and T through the conservation laws.

Another difficulty of thermal models is that the Prandtl number (ratio of the viscosity to the heat conductivity) is not adjustable. A two-time BGK model has been proposed to offer more flexibility [28]. The collision term for f_i contains a usual relaxation $(f_i^{(0)} - f_i)/\tau_1$ plus a new term $(f_{i'}^{(0)} - f_{i'})/\tau_2$, where i' denotes the direction opposite to i . This formulation yields an adjustable Prandtl number at the price of some inconsistency in the thermohydrodynamic equations [28].

The high compressibility of LB fluids is sometimes viewed as a drawback of the method since it restricts the simulation of incompressible flows to the regime of low

Mach numbers [195]. In order to model a truly incompressible fluid, it has been suggested to use the pressure p instead of ρ as an independent dynamic variable [79]. Another possibility [28] is to redefine the fluid flow as $\vec{w} = \vec{u} + \vec{\nabla}\phi$, where \vec{u} has the usual definition (4.4) in terms of the f_i 's and ϕ satisfies $\nabla^2\phi = \text{div } \vec{u}$. See also Ref. 165.

5.2. Non-ideal systems and multicomponent fluids

A great deal of effort has been devoted to go beyond ideal systems (where the scalar pressure p is proportional to ρT) and to model, for instance, van der Waals interactions and liquid-gas transition. To this end, the Shan and Chen model [160] adds a nearest-neighbor interaction between the LB particles. This force is specified by an adjustable function Ψ of the particle density at each lattice site and causes a change of the momentum of the particles. This momentum change is implemented by replacing \vec{u} in $f^{(0)}$ (see (4.7)) by \vec{u}' computed as

$$\rho\vec{u}'(\vec{r}) = \sum_i f_i\vec{v}_i - \tau G\Psi(\rho(\vec{r})) \sum_i \Psi(\rho(\vec{r} + \Delta_t\vec{v}_i))\vec{v}_i.$$

Since this interaction is mutual, it can be shown that momentum is still conserved over the system.

The effect of this force is to add a non-ideal gas correction $\propto G\Psi^2(\rho)$ to the ideal gas expression $p_0 = c_s^2\rho$. A temperature-like parameter, proportional to c_s^2/G can be tuned to control the liquid-gas transition. This approach gives good results for equilibrium simulations (Laplace law, density profile at an interface, etc). However, as pointed out in Ref. 168, this method is not consistent with the concept of a free energy and spurious diffusive terms appear in the continuity equation [168]. In addition, no energy equation is included. An extension of the Shan–Chen model to describe multicomponent fluids is given in Ref. 115.

A different approach has been proposed by Swift *et al.* [168] in order to be consistent, at equilibrium, with the free energy construction of the Cahn–Hilliard theory [23]. For a non-ideal single component fluid one writes

$$\sum_i f_i^{(0)} v_{i\alpha} v_{i\beta} = P_{\alpha\beta} + \rho u_\alpha u_\beta,$$

where the pressure tensor $P_{\alpha\beta}$ is computed from a free energy function given as an input. The effect of the interaction comes in the second moment of $f^{(0)}$ whereas it enters in the first moment in the Shan–Chen model.

In order to match the desired expression of $P_{\alpha\beta}$, the local equilibrium approach is complemented as [168]:

$$f_i^{(0)} = a_i\rho + \frac{b}{v^2}\rho\vec{v}_i \cdot \vec{u} + \rho e_i \frac{u^2}{v^2} + \rho \frac{h}{v^4} v_{i\alpha} v_{i\beta} u_\alpha u_\beta + G_{\alpha\beta} \frac{v_{i\alpha} v_{i\beta}}{v^2}. \quad (5.1)$$

For the case of a van der Waals gas, an explicit expression is known in terms of the temperature and the density and its derivative. The derivative of the density is computed by finite differences on the lattice.

A correct coexistence curve is obtained from this model, as well as physically sound density variations through a flat interface or droplets. The kinetics of the model (how equilibrium is approached) is in the universality class of model A. However, some breaking of the Galilean invariance appears for droplets in a constant speed flow.

The Swift *et al.* model also applies to a binary fluid. If the densities of the two fluids are respectively ρ_1 and ρ_2 , one defines two sets of distribution functions, f and g such that

$$\rho = \rho_1 + \rho_2 = \sum_i f_i, \quad \Delta\rho = \rho_1 - \rho_2 = \sum_i g_i, \quad \rho\vec{u} = \sum_i f_i\vec{v}_i.$$

Both the f_i and g_i obey the lattice BGK equation (4.3), each with a different relaxation time τ_1 and τ_2 . Since the two densities are independent, one has three conservation laws (for ρ , $\rho\vec{u}$ and $\Delta\rho$) to determine the coefficients of the expressions for $f_i^{(0)}$ and $g_i^{(0)}$ (given by an expression similar to Eq. (5.1)). In addition one imposes the second moments as

$$\begin{aligned} \sum_i f_i^{(0)} v_{i\alpha} v_{i\beta} &= P_{\alpha\beta} + \rho u_\alpha u_\beta, \\ \sum_i g_i^{(0)} v_{i\alpha} v_{i\beta} &= \Gamma \Delta\mu \delta_{\alpha\beta} + \Delta\rho u_\alpha u_\beta, \end{aligned}$$

where Γ is the mobility and $\Delta\mu$ the chemical potential. From a free energy construction, an explicit expression for $\Delta\mu$ and $P_{\alpha\beta}$ can be obtained for two ideal gases with repulsive forces.

The basic properties of a binary mixture is well reproduced within this model, although some spurious velocities are observed in the interface. As expected (conservation of the order parameter) the kinetics of this model belongs to model B universality class. As in the Shan–Chen model, the fundamental problem of this approach is the absence of an energy equation, as well as the absence of a H-theorem.

Historically, the first model proposed to simulate a two-component, immiscible fluid system is probably that of Rothman and Keller [153, 154, 155]. It was first devised as a CA model and then extended to the LB scheme [76].

The two immiscible fluids (say a blue one and a red one) interact so as to conserve the total momentum $\rho\vec{u}$ and the densities ρ_1 and ρ_2 of each species. The immiscible character of the system is obtained by defining a color gradient $\vec{q} = \sum_i [\Delta\rho(\vec{r} + \Delta_t\vec{v}_i)]\vec{v}_i$ where $\Delta\rho$ is the density difference. As in the Swift model above, the f_i describe the sum of the fluids and g_i their difference. In a first step, the f_i are computed from a standard, ideal gas lattice BGK equation. Then, the f_i are modified according to the color gradient as follows:

$$f_i \rightarrow f_i + |q| \cos 2\Phi_i,$$

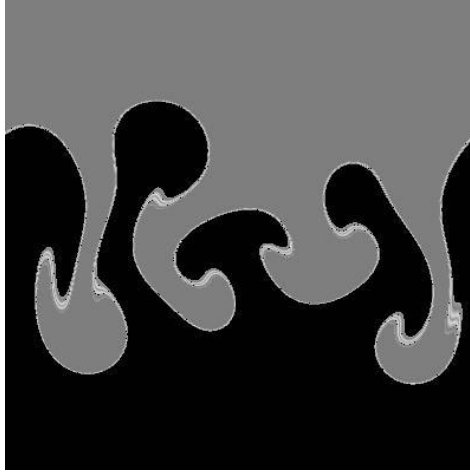


Fig. 42. Rayleigh–Taylor instability obtained by a simulation of two LB fluid subject to a repulsion as defined in the Shan and Chen model.

where $\cos \Phi_i = (\vec{q}_i \cdot \vec{v}_i) / (|\vec{q}_i| |\vec{v}_i|)$. Since $\cos 2\Phi_i = 2 \cos^2 \Phi_i - 1$, it is easy to check that the new f_i preserves the total mass and the total momentum. This construction is equivalent to define a modified local equilibrium function, as is Eq. (5.1), but with a different expression for the $G_{\alpha\beta}$ [168]. The second step of the microdynamics is a numerical optimization phase which consists of maximizing the scalar product of \vec{q} with the color flux $\sum_i g_i \vec{v}_i$.

This two-color dynamics is quite intuitive but, as opposed to the Swift model, it is not consistent with the concept of a free energy. Also the quantities $\sum_i g_i^{(0)} \vec{v}_i$ and $\sum_i g_i^{(0)} v_{i\alpha} v_{i\beta}$ have no obvious physical interpretations.

Finally, the Shan and Chen model can be modified to deal simply and naturally with a multicomponent fluid [115]. The interaction (repulsive for immiscible fluids) is implemented as an exchange of momentum between different fluid components at nearest neighbor sites. Figure 42 shows the results of a two-component immiscible model in which the upper fluid is heavier (gravity is added) than the lower one. This situation corresponds to the so-called Rayleigh–Taylor instability described in more detail in Sec. 3.10 (see also Ref. 130).

Other models of multicomponent fluids can be found in Refs. 33, 52, 65, 74. Figure 43 shows an example of the formation of meniscus in a capillary tube in a simplified two-component system (see Ref. 33).

5.3. Stability and H-theorem

While CA fluids are intrinsically stable from a numerical point of view, LB fluids are not. At low viscosity ($\tau \rightarrow 1/2$) and with high velocity gradients, numerical instabilities develop. One possibility to circumvent this problem is to use a subgrid model, as discussed in Sec. 4.8.

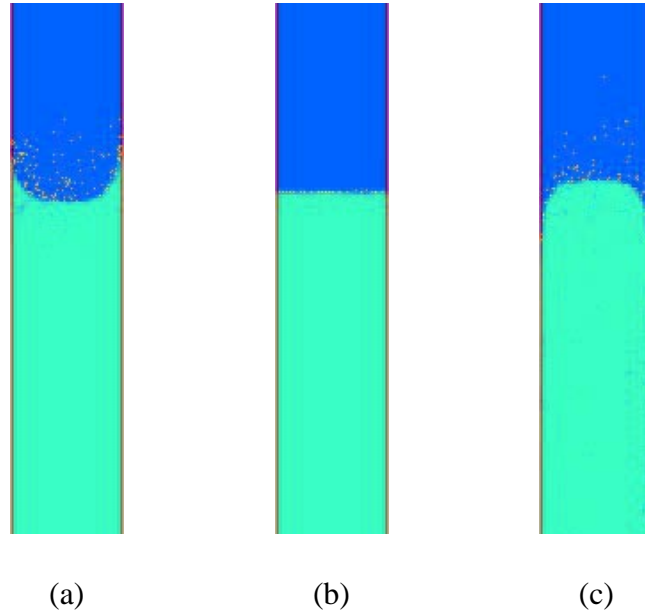


Fig. 43. Free surface of a liquid in a capillary tube: (a) a wetting situation; (b) inert walls; and (c) a non-wetting situation.

An interesting way to improve stability is the so-called *moment method* [105], where the LB dynamics is expressed in terms of new quantities ϕ_i obtained from an orthogonalization of the f_i 's.

A more first principle approach to the stability problem is based on the idea of a H-theorem. In CA fluids, a H-theorem has been shown to exist [66]. This is not the case for LB systems. Boghosian (see Ref. 12) proposes that the limit ($\tau \rightarrow 1/2$) may violate the second principle of thermodynamics, thus explaining the instability. Other authors [62, 98, 178] show how to construct local equilibrium functions $f^{(0)}$ which satisfy Eqs. (4.8) and (4.10) while minimizing a convex function $H(f)$, called the entropy function. For the case of the D2Q9 model, it is found [62] that, up to the desired order of accuracy ($O(u^2)$ in this case), the standard expression (4.7) for $f^{(0)}$, with the extra condition that $c_s^2 = v^2/3$ is consistent with a convex entropy function $H = \sum_i f_i(1 - f_i) + \sum_i \gamma_i f_i$, where γ_i are some constants.

The existence of a H-function can be used to define the evolution rule of a LB scheme in a thermodynamically consistent way. If the input state is a given set of f_i , the output set f'_i is constructed as $(1 - \beta)f_i + \beta f_i^*$, where β is a parameter similar to the relaxation time and f^* is an auxiliary state obeying the hydrodynamic constraints and defined as the most distant state so that either $H(f) = H(f^*)$ or $f_i^* > 0$. Preliminary numerical simulations with this approach show a significant improvement of the numerical stability at low viscosity [128]. A detailed comparison with the subgrid approach is still to be investigated.

Among the other possibilities to alleviate numerical instabilities, one can also mention grid refinement techniques [57, 63, 106] in which spatial regions where gradients are important are locally discretized with a finer mesh of spacing Δ_r/n , where n is the refinement degree. Some other approaches are based on the extensions of the LB models to irregular grids (see Sec. 5.4).

Finally another way to remedy the instability problem is to define multiparticle models which lie in between the CA and LB approaches, as discussed in Sec. 7.

5.4. Irregular meshes

Most current LB models are defined on a regular lattices, while CFD techniques can deal with arbitrary irregular meshes. For some applications where the geometry cannot be fitted by a regular lattice, this may appear as a strong limitation. However, irregular mesh generation is a tough problem, which take a lot of CPU time for complicated geometries. Therefore, the Cartesian grid used in LB model can also be seen as positive aspect of the approach. Off-lattice boundary conditions [165] can be used to implement very complex geometries, leading to efficient numerical simulation, for instance in the automotive industry. Nevertheless, some efforts have been devoted to extend LB models to irregular lattices [166].

A possible approach is to separate the space-time discretization from the velocity discretization. For instance one may assume an underlying continuous space-time Boltzmann equation with *discrete velocities* and express its evolution on a coarse grain discrete spatial mesh. Note that discrete velocity Boltzmann models are a well known topic which has developed somehow independently of the CA and LB stream [20, 46].

Recently, He and Luo [80] have proposed an *a priori* derivation of the BGK lattice scheme (4.3) starting from a continuous space-time Boltzmann equation, with the standard Maxwell–Boltzmann distribution as a local equilibrium function. They present a general procedure to systematically derive discrete velocity models and to enforce the correct values of the momenta of $f^{(0)}$ for irregular meshes. As an example, LB simulations of the backward-facing step flow confirms the possibility to refine the mesh in regions where more accuracy is needed.

A key ingredient in the formulation of LB models on an irregular grid is the interpolation procedure which is necessary for the propagation step (particles no longer have a velocity which connects them naturally to the next grid point). This is a fundamental difference with the usual LB approach [80].

Peng *et al.* [135, 136] gives a finite volume formulation of the LB approach and shows a very good agreement between simple LB flows on a totally unstructured mesh and exact solution of the Navier–Stokes equation. While it retains much of the flexibility of the standard LB scheme, this method is numerically more involved.

A current trend is to adapt standard CFD techniques to the LB framework. For instance, implicit schemes for solving a Boltzmann equation with discrete velocities

on non-uniform meshes is discussed by Krafczyk in Ref. 12. The result is that the implicit discretization method may be of significant advantage for high Reynolds stationary flows.

6. Reaction-Diffusion Systems

Diffusive phenomena and reaction processes play an important role in many areas of physics, chemistry and biology and still constitute an active field of research. Systems in which reactive particles are brought into contact by a diffusion process and transform, often give rise to very complex behaviors. Pattern formation [124, 133], is a typical example of such a behavior in reaction-diffusion processes.

In addition to a clear academic interest, reaction-diffusion phenomena are also quite important in technical sciences and still constitute numerical challenges. As an example, we may mention the famous problem of carbonation in concrete [18, 70].

In many reaction-diffusion problems a particle based model, such as a lattice gas dynamics, provides a useful approach and efficient numerical tool.

For instance, processes such as aggregation, formation of a diffusion front, trapping of particles performing a random walk in some specific region of space [179, 180], or the adsorption of diffusing particles on a substrate [110] are important problems that are difficult to solve with the standard diffusion equation. A microscopic model, based on a cellular automata dynamics, is therefore of clear interest.

Reaction processes, as well as growth mechanisms are most of the time non-linear phenomena, characterized by a threshold dynamics. While they are naturally implemented in terms of a point-particles description they may be very difficult to analyze theoretically and even numerically, with standard techniques, due to the important role that fluctuations may play. In the simplest cases, fluctuations are responsible for symmetries breaking which may produce interesting patterns, as we shall see later in this section.

More surprisingly, microscopic fluctuations are sometimes relevant at a macroscopic level of observation because they may induce an anomalous dynamics, as in the $A + A \rightarrow 0$ or $A + B \rightarrow 0$ annihilation reactions [44, 45]. These systems depart from the behavior predicted by the classical approach based on differential equations for the densities. The reason is that they are fluctuations-driven and that correlations cannot be neglected. In other words, one has to deal with a full N-body problem and the Boltzmann factorization assumption is not valid. For this kind of problem, a lattice gas automata approach turns out to be a very successful approach.

Cellular automata particles can be equipped with diffusive and reactive properties, in order to mimic real experiments and model several complex reaction-diffusion-growth processes, in the same spirit as a cellular automata fluid simulates a fluid flow: these systems are expected to retain the relevant aspects of the microscopic world they are modeling. Diffusion can be obtained with the rule described

in Sec. 2.6. Chemical reactions, such as $A + B \rightarrow C$, are treated in an abstract way, as a particle transformation phenomena rather than a real chemical interaction.

Within the CA approach, there are two ways of modeling a spatially extended system with local reactive interactions. The first one is to use a standard CA scheme: each cell is updated according to the state of its neighbors. The second way is to consider a lattice gas (LG) approach. As already mentioned, LG are a particular class of cellular automata, characterized by a two-phase dynamics: first, a completely local interaction on each lattice point, and then particle transport (or propagation) to nearest-neighbor sites. This way of partitioning the space prevents the problem of having a particle simultaneously involved in several different interactions.

Here we shall start the discussion with the first kind of model. Some reactive phenomena can be nicely described by simple rules, without the space partitioning of the LG paradigm. In Sec. 6.1, we present a model of excitable media in which chemical waves are observed and, in Sec. 6.2, we shall see an example of a surface reaction on a catalytic substrate.

Then, in Sec. 6.3, we shall concentrate on the LG approach which is well suited to represent many reaction-diffusion processes in terms of fictitious particles evolving in a discrete universe. We shall first present the generic model for diffusion with only one species of particles. The approach can be extended to the case where several different chemical species coexist simultaneously on the same lattice and diffuse. It just requires more bits of information to store the extra automaton states. Then, it is easy to supplement the diffusion rule with the annihilation or creation of particles of a different kind, depending on the species present at each lattice site and the reaction rule under study.

The microdynamics will be given, as well as its link to macroscopic rate equations. The corresponding LB extension will be discussed too. As an illustration of the method, an application to the formation of patterns of precipitate in a reaction-diffusion process (the so-called Liesegang structures) will be presented.

Note that in Sec. 7, we shall consider other reaction-diffusion processes, using the multiparticle method. Other examples and applications can be found in Ref. 17.

6.1. *Excitable media*

An excitable medium is basically characterized by three states [17]: the resting state, the excited state and the refractory state. The resting state is a stable state of the system. But a resting state can respond to a local perturbation and become excited. Then, the excited state evolves to a refractory state where it no longer influences its neighbors and, finally, returns to the resting state.

A generic behavior of excitable media is to produce chemical waves of various geometries [96, 101]. Ring and spiral waves are a typical pattern of excitations. Many chemical systems exhibits an excitable behavior. The Selkov model [159] and the Belousov–Zhabotinsky reaction are examples. Chemical waves play an important role in many biological processes (nervous systems, muscles) since they can mediate the transport of information from one place to another.

The Greenberg–Hasting model is an example of a cellular automata model of an excitable media. This rule, and its generalization, have been extensively studied [64, 72].

The implementation we propose here for the Greenberg–Hasting model is the following: the state $\phi(\vec{r}, t)$ of site \vec{r} at time t takes its value in the set $\{0, 1, 2, \dots, n-1\}$. The state $\phi = 0$ is the resting state. The states $\phi = 1, \dots, n/2$ (n is assumed to be even) correspond to excited states. The rest, $\phi = n/2 + 1, \dots, n-1$ are the refractory states. The cellular automata evolution rule is the following:

- (i) If $\phi(\vec{r}, t)$ is excited or refractory, then $\phi(\vec{r}, t+1) = \phi(\vec{r}, t) + 1 \bmod n$.
- (ii) If $\phi(\vec{r}, t) = 0$ (resting state) it remains so, unless there are at least k excited sites in the Moore neighborhood of site \vec{r} . In this case $\phi(\vec{r}, t) = 1$.

The n states play the role of a clock: an excited state evolves through the sequence of all possible states until it returns to 0, which corresponds to a stable situation.

The behavior of this rule is quite sensitive to the value of n and the excitation threshold k . Figures 44 and 45 show the evolution of this automaton for two different sets of parameters n and k . Both simulations are started with a uniform configuration of resting states, perturbed by some excited sites randomly distributed over the system. If the concentration of perturbation is low enough, excitation dies out

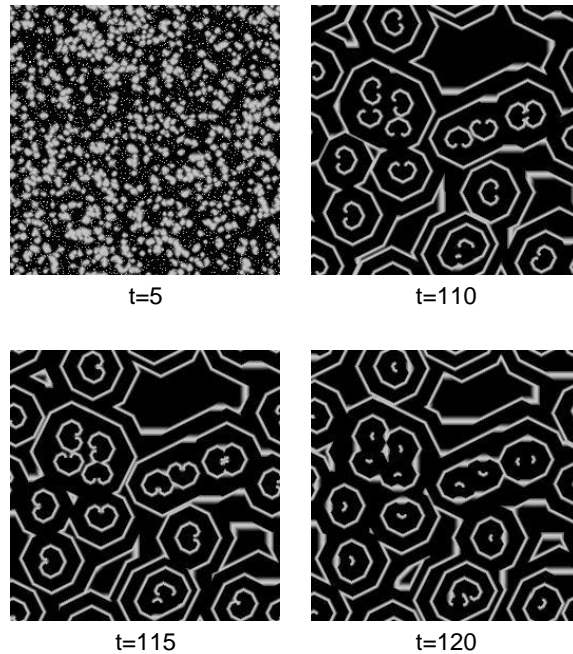


Fig. 44. Excitable medium: evolution of a stable initial configuration with 10% of excited states $\phi = 1$, for $n = 10$ and $k = 3$. The color black indicates resting states. After a transient phase, the system sets up in a state where pairs of counter-rotating spiral waves propagate. When the two extremities come into contact, a new, similar pattern is produced.

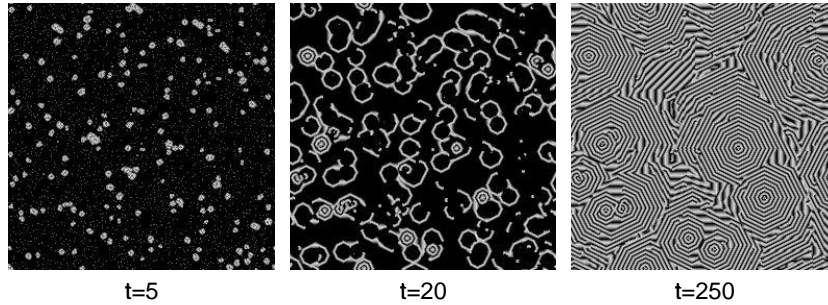


Fig. 45. Excitable medium: evolution of a configuration with 5% of excited states $\phi = 1$, and 95% of resting states (black), for $n = 8$ and $k = 3$.

rapidly and the system returns to the rest state. Increasing the number of perturbed states leads to the formation of traveling waves and self-sustained oscillations may appear in the form of ring or spiral waves.

The Greenberg–Hasting model has some similarity with the “tube-worms” rule proposed by Toffoli and Margolus [169]. This rule is intended to model the Belousov–Zhabotinsky reaction and is as follows. The state of each site is either 0 (refractory) or 1 (excited) and a local timer (whose value is 3, 2, 1 or 0) controls the refractory period. Each iteration of the rule can be expressed by the following sequence of operations: (i) where the timer is zero, the state is excited; (ii) the timer is decreased by 1 unless it is 0; (iii) a site becomes refractory whenever the timer is equal to 2; (iv) the timer is reset to 3 for the excited sites which have two, or more than four, excited sites in their Moore neighborhood.

Figure 46 shows a simulation of this automaton, starting from a random initial configuration of the timers and the excited states. We observe the formation of spiral pairs of excitations. Note that this rule is very sensitive to small modifications (in particular to the order of operations (i) to (iv)).

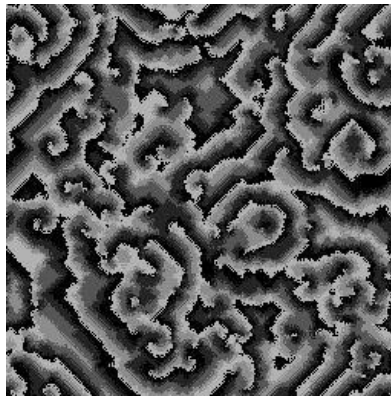


Fig. 46. The tube-worms rule for an excitable media.

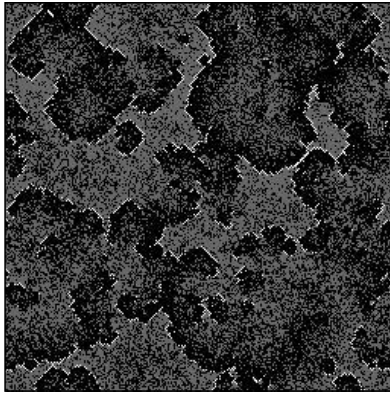


Fig. 47. The forest fire rule: grey sites correspond to a grown tree, black pixels represent burned sites and the white color indicates a burning tree. The snapshot given here represents the situation after a few hundred iterations. The parameters of the rule are $p = 0.3$ and $f = 6 \times 10^{-5}$.

Another rule which is also similar to Greenberg–Hasting and Margolus–Toffoli tube-worm models is the so-called forest-fire model. This rule describes the propagation of a fire or, in a different context, may also be used to mimic contagion in case of an epidemic. Here we describe the case of a forest-fire rule.

The forest-fire rule is a probabilistic CA defined on a d -dimensional hypercubic lattice. Initially, each site is occupied by either a tree, a burning tree or is empty. The state of the system is parallel updated according to the following rule: (1) a burning tree becomes an empty site; (2) a green tree becomes a burning tree if at least one of its nearest neighbors is burning; (3) at an empty site, a tree grows with probability p ; (4) A tree without a burning nearest neighbor becomes a burning tree during one time step with probability f (lightning).

Figure 47 illustrates the behavior of this rule, in a two-dimensional situation. Provided that the time scales of tree growth and burning down of forest clusters are well separated (i.e. in the limit $f/p \rightarrow 0$), this model has self-organized critical states [53]. This means that in the steady state, several physical quantities characterizing the system have a power law behavior. For example, the cluster size distribution $\mathcal{N}(s)$ and radius of a forest cluster $\mathcal{R}(s)$ vary with the number of trees s in the forest cluster as $\mathcal{N}(s) \sim s^{-\Delta_t} \mathcal{C}(s/s_{\max})$ and $\mathcal{R}(s) \sim s^{1/\mu} \mathcal{S}(s/s_{\max})$. Scaling relations can be established between the critical exponents Δ_t and μ , and the scaling functions \mathcal{C} and \mathcal{S} can be computed.

6.2. Surface reaction models

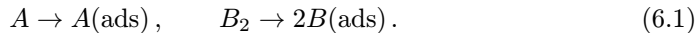
The problem of non-equilibrium phase transition is an important topics in physics. The situation is not as clear as it is for equilibrium systems and no general theory is available to describe such systems. Most of the known results are based on numerical simulations. However, as is the case for equilibrium systems, the concept of universality classes appears to be relevant although we do not completely under-

stand how the universality classes are characterized.

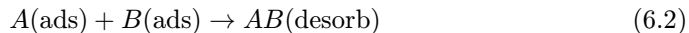
In this section, we discuss the case of a non-equilibrium phase transition in a simple model of reaction on a catalytic surface. The system is out of equilibrium because it is an open system in which material continuously flows in and out. However, after a while, it reaches a stationary state and, depending on some control parameters, may be in different phases.

The system we shall consider is the so-called Ziff model [194]. This model is based upon some of the known steps of the reaction $A - B_2$ on a catalyst surface (for example $\text{CO} - \text{O}_2$). The basic steps are

- A gas mixture with concentrations X_{B_2} of B_2 and X_A of A sits above the surface and can be adsorbed. The surface can be divided into elementary cells. Each cell can adsorb one atom only.
- The B species can be adsorbed only in the atomic form. A molecule B_2 dissociates into two B atoms only if two adjacent cells are empty. Otherwise the B_2 molecule is rejected. The first two steps correspond to the reactions



- If two nearest neighbor cells are occupied by different species they chemically react according to the reaction



and the product of the reaction is desorbed. In the example of the $\text{CO} - \text{O}_2$ reaction, the desorbed product is a CO_2 molecule.

This final desorption step is necessary for the product to be recovered and for the catalyst to be regenerated. However, the gas above the surface is assumed to be continually replenished by fresh material so that its composition remains constant during the whole evolution.

It is found by *sequential* numerical simulation [194] that a reactive steady state occurs only in a window defined by

$$X_1 < X_A < X_2,$$

where $X_1 = 0.389 \pm 0.005$ and $X_2 = 0.525 \pm 0.001$ (provided that $X_{B_2} = 1 - X_A$). This situation is illustrated in Fig. 48, though for the corresponding cellular automata dynamics and $X_{B_2} \neq 1 - X_A$.

Outside this window, the steady state is a “poisoned” catalyst of pure A ($X_A > X_2$) or pure B ($X_A < X_1$). For $X_A > X_1$, the coverage fraction varies continuously with X_A and one speaks of a continuous (or second-order) non-equilibrium phase transition. At $X_A = X_2$, the coverage fraction varies discontinuously with X_A and one speaks of a discontinuous (or first-order) non-equilibrium phase transition. The asymmetry of behavior at X_1 and X_2 comes from the fact that A and B atoms have a different adsorption rule: two vacant adjacent sites are necessary for B to stick on the surface, whereas one empty site is enough for A .

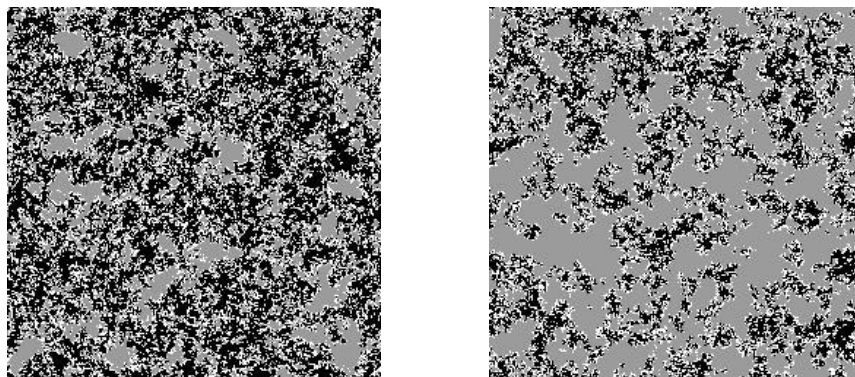


Fig. 48. Typical microscopic configuration in the stationary state of the CA Ziff model, where there is coexistence of the two species. The simulation corresponds to the generalized model described by rules R1, R2, R3 and R4 below. The gray and black dots represent, respectively, the A and B particles, while the empty sites are white. The control parameter X_A is larger in the right image than it is in the left one.

From a physical point of view, the dynamics of such a system is not sequential since many cells can be reacting simultaneously, within a given small time interval. A parallel, asynchronous dynamics would then be a more realistic updating scheme. However, it is interesting to study the Ziff model with a fully parallel, synchronous cellular automata dynamics [31], which represents the other limiting case.

In a CA approach the elementary cells of the catalyst are mapped onto the cells of the automaton. In order to model the different processes, each cell j can be in one of four different states, denoted $|\psi_j\rangle = |0\rangle, |A\rangle, |B\rangle$ or $|C\rangle$.

The state $|0\rangle$ corresponds to an empty cell, $|A\rangle$ to a cell occupied by an atom A , and $|B\rangle$ to a cell occupied by an atom B . The state $|C\rangle$ is artificial and represents a precursor state describing the conditional occupation of the cell by an atom B . Conditional means that during the next evolution step of the automaton, $|C\rangle$ will become $|B\rangle$ or $|0\rangle$ depending upon the fact that a nearest neighbor cell is empty and ready to receive the second B atom of the molecule B_2 . This conditional state is necessary to describe the dissociation of B_2 molecules on the surface.

The main difficulty when implementing the Ziff model with a fully synchronous updating scheme is to ensure that the correct stoichiometry is obeyed. Indeed, since all atoms take a decision at the same time, the same atom could well take part in a reaction with several different neighbors, unless some care is taken.

The solution to this problem is to add a vector field to every site in the lattice [193], as shown in Fig. 49. A vector field is a collection of arrows, one at each lattice site, that can point in any of the four directions of the lattice. The directions of the arrows at each time step are assigned randomly. Thus, a two-site process is carried out only on those pairs of sites in which the arrows point toward each other (matching nearest-neighbor pairs (MNN)). This concept of *reacting matching pairs* is a general way to partition the parallel computation in local parts.

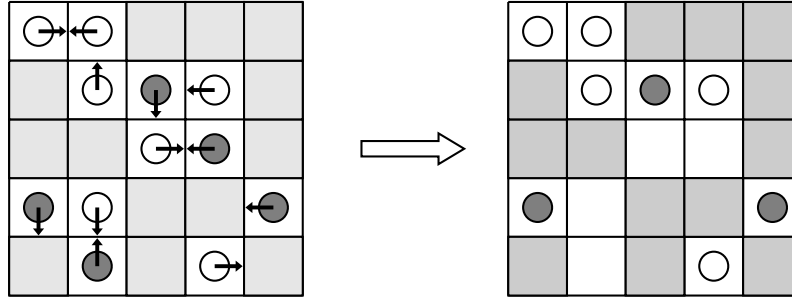


Fig. 49. Illustration of rules R2 and R3. The arrows select which neighbor is considered for a reaction. Dark and white particles represent the A and B species, respectively. The shaded region corresponds to cells that are not relevant to the present discussion such as, for instance, cells occupied by the intermediate C species.

In the present implementation, the following generalization of the dynamics is included: an empty site remains empty with some probability. One has then two control parameters to play with: X_A and X_{B_2} that are the arrival probability of an A and a B_2 molecule, respectively.

Thus, the time evolution of the CA is given by the following set of rules, fixing the state of the cell j at time $t + 1$, $|\psi_j\rangle(t + 1)$, as a function of the state of the cell j and its nearest neighbors (von Neumann neighborhood) at time t . Rules R1, R4 describe the adsorption-dissociation mechanism while rules R2, R3 (illustrated in Fig. 49) describe the reaction-desorption process.

R1: If $|\psi_j\rangle(t) = |0\rangle$ then

$$|\psi_j\rangle(t + 1) = \begin{cases} |A\rangle & \text{with probability } X_A \\ |C\rangle & \text{with probability } X_{B_2} \\ |0\rangle & \text{with probability } 1 - X_A - X_{B_2}. \end{cases} \quad (6.3)$$

R2: If $|\psi_j\rangle(t) = |A\rangle$ then

$$|\psi_j\rangle(t + 1) = \begin{cases} |0\rangle & \text{if the MNN of } j \text{ was in the} \\ & \text{state } |B\rangle \text{ at time } t \\ |A\rangle & \text{otherwise.} \end{cases} \quad (6.4)$$

R3: If $|\psi_j\rangle(t) = |B\rangle$ then

$$|\psi_j\rangle(t + 1) = \begin{cases} |0\rangle & \text{if the MNN of } j \text{ was in the} \\ & \text{state } |A\rangle \text{ at time } t \\ |B\rangle & \text{otherwise.} \end{cases} \quad (6.5)$$

R4: If $|\psi_j\rangle(t) = |C\rangle$ then

$$|\psi_j\rangle(t + 1) = \begin{cases} |B\rangle & \text{if MNN is in the state } |C\rangle \text{ at time } t \\ |0\rangle & \text{otherwise.} \end{cases} \quad (6.6)$$

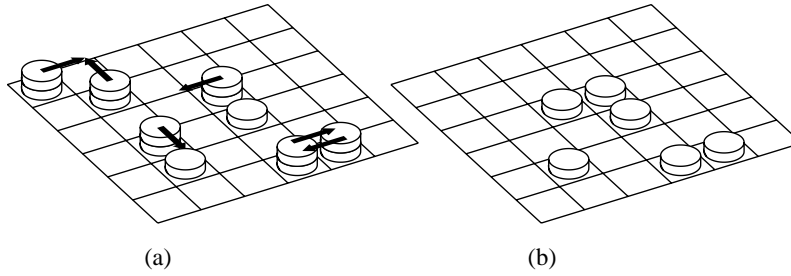


Fig. 50. Dissociation rule R4. The B_2 molecule (or C state) is represented as two disks on top of each other. Dissociation is possible if the upper disk can move to the site indicated by the arrow without conflict with other moves.

In addition, Eq. (6.6) is supplemented by the following rule: a cell in the intermediate state C will give two adjacent B atoms if its matching arrow points to an empty site which is not pointed to by another C state. Rule R4 is illustrated in Fig. 50.

Figure 48 shows typical stationary configurations obtained with a cellular automata version of the Ziff model. At time $t = 0$, all the cells are empty and a randomly prepared mixture of gases with fixed concentrations X_A and X_{B_2} sits on top of the surface. The rules are iterated until a stationary state is reached. The stationary state is a state for which the mean coverage fractions X_A^a and X_B^a of atoms of type A or B does not change in time, although microscopically the configurations of the surface changes.

The phase diagram obtained for this generalized CA Ziff model is given in Fig. 51, with the value $X_{B_2} = 0.1$. This phase diagram is topologically similar to the sequential updating case (with $X_{B_2} = 1 - X_A$) since we observe a first and a second order transition surrounding a region of coexistence of both species. However the

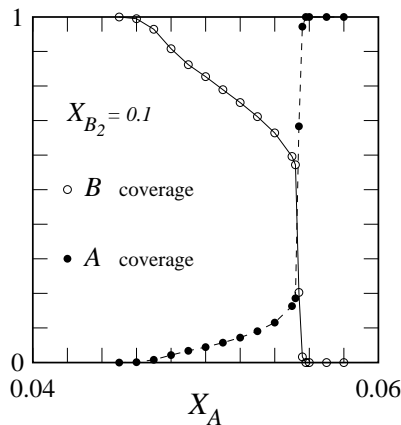


Fig. 51. Stationary state phase diagram corresponding to the CA Ziff model.

locations of the critical points are different, illustrating the non-universal character of these quantities.

6.3. The reaction-diffusion rule

In this section we shall introduce a LGA model for reaction-diffusion processes. Our model will be very similar in spirit to the cellular automata fluids discussed in Sec. 3 except that, here, the collision rule will reproduce a diffusive behavior and implement some particle transformations. We shall first discuss the diffusion rule and then show how a reaction term can be included.

6.3.1. The diffusion rule

At a microscopic level of description, a diffusive phenomena corresponds to the random walk of many particles. Particle number is conserved but not momentum. This random motion is typically due to the properties of the environment the particles are moving in. When one is not interested in an explicit description of this environment, it can be considered as a source of thermal noise and its effective action on the particles can be assumed to be stochastic. Thus, the CA rule proposed in Sec. 2.6 gives us the basic model for diffusion.

This evolution rule requires random numbers and then corresponds to a *probabilistic* cellular automaton.

Thus, our diffusion model consists of particles moving along the main directions of a hypercubic lattice (a square lattice in two dimensions or a cubic lattice in three dimensions). As opposed to cellular automata fluids, we do not have to consider here more complicated lattices. The reason is that diffusion processes do not require a fourth-order tensor for their description. The random motion is obtained by permuting the direction of the incoming particles. If d is the space dimension, there are $2d$ lattice directions. These $2d$ directions of motion can be shuffled in $2d!$ ways, which is the number of permutations of $2d$ objects. However, it is not necessary to consider all permutations. A subset of them is enough to produce the desired random motion and, as in Sec. 2.6, we restrict ourselves to cyclic permutations. Thus, at each time step, the directions of the lattice are “rotated” by an angle α_i chosen at random, with probability p_i , independently for each site of the lattice. With this mechanism, the direction a particle will exit a given site depends on the direction it had when entering the site. The modification of its velocity determines its next location on the lattice.

By labeling the lattice directions with the unit vectors \vec{c}_i we can introduce the occupation numbers $n_i(\vec{r})$ defined as the number of particles entering the site \vec{r} , at time t with a velocity pointing in direction \vec{c}_i .

With this notation, the CA rule governing the dynamics of our model reads

$$n_i(\vec{r} + \Delta_r \vec{c}_i, t + \Delta_t) = \sum_{\ell=0}^{2d-1} \mu_\ell(\vec{r}, t) n_{i+\ell}(\vec{r}, t), \quad (6.7)$$

where i is wrapped onto $\{1, 2, \dots, 2d\}$. The $\mu_\ell \in \{0, 1\}$ are Boolean variables which select only one of the $2d$ terms in the right-hand side. Therefore they must obey the condition

$$\sum_{\ell=0}^{2d-1} \mu_\ell = 1. \quad (6.8)$$

Practically, this condition can be enforced in a simulation by dividing the interval $[0, 1]$ into $2d$ bins of length p_ℓ , each assigned to one of the ν_ℓ . Then, at each lattice site and each time step, a real random number between 0 and 1 is computed (with a random number generator). The bin it falls into will determine which μ_ℓ is the one that will be non-zero. This rule is illustrated in Fig. 15 for the case of a two-dimensional system.

The macroscopic behavior resulting from microdynamics (6.7) in the limit of infinitely small lattice spacing Δ_r and time step Δ_t can be obtained with the same techniques as developed in Sec. 3, namely the multiscale Chapman–Enskog expansion [33]. Since the dynamics is linear, a more direct calculation is also possible if the limit is taken in such a way that Δ_r^2/Δ_t remains constant.

As expected, the result is that the quantity $\rho = \sum_{i=1}^{2d} \langle n_i \rangle$, where $\langle n_i \rangle$ is the average occupation number at site \vec{r} and time t obeys the diffusion equation [33]

$$\partial_t \rho + \text{div}[-D \text{grad} \rho] = 0,$$

where D is the diffusion constant whose expression, in a two-dimensional square lattice, is

$$D = \frac{\Delta_r^2}{\Delta_t} \left(\frac{1}{4(p+p_2)} - \frac{1}{4} \right) = \frac{\Delta_r^2}{\Delta_t} \left(\frac{p+p_0}{4[1-(p+p_0)]} \right). \quad (6.9)$$

For the one- and three-dimensional cases, a similar expression can be found [33].

6.3.2. Lattice Boltzmann diffusion rule

If, instead of Boolean variables, the diffusion process is described in terms of the probability of presence $f_i(\vec{r}, t)$ of a particle entering site \vec{r} at time t along direction i , the diffusion rule can be written down using the LB (lattice Boltzmann) formalism introduced in Sec. 4.

The evolution rule takes the form

$$f_i(\vec{r} + \Delta_t \vec{v}_i, t + \Delta_t) = \frac{1}{\tau} f_i^{(0)}(\vec{r}, t) + \left(1 - \frac{1}{\tau}\right) f_i(\vec{r}, t),$$

where $f_i^{(0)}$ is the local equilibrium distribution and τ the relaxation time. Since the only conserved quantity in a diffusive process is the particle number $\rho = \sum_{i=1}^{2d} f_i$, we choose

$$f_i^{(0)} = \frac{1}{2d} \rho$$

so that (i) ρ is indeed conserved and (ii) the local equilibrium depends on \vec{r} and t only through the conserved quantities.

Thus, the evolution rule can be rewritten as

$$f_i(\vec{r} + \Delta_t \vec{v}_i, t + \Delta_t) = \left[1 - \frac{1}{\tau} \left(1 - \frac{1}{2d} \right) \right] f_i(\vec{r}, t) + \sum_{j \neq i} \frac{1}{(2d\tau)} f_j(\vec{r}, t).$$

This is equivalent to the lattice Boltzmann equation associated with the diffusive CA having the probability of rotation

$$p_0 = 1 - \frac{1}{\tau} \left(1 - \frac{1}{2d} \right), \quad p_j = \frac{1}{2d}.$$

For a two-dimensional square lattice and according to Eq. (6.9), these values of p_i correspond to a diffusion constant

$$D = \frac{1}{2} \left(\tau - \frac{1}{2} \right) \frac{\Delta_r^2}{\Delta_t}.$$

From this, we conclude that $\tau \geq 1/2$, otherwise D becomes negative. However, from the expression for p_0 , we see also that $\tau \geq 1 - 1/(2d)$, if we want to interpret p_0 as a probability. Thus, in two dimensions, the situation $1/2 < \tau < 3/4$ does not correspond to a CA realization. Yet, the CA model can have $D = 0$ in a different way since it does not impose that all p_i 's are equal but p_0 . This also shows that the numerical behavior of the LB scheme must be checked in more detail when $1/2 < \tau < 3/4$. Finally, notice that a too large value of τ may yield an anisotropic behavior because it favors too much the lattice axis.

6.3.3. *LB diffusion in polar coordinates*

The models presented so far (whether hydrodynamical or diffusive) require a regular lattice to be defined properly. There is a clear interest to relax this limitation and allow “body-fitted” meshes that can be adapted to a given geometry of boundaries. This problem is still an active field of research [129, 166].

Here we simply present a way to define a LB model in polar coordinate, assuming that the system has an angular symmetry. Thus, the variables f_i depends only on the distance r to the center of the system. We shall also assume that the system is described by an underlying lattice dynamics, independent of the space discretization given by the polar coordinates.

We want to compute how many particles enter a polar cell located at distance r . Particles traveling toward larger values of r are described by the quantity $f_1(r, t)$, whereas particle moving to the center of the system are described by $f_2(r, t)$. Due to the angular symmetry, there is no need to consider other directions of motion.

In the case of a diffusive system, the population f_1 and f_2 are mixed according to $f'_1 = pf_1 + (1-p)f_2$ and $f'_2 = pf_2 + (1-p)f_1$.

The number of particles entering cell $r + dr$ in the positive direction are those exiting cell r after the diffusion step. The density of such particles is given by f'_1 . Since we work in polar coordinate, the cross section of cell r is σr^{d-1} , where σ is some constant and d the space dimensionality. Therefore, there are $\sigma r^{d-1} f'_1$ particles moving from cell r to cell $r + dr$. Since the cross section of cell $r + dr$ is $\sigma(r + dr)^{d-1}$, the density $f_1(r + dr, t + \Delta_t)$ is defined by the balance equation

$$\sigma(r + dr)^{d-1} f_1(r + dr, t + \Delta_t) = \sigma r f'_1.$$

A similar derivation hold for $f_2(r - dr, t + \Delta_t)$. Thus, for a diffusion process, we obtain

$$\begin{aligned} f_1(r + dr, t + \Delta_t) &= \left(\frac{r}{r + dr} \right)^{d-1} [p f_1 + (1 - p) f_2], \\ f_2(r - dr, t + \Delta_t) &= \left(\frac{r}{r - dr} \right)^{d-1} [p f_2 + (1 - p) f_1]. \end{aligned} \quad (6.10)$$

Therefore, the effect of the polar coordinate system is to modify the propagation scheme. It can be checked that numerical simulations of Eq. (6.10), with fixed boundary conditions at $r = r_0$ and $r = r_1$, converges to the corresponding solution of Laplace equation in polar coordinates.

6.3.4. The reaction rule

In this section we add a reaction term on top of the diffusion rule described in the previous section. Our aim is to simulate processes such as



where A , B and C are different chemical species, all diffusing in the same solvent, and K is the reaction constant. To account for this reaction, one can consider the following mechanism: at the “microscopic” level of the discrete lattice dynamics, all the three species are first governed by a diffusion rule. When an A and a B particle enter the same site at the same time, they disappear and form a C particle.

Of course, there are several ways to select the events that will produce a C when more than one A or one B are simultaneously present at a given site. Also, when C s already exist at this site, the exclusion principle may prevent the formation of new ones. A simple choice is to have A and B react only when they perform a head-on collision and when no C s are present in the perpendicular directions. Other rules can be considered if we want to enhance the reaction (make it more likely) or to deal with more complex situations ($2A + B \rightarrow C$, for instance).

A parameter k can be introduced to tune the reaction rate K by controlling the probability of a reaction taking place.

In order to write down the microdynamic equation of this process, we shall denote by $a_i(\vec{r}, t)$, $b_i(\vec{r}, t)$ and $c_i(\vec{r}, t) \in \{0, 1\}$ the presence or absence of a particle of type A , B or C , entering site \vec{r} at time t pointing in lattice direction i .

We shall assume that the reaction process first takes place. Then, the left-over particles, or the newly created ones, are randomly deflected according to the diffusion rule. Thus, using Eq. (6.7), we can write the reaction-diffusion microdynamics as (d is the dimensionality of the Cartesian lattice)

$$a_i(\vec{r} + \Delta_r \vec{e}_i, t + \Delta_t) = \sum_{\ell=0}^{2d-1} \mu_\ell(\vec{r}, t) [a_{i+\ell}(\vec{r}, t) + R_{i+\ell}^a(a, b, c)] \quad (6.12)$$

and similarly for the two other species B and C .

As before, the $\mu_\ell(\vec{r}, t)$ are independent random Boolean variables producing the direction shuffling. The lattice spacing Δ_r and time steps Δ_t are introduced as usual and the lattice directions \vec{e}_i are defined as east, north, west and south, in the case of a two-dimensional lattice.

The quantity $R_j^a(a, b, c)$ is the reaction term: it describes the creation or the annihilation of an A particle in the direction j , due to the presence of the other species. In the case of an annihilation process, the reaction term takes the value $R_j^a = -1$ so that $a_j - R_j^a = 0$. On the other hand, when a creation process takes place, $a_j = 0$ and $R_j^a = 1$. When no interaction occurs, $R_j^a = 0$.

For instance, in the case of the reaction (6.11) (illustrated in Fig. 52), the reaction terms could be written as

$$\begin{aligned} R_i^a &= -\kappa a_i b_{i+2} [\nu(1 - c_{i+1}) + (1 - \nu)(1 - c_{i-1})], \\ R_i^b &= R_{i+2}^a, \\ R_i^c &= \kappa(1 - c_i) [\nu a_{i-1} b_{i+1} + (1 - \nu) a_{i+1} b_{i-1}]. \end{aligned} \quad (6.13)$$

R_i^a and R_i^b are annihilation operators, whereas R_i^c corresponds to particle creation. One can easily check that, for each A (or B) particle which disappears, a C particle is created. That is,

$$\sum_{i=1}^{2d} R_i^a = \sum_{i=1}^{2d} R_i^b = - \sum_{i=1}^{2d} R_i^c.$$

The quantities $\nu(\vec{r}, t)$ and $\kappa(\vec{r}, t)$ in Eqs. (6.13) are independent random bits, introduced in order to select among the various possible events: $\nu(\vec{r}, t)$ is 1 with probability 1/2 and decides in which direction the reaction product C is created. When $\nu = 1$, the new C particle forms a $+90^\circ$ angle with respect to the old A particle. This angle is -90° when $\nu = 0$.

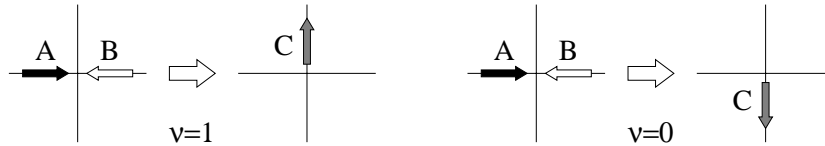


Fig. 52. Automata implementation of the $A + B \rightarrow C$ reaction process.

The occurrence of the reaction is subject to the value of the Boolean variable κ . With probability k , $\kappa = 1$. Changing the value of k is a way to adjust the reaction constant K . We shall see that k and K are proportional.

The presence of the terms involving c_i in the right-hand side of Eq. (6.13) may seem unphysical. Actually, these terms are introduced here in order to satisfy the exclusion principle: a new C cannot be created in direction i if c_i is already equal to 1. With this formulation, the reaction slows down as the number of C particles increases. At some point one may reach saturation if no more room is available to create new particles.

In practice, however, this should not be too much of a problem if one works at low concentrations. Also, quite often, the C species also undergoes a transformation: the reaction can be reversible or C particles can precipitate if the concentration reaches some threshold. Or, sometimes, one is only interested in the production rate $\sum_j R_j^a = \sum_j R_j^b$ of the species C and one can forget about them once they are created. In this case, one simply puts $c_i = 0$ in the first two Eq. (6.13).

Clearly, the exclusion principle may introduce some renormalization of the reaction rate. If for some reason, this is undesirable, multiparticle models offer an alternative to the LGA approach. This will be discussed in Sec. 7.

Due to the simple microscopic interpretation, Eq. (6.13) is easily generalized to other reaction processes. A common situation is when one species is kept at a fixed concentration. This means that the system is fed a chemical by an external mechanism. In this case, the corresponding occupation numbers (for instance the b_i s) can be replaced by random Boolean variables which are 1 with a probability given by the selected concentration of the species.

6.4. The macroscopic behavior

Here we establish the link between the discrete reaction-diffusion cellular automata dynamics and the corresponding macroscopic level of description. We shall perform this calculation for the case of three species A , B and C but a generalization to other reaction schemes is straightforward.

Our approach is similar to that used in Secs. 3 and 4. We use the Boltzmann molecular chaos assumption, in which correlations are neglected. Within this approximation, we shall see that the microdynamics of the $A + B \rightarrow 0$ reaction-diffusion processes yields the usual rate equation

$$\partial_t \rho_A = D \nabla^2 \rho_A - K \rho_A \rho_B. \quad (6.14)$$

To derive the macroscopic behavior of our automata rule, we first average Eq. (6.12)

$$\begin{aligned} & A_i(\vec{r} + \Delta_r \vec{e}_i, t + \Delta_t) - A_i(\vec{r}, t) \\ &= \sum_{j=1}^{2d} \Omega_{ij} A_j(\vec{r}, t) + \sum_{j=1}^{2d} (\delta_{ij} + \Omega_{ij}) R_j^a(A, B, C), \end{aligned} \quad (6.15)$$

102 *B. Chopard, et al.*

where $A_i = \langle a_i \rangle$ is the average value of the occupation numbers a_i . The matrix Ω is the matrix expressing the diffusion rule, that is

$$\Omega_{ii} = p_0 - 1, \quad \Omega_{ij} = p_{j-i},$$

where $j - i$ is defined modulo $2d$. Similar to equations to Eq. (6.15) hold for B_i and C_i .

Using the Boltzmann hypothesis, the average value of the reaction term is written as

$$\langle R_i^a(a, b, c, \kappa, \nu) \rangle \approx R_i^a(A, B, C, \langle \kappa \rangle, \langle \nu \rangle). \quad (6.16)$$

Note that this factorization may be wrong for simple annihilation reaction-diffusion processes, as discussed in Sec. 7.3.1.

The second step is to replace the finite difference in the left-hand side of Eq. (6.15) by its Taylor expansion

$$\begin{aligned} & A_i(\vec{r} + \Delta_r \vec{e}_i, t + \Delta_t) - A_i(\vec{r}, t) \\ &= \left[\Delta_t \partial_t + \frac{\Delta_t^2}{2} \partial_t^2 + \Delta_r (\vec{c}_i \cdot \partial_{\vec{r}}) + \frac{\Delta_r^2}{2} (c_i \cdot \partial_{\vec{r}})^2 + \Delta_t \Delta_r \partial_t (\vec{c}_i \cdot \partial_{\vec{r}}) \right] A_i \end{aligned} \quad (6.17)$$

and similarly for the other species B and C . As in the hydrodynamic case, we consider a Chapman–Enskog-like expansion and look for a solution of the following form

$$A_i = A_i^{(0)} + \epsilon A_i^{(1)} + \epsilon^2 A_i^{(2)} + \dots \quad (6.18)$$

Since particle motion is governed by the diffusion process, we will use the fact that when taking the continuous limit, the time and length scale are of the following order of magnitude

$$\Delta_r = \epsilon \Delta_{r1} \quad \text{and} \quad \Delta_t = \epsilon^2 \Delta_{t2}. \quad (6.19)$$

In reactive systems, as opposed to hydrodynamics or pure diffusion, neither momentum nor particle number are conserved in general. For instance, in the annihilation process $A + A \rightarrow \emptyset$, no conservation law holds.

On the other hand, the reaction term can be considered as a perturbation to the diffusion process, which makes derivation of the macroscopic limit rather simple. In Eq. (6.14), the reaction constant K has the dimension of the inverse of a time. This quantity defines at what speed the reaction occurs. At the level of the automaton, this reaction rate is controlled by the reaction probability $k = \langle \kappa \rangle$ introduced in the previous section.

When the continuous limit is taken, the automaton time step Δ_t goes to zero. Thus, the number of reactions per second will increase as Δ_t decreases, unless the reaction probability k also diminishes in the right ratio. In other words, to obtain a finite reaction constant K in the macroscopic limit, it is necessary to consider that

$k \propto \Delta_t$. Since Δ_t is of the order ϵ^2 in our Chapman–Enskog expansion, the reaction term R_i^a is also to be considered as an $O(\epsilon^2)$ contribution and we shall write

$$R_i^a = \epsilon^2 R_{2i}^a. \quad (6.20)$$

At the macroscopic level the physical quantities of interest are the particle densities of each species. Following the usual method, we define the density ρ_A of the A species as

$$\rho_A = \sum_{i=1}^{2d} A_i^{(0)}$$

with the condition

$$\sum_{i=1}^{2d} A_i^{(\ell)} = 0 \quad \text{if } \ell \geq 1.$$

Now we have to identify the different orders in ϵ which appear in Eq. (6.15), using the expressions (6.17), (6.18), (6.19) and (6.20). We obtain

$$O(\epsilon^0) : \quad \sum_j \Omega_{ij} A_i^{(0)} = 0, \quad (6.21)$$

$$O(\epsilon^1) : \quad \Delta_{r1} (\vec{e}_i \cdot \nabla) A_i^{(0)} = \sum_j \Omega_{ij} A_j^{(1)}. \quad (6.22)$$

These equations are exactly similar to those derived in the case of pure diffusion (see Ref. 33) and the result is that

$$A_i^{(0)} = \frac{\rho_A}{2d}$$

and

$$A_i^{(1)} = \frac{\Delta_{r1}}{2d} \frac{1}{V} e_{i\alpha} \partial_\alpha \rho_A,$$

where V is the eigenvalue of the diffusion matrix Ω for the eigenvector

$$E_\alpha = (e_{1,\alpha}; e_{2,\alpha}; \dots; e_{2d,\alpha}).$$

The equation for the density ρ_A is now obtained by summing over i equations (6.15), remembering that

$$\sum_i \Omega_{ij} = 0.$$

Collecting all the terms up to $O(\epsilon^2)$, we see that the orders $O(\epsilon^0)$ and $O(\epsilon)$ vanish and we are left with

$$\begin{aligned} & \epsilon^2 \Delta_{t2} \partial_t \sum_i A_i^{(0)} + \epsilon^2 \Delta_{r1} \sum_i (\vec{e}_i \cdot \nabla) A_i^{(1)} + \epsilon^2 \frac{\Delta_{r1}}{2} \sum_i (\vec{e}_i \cdot \nabla)^2 A_i^{(0)} \\ & = \epsilon^2 \sum_j R_{2j}^a (A^{(0)}, B^{(0)}, C^{(0)}). \end{aligned}$$

Using the definition of Δ_{t2} , Δ_{r1} , R_{2j}^a and performing the summations yields

$$\partial_t \rho_A = D \nabla^2 \rho_A + \frac{1}{\Delta_t} \sum_j R_j^a \left(\frac{\rho_A}{2d}, \frac{\rho_B}{2d}, \frac{\rho_C}{2d} \right), \quad (6.23)$$

where D is the same diffusion constant as would be obtained without the chemical reactions (see Sec. 6.3.1).

It is interesting to note that expression (6.23) has been obtained without knowing the explicit expression for the reaction terms R and independently of the number of species. Actually, from this derivation, we see that the reaction term enters in a very natural way in the macroscopic limit: we just have to replace the occupation numbers by $\rho/2d$, the random Boolean fields by their average values and sum up this result for all lattice directions.

For the case of the $A+B \rightarrow C$ process in two dimensions, with the reaction term given by Eq. (6.13), Eq. (6.23) shows that the macroscopic behavior is described by the rate equations

$$\begin{aligned} \partial_t \rho_A &= D_A \nabla^2 \rho_A - \frac{k}{4\Delta_t} \left(1 - \frac{\rho_C}{4} \right) \rho_A \rho_B, \\ \partial_t \rho_B &= D_B \nabla^2 \rho_B - \frac{k}{4\Delta_t} \left(1 - \frac{\rho_C}{4} \right) \rho_A \rho_B, \\ \partial_t \rho_C &= D_C \nabla^2 \rho_C + \frac{k}{4\Delta_t} \left(1 - \frac{\rho_C}{4} \right) \rho_A \rho_B, \end{aligned} \quad (6.24)$$

where, in principle a different diffusion constant can be chosen for each species. We also observe that the reaction constant K is related to the reaction probability k by

$$K = \frac{k}{4\Delta_t}.$$

As explained previously, the exclusion principle introduces a correction $(1 - \rho_c/4)$ which remains small as long as C is kept at a low concentration.

6.5. Liesegang patterns

In this section we shall study a more complex system in which reaction-diffusion will be accompanied by solidification and growth phenomena. This gives rise to nice and complex structures that can be naturally modeled and analyzed in the framework of the cellular automata approach.

These structures are known as Liesegang patterns, from the German chemist R. E. Liesegang who first discovered them at the end of the nineteenth century [81].

Liesegang patterns are produced by precipitation and aggregation in the wake of a moving reaction front. Typically, they are observed in a test tube containing a gel in which a chemical species B (for example AgNO_3) reacts with another species A

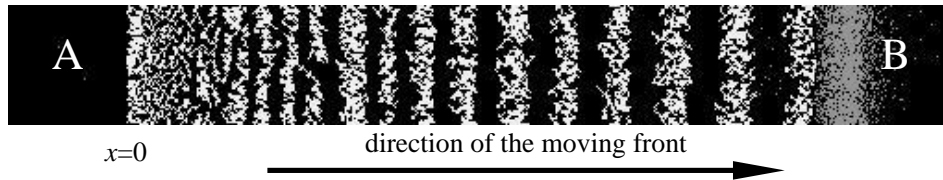


Fig. 53. Example of the formation of Liesegang bands in a cellular automata simulation. The white bands correspond to the precipitate which results from the $A + B$ reaction.

(for example HCl). At the beginning of the experiment, B is uniformly distributed in the gel with concentration b_0 . The other species A , with concentration a_0 is allowed to diffuse into the tube from its open extremity. Provided that the concentration a_0 is larger than b_0 , a reaction front propagates in the tube. As this $A + B$ reaction goes on, formation of consecutive bands of precipitate (AgCl in our example) is observed in the tube, as shown in Fig. 53. Although this figure is from a computer simulation, it is very close to the picture of a real experiment.

The presence of bands is clearly related to the geometry of the system. Other geometries lead to the formation of rings or spirals.

Depending on the experimental situation, some Liesegang patterns can present unexpected structures (inverse banding [120], effect of gravity, shape of the container and other exotic behaviors [100]). Therefore a complete analysis of the phenomena is difficult and still under investigation [3, 54].

On the other hand, for many different substances, generic formation laws can be identified. For instance, after a transient time, Liesegang bands appear at some positions x_i and times t_i and have a width w_i . It is first observed that the center position x_n of the n th band is related to the time t_n of its formation through the so-called *time law* $x_n \sim \sqrt{t_n}$.

Second, the ratio $p_n \equiv x_n/x_{n-1}$ of the positions of two consecutive bands approaches a constant value p for large enough n . This last property is known as the Jabczynski law [91] or the *spacing law*. Finally, the *width law* states that the width w_n of the the n th band is an increasing function of n . These features are related to the properties of the reaction front which move in the system. The time law appears to be a simple consequence of the diffusive dynamics. On the other hand, spacing and width laws cannot be derived with the reaction-diffusion hypotheses alone. Extra nucleation-aggregation mechanisms have to be introduced, which makes any analytical derivation quite intricate [140, 163, 192].

From an abstract point of view, the most successful mechanism that can be proposed to explain the formation of Liesegang patterns is certainly the supersaturation assumption based on Ostwald's ideas [132]. This mechanism can be understood using the formation scenario proposed by Dee [48]: the two species A and B react to produce a new species C (a colloid, in chemical terminology) which also diffuses in the gel.

When the local concentration of C reaches some threshold value, nucleation occurs: that is, spontaneously, the C particles precipitate and become solid D particles at rest. This process is described by the following equations

$$\begin{aligned}\partial_t a &= D_a \nabla^2 a - R_{ab}, \\ \partial_t b &= D_b \nabla^2 b - R_{ab}, \\ \partial_t c &= D_c \nabla^2 a + R_{ab} - n_c, \\ \partial_t d &= n_c,\end{aligned}\tag{6.25}$$

where, as usual, a , b , c , d stand for the concentration at time t and position \vec{r} of the A , B , C and D species, respectively. The term R_{ab} expresses the production of the C species due to the $A+B$ reaction. Classically, a mean-field approximation is used for this term and $R_{ab} = Kab$, where K is the reaction constant. The quantity n_c describes the depletion of the C species resulting from nucleation and aggregation on existing D clusters. An analytical expression for this quantity is rather complicated. However, at the level of a cellular automata model, this depletion term can be included quite naturally.

Within this framework, the supersaturation hypothesis can be stated as follows: due to aggregation, the clusters of nucleated D particles formed at the reaction front deplete their surroundings of the reaction product C . As a result, the level of supersaturation drops dramatically and the nucleation and solidification processes stop. To reach again suitable conditions to form new D nuclei, the $A-B$ reaction has to produce sufficient new C particles. But, the reaction front moves and this happens at some location further away. As a result, separate bands appear.

Most of the ingredients needed for modeling the formation of Liesegang pattern in terms of a CA approach have already been introduced in the previous section, when describing the $A+B \rightarrow C$ reaction-diffusion process. In the case of Dee's scenario, we also need to provide a mechanism for spontaneous nucleation (or precipitation) in order to model the transformation of a diffusing C particle into a solid D particle. Finally, aggregation of C particles on an existing D cluster will be modeled in very much the same spirit as the DLA growth described in Sec. 2.6. The key idea will be to introduce threshold values to control both of these processes.

The C particles, once created, diffuse until their local density (computed as the number of particles in a small neighborhood divided by its total number of sites and lattice directions), reaches a threshold value k_{sp} . Then they spontaneously precipitate and become D particles at rest (nucleation). Here, we typically consider 3×3 Moore neighborhoods centered around each lattice site.

Morover, C particles located in the vicinity of one or more precipitate D particles aggregate provided that their local density (computed as before) is larger than an aggregation threshold $k_p < k_{sp}$.

The parameters k_p and k_{sp} are two control parameters of the model. The introduction of these critical values refers to the qualitative models of solidification theory, relating supersaturation and growth behavior [82].

An important aspect of the mechanism of Liesegang patterns formation is the role of spontaneous fluctuations. Precipitation and aggregation processes (such as a DLA) are clearly dependent on local density fluctuations. For instance, even if the average particle concentration of C particles is less than the supersaturation threshold, it may be higher locally and give rise to spontaneous nucleation. Similarly, aggregation is a function of the particle density in the vicinity of an existing solid cluster, which is also a locally fluctuating quantity.

The cellular automata approach naturally accounts for these fluctuation phenomena and, in addition, captures the mesoscopic nature of the precipitate cluster, that can be fractal.

Figure 53 shows a typical example of a cellular automata simulation with C particles, giving rise to bands. The initial condition is built as follows: at time $t = 0$, the left part of the system ($x \leq 0$) is randomly occupied by A particles, with a density a_0 and the right part ($x > 0$) is filled with B particles with a density b_0 .

From the positions x_n and the formation time t_n of each band, we can verify the spacing and the time laws. For instance, the plot given in Fig. 54 shows very good agreement for the relation $x_n/x_{n-1} \rightarrow p$. It is found that the so-called Jablczynski coefficient p is 1.08, a value corresponding to experimental findings. The way the value of p depends on the parameters of the model is expected to follow the so-called Matalon–Pakter [119] experimental law. From a numerical and theoretical point of view, this dependence is still under investigation [3].

Liesegang patterns are found only if the parameters of the experiment are thoroughly adjusted. In our simulation, k_p and k_{sp} are among the natural quantities that control supersaturation and aggregation. In practice, however, one cannot directly modify these parameters. On the other hand, it is experimentally possible to change some properties of the gel (its pH for example) and thus influence the properties of the aggregation processes or the level of supersaturation.

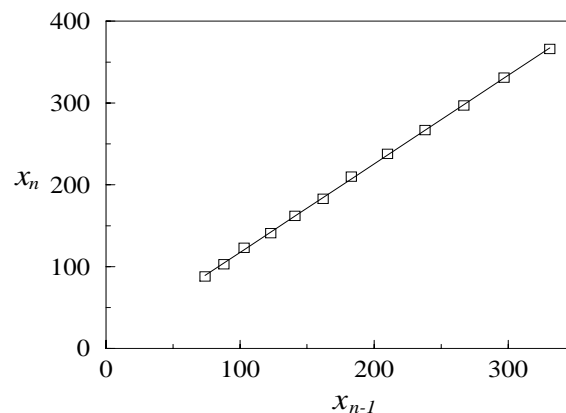


Fig. 54. Verification of the spacing law for the situation with C particles. The ratio x_n/x_{n-1} tends to $p = 1.08$.

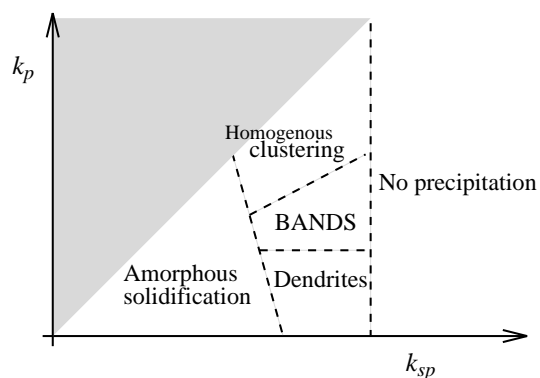


Fig. 55. Qualitative phase diagram showing the different possible patterns that can be obtained with our cellular automata model, as a function of the values of k_{sp} and k_p .

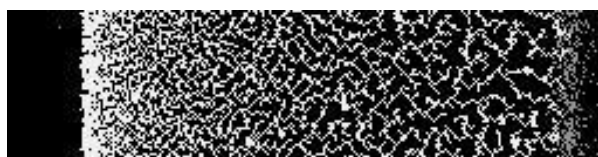
Outside of the region where Liesegang patterns are formed, our simulations show that, when k_p and k_{sp} vary, other types of patterns are obtained. These various patterns can be classified in a qualitative phase diagram, as shown in Fig. 55. An example of some of these “phases” is illustrated in Fig. 56. Note that the limits



(a)



(b)



(c)

Fig. 56. Examples of patterns that are described in the phase diagram: (a) corresponds to homogeneous clustering; this is also the case of pattern (b) but closer to the region of band formation. Pattern (c) shows an example of what we called a dendrite structure. Amorphous solidification would correspond to a completely uniform picture.

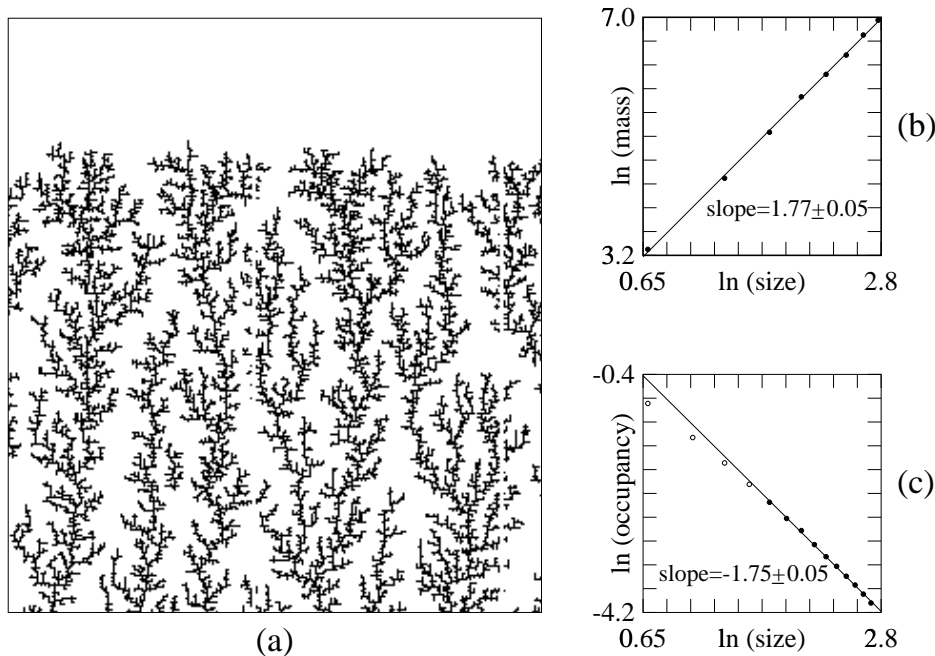


Fig. 57. (a) Examples of mineral dendrite obtained from a cellular automata simulation with $k_p = 0$; in this figure, the reaction front moves from upward. The two graphs on the right show the numerical measurement of the fractal dimension using: (b) a sand-box method and (c) a box-counting technique.

between the different “phases” do not correspond to any drastic modification of the patterns. There is rather a smooth crossover between the different domains. The associated names are borrowed from the phenomenological theory of solidification [82].

The terminology of dendrite comes from the tree-like structures that are sometimes found on the surfaces of limestone rocks or plates and that can be confused with fossils. The plant-shaped deposit is made of iron or manganese oxides that appear when at some point in the geological past the limestone was penetrated by a supersaturated solution of manganese or iron ions. It turns out that the formation of these mineral dendrites can be simulated by the same scenario as Liesegang patterns, but with an aggregation threshold $k_p = 0$. Figure 57 shows the results of such a modeling. The fractal dimension of these clusters is found to be around 1.77, a value which is very close to that measured in a real sample [37].

The patterns we have presented so far show axial symmetry, reflecting the properties of the experimental setup. But the same simulations can be repeated with different initial conditions. A case of interest is the situation of radial symmetry responsible for the formation of rings or spirals. The reactant A is injected in the central region of a two-dimensional gel initially filled with B particles. The

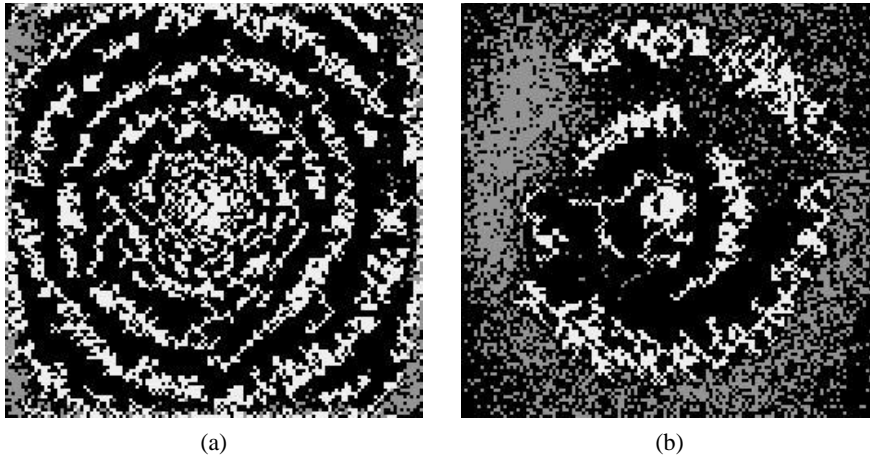


Fig. 58. Liesegang rings (a) and spiral (b), as obtained after 2000 iterations of the cellular automata model, with C particles indicated in gray.

result of the cellular automata simulation is shown in Fig. 58. In (a) concentric rings are formed, starting from the middle of the system and appearing as the reaction front radially moves away. In (b) a spiral-shaped structure is created. Although the two situations are similar as far as the simulation parameters are concerned, the appearance of a spiral stems from a spontaneous spatial fluctuation which breaks the radial symmetry.

Liesegang patterns are obtained when the initial A concentration is significantly larger than the initial B concentration. In a cellular automata model with an exclusion principle, a large concentration difference implies having very few B particles. As a consequence, the production rate of C particles is quite low because very few reactions take place. For this reason, the simulations presented above, have been produced with a pseudo-three-dimensional system composed of several two-dimensional layers. The reaction has been implemented so that particles of different layers can interact.

Therefore, pure CA simulations of Liesegang structure can be very demanding in terms of CPU time. It turns out that a LB approach is also possible, with much less computer resources, and makes it possible to investigate large systems exhibiting many more bands.

The LB model follows the same line as in the CA approach but some external noise is added to describe aggregation and nucleation as probabilistic processes. We refer the reader to Ref. 38 for a more detailed discussion. Below we just show some of the patterns generated with the LB model. Figure 59 shows an example of a lattice Boltzmann simulation containing up to 30 consecutive bands, in a system of sizes 1024×64 .

We can also consider again the case of Liesegang rings and spirals in the framework of the LB approach.

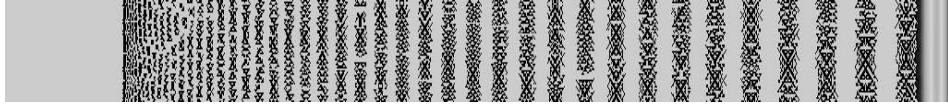


Fig. 59. Example of the formation of Liesegang bands in a lattice Boltzmann simulation.

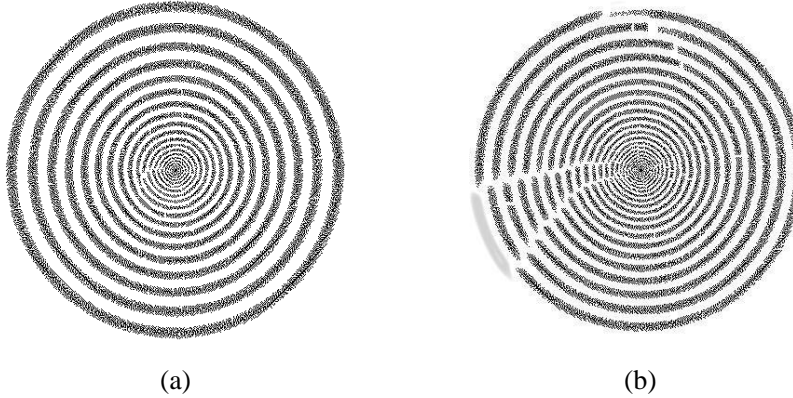


Fig. 60. Formation of (a) Liesegang rings and (b) spiral-shaped pattern, as obtained after 2000 iterations of the lattice Boltzmann model.

Figure 60(a) shows the situation where concentric rings of precipitate are formed. The numerical parameters are: $a_0 = 1$, $b_0/a_0 = 0.013$, $D_b/D_a = 0.1$, $k_{sp}/a_0 = 0.0087$, $k_p/a_0 = 0.0065$. The nucleation process takes place with a probability of 0.05 and aggregation with a probability close to 1. This pattern turns out to be quite similar to real Liesegang structures obtained in a similar experimental situation [81].

For the same set of parameters, but $b_0/a_0 = 0.016$, a different pattern is observed in Fig. 60(b). There, a local defect produced by a fluctuation develops and a spiral of precipitate appears instead of a set of rings. Such a spiral pattern will never be obtained from a deterministic model without a stochastic component.

7. Multiparticle Models

Multiparticle models (also termed Integer Lattice Gas Automata [14]) are lattice gas models without an exclusion principle. They are designed to conciliate the advantages of the CA and LB models. LB models are less noisy and provide more flexibility than their Boolean (CA) counterpart. However they may exhibit some bad numerical instabilities (that is the case of lattice BGK models of fluids) and they sometimes fail to account for relevant physical phenomena because fluctuations are neglected. An example is provided in Sec. 7.3.1 by the anomalous kinetics in the simple $A + A \rightarrow 0$ reaction-diffusion processes.

Multiparticle models conserve the point-like nature of particles, as in cellular automata, but allow an arbitrary number of them to be present at each lattice site. This eliminates the exclusion principle that plagues the cellular automata approach and which appears as a numerical artifact rather than a desirable physical property.

Mathematically speaking, this means that the state of each lattice site cannot be described with a finite number of information bits. However, in practice, it is easy to allocate a 32- or 64-bit computer word to each lattice site, to safely assume that “any” number of particles can be described at that site.

Multiparticle models lead to a reduced statistical noise: if the number of particles per site is N , the intrinsic fluctuations due to the discrete nature of the particles will typically be of the order \sqrt{N} . This is small compared to N , if N is large enough. Therefore, we do not have to perform much averaging to get a meaningful result.

In addition, with an arbitrary number of particle per site, we have much more freedom to enforce a given boundary condition, or tune a parameter of the simulation. Actually, when modeling a reaction process, it is often necessary to get rid of the exclusion principle. For instance, to describe processes such as $mA + nB \rightarrow C$, it is highly desirable to have more than four particles per site.

Unfortunately, the numerical implementation of multiparticle models is much more involved than LB or CA models and the computation time is also much higher. On the other hand, we restore in a natural way the fluctuations that are absent in LB simulations and provide an intrinsically stable numerical scheme (since we deal with positive integer numbers). Besides, when compared to CA, the extra computational time may well be compensated by the fact that less averaging is required.

In this section we first consider the case of a reaction-diffusion system and then we shall describe how a hydrodynamical model can be defined within the context of a multiparticle approach.

7.1. *Multiparticle diffusion model*

Our algorithm is defined on a d -dimensional Cartesian lattice of spacing Δ_r [36]. Each lattice site \vec{r} is occupied, at time t , by an arbitrary number of particles $n(\vec{r}, t)$. The discrete time diffusion process is defined as follows: during the time interval Δ_t , each particle can jump to one of its $2d$ nearest-neighbor sites along lattice direction i with probability p_i , or stay at rest with a probability $p_0 = 1 - \sum_{i=1}^{2d} p_i$.

An advantage of dealing with multiparticle dynamics is that advection mechanisms can be added to the diffusion process. When the probabilities of jumping to a nearest-neighbor site are different in each direction, a drift is introduced. This adds a density gradient term to the diffusion equation which then reads

$$\partial_t \rho = \vec{V} \nabla \rho + D \nabla^2 \rho,$$

where \vec{V} is the advection velocity. Such an advection effect is difficult to produce without an artifact when an exclusion principle holds.

For the sake of simplicity, we shall now consider a two-dimensional case. The generalization is straightforward and follows the same reasoning.

The idea is to loop over every particle at each site, decide where it goes and move it to its destination site. In terms of the particle numbers $n(\vec{r}, t)$, our multiparticle rule can be expressed as

$$\begin{aligned}
 n(\vec{r}, t + \Delta t) = & \sum_{\ell=1}^{n(\vec{r}, t)} p_{0\ell}(\vec{r}, t) + \sum_{\ell=1}^{n(\vec{r} + \Delta_r \vec{e}_3, t)} p_{1\ell}(\vec{r} + \Delta_r \vec{e}_3, t) \\
 & + \sum_{\ell=1}^{n(\vec{r} + \Delta_r \vec{e}_1, t)} p_{3\ell}(\vec{r} + \Delta_r \vec{e}_1, t) + \sum_{\ell=1}^{n(\vec{r} + \Delta_r \vec{e}_4, t)} p_{2\ell}(\vec{r} + \Delta_r \vec{e}_4, t) \\
 & + \sum_{i=1}^{n(\vec{r} + \Delta_r \vec{e}_2, t)} p_{4\ell}(\vec{r} + \Delta_r \vec{e}_2, t). \tag{7.1}
 \end{aligned}$$

The vectors $\vec{e}_1 = -\vec{e}_3$, $\vec{e}_2 = -\vec{e}_4$ are the four unit vectors along the main directions of the lattice. The stochastic Boolean variable $p_{i\ell}(\vec{r}, t)$ is 1 with probability p_i and selects whether or not particle ℓ chooses to move to site $\vec{r} + \Delta_r \vec{e}_i$. Since each particle has only one choice, we must have

$$p_{0\ell} + p_{1\ell} + p_{2\ell} + p_{3\ell} + p_{4\ell} = 1.$$

The macroscopic occupation number $N(\vec{r}, t) = \langle n(\vec{r}, t) \rangle$ is obtained by averaging the above evolution rule over an ensemble of equivalent systems. Clearly, one has

$$\left\langle \sum_{\ell=1}^{n(\vec{r}, t)} p_{i\ell}(\vec{r}, t) \right\rangle = p_i N(\vec{r}, t).$$

Thus, we obtain the following equation of motion:

$$\begin{aligned}
 N(\vec{r}, t + \Delta t) = & p_0 N(\vec{r}, t) + p_1 N(\vec{r} + \Delta_r \vec{e}_3, t) + p_3 N(\vec{r} + \Delta_r \vec{e}_1, t) \\
 & + p_2 N(\vec{r} + \Delta_r \vec{e}_4, t) + p_4 N(\vec{r} + \Delta_r \vec{e}_2, t). \tag{7.2}
 \end{aligned}$$

Assuming N varies slowly on the lattice, we can perform a Taylor expansion in both space and time to obtain the continuous limit. Using $\sum p_i = 1$ and $\vec{e}_i = -\vec{e}_{i=2}$, we obtain

$$\begin{aligned}
 \Delta_t \partial_t N(\vec{r}, t) + \frac{\Delta_t^2}{2} \partial_t^2 N(\vec{r}, t) + \mathcal{O}(\Delta_t^3) \\
 = \Delta_r [(p_3 - p_1) \vec{e}_1 + (p_4 - p_2) \vec{e}_2] \cdot \nabla N(\vec{r}, t) + \frac{\Delta_r^2}{2} (p_1 + p_3) (\vec{e}_1 \cdot \nabla)^2 N(\vec{r}, t) \\
 + \frac{\Delta_r^2}{2} (p_2 + p_4) (\vec{e}_1 \cdot \nabla)^2 N(\vec{r}, t) + \mathcal{O}(\Delta_r^3). \tag{7.3}
 \end{aligned}$$

Since, \vec{e}_1 and \vec{e}_2 are orthonormal, we have

$$(\vec{e}_1 \cdot \nabla)^2 + (\vec{e}_2 \cdot \nabla)^2 = \nabla^2.$$

In order to use this property it is necessary that $p_1 + p_3 = p_2 + p_4$, otherwise the lattice directions will “visible.” Thus we impose the isotropy condition

$$p_1 + p_3 = p_2 + p_4 = \frac{1 - p_0}{2}$$

and we obtain

$$\begin{aligned} \partial_t N(\vec{r}, t) + \frac{\Delta_t}{2} \partial_t^2 N(\vec{r}, t) + \mathcal{O}(\Delta_t^2) \\ = \vec{V} \cdot \nabla N(\vec{r}, t) + D \nabla^2 N(\vec{r}, t) + \mathcal{O}(\Delta_r^3), \end{aligned} \quad (7.4)$$

where \vec{V} is the advection velocity

$$\vec{V} = \frac{\Delta_r}{\Delta_t} [(p_3 - p_1)\vec{e}_1 + (p_4 - p_2)\vec{e}_2]$$

and D the diffusion constant

$$D = \frac{\Delta_r^2}{4\Delta_t} (1 - p_0). \quad (7.5)$$

We may now consider the limit $\Delta_r \rightarrow 0$ and $\Delta_t \rightarrow 0$ with $\Delta_r^2/\Delta_t \rightarrow \text{constant}$, as usual in a diffusion process. However, here, some additional care is needed. If $p_3 \neq p_1$ or $p_4 \neq p_2$, the advective term will diverge in the limit. This means that $p_3 - p_1$ or $p_4 - p_2$ must decrease proportionally to Δ_r when the limit is taken. Thus, with a halved lattice spacing, the difference between p_i and p_{i+2} must also be halved in order to produce the same advection. With these assumptions, we obtain, in the macroscopic limit

$$\partial_t N = \vec{V} \cdot \nabla N + D \nabla^2 N.$$

7.2. Numerical implementation

The main problem when implementing our algorithm on a computer (for instance, for the two-dimensional case we described in the previous section) is to find an efficient way to select the particles at rest and distribute randomly the others among the four possible directions of motion. More precisely, we have to compute quantities such as

$$n_i = \sum_{\ell=1}^{n(\vec{r}, t)} p_{i\ell}(\vec{r}, t).$$

In practice, we can loop over all ℓ particles at every site and, for each of them, choose a random number r , uniformly distributed in the interval $[0, 1]$. Then, we consider a division of this interval in subintervals $[r_j, r_{j+1}]$, $j = 0, \dots, 5$, so that $p_i = r_{i+1} - r_i$. We say that $p_{i\ell} = 1$ if and only if $r_{i+1} \leq r < r_i$. The quantities n_i are thus distributed according to a multinomial distribution.

This procedure is acceptable for small values of n but, otherwise, very time consuming. However, when n is large (more precisely when $np_i(1 - p_i) \gg 1$, the

statistical distributions of the n_i is expected to approach Gaussian distributions of mean np_i and variance $np_i(1-p_i)$. This Gaussian approximation allows us to be much more efficient because we no longer have to generate a random number for each particle at each site.

For simplicity, take the case $p_0 = p$ and $p_1 = p_2 = p_3 = p_4 = (1-p)/4$. The n_i 's can be approximated as follows: we draw a random number n_0 from a Gaussian distribution of mean np and variance $np(1-p)$ (for instance using the Box-Muller method [141]). This number is then rounded to the nearest integer.

Thus, in one operation, this procedure splits the population into two parts: n_0 particles that will stay motionless and $n - n_0$ that will move. In a second step, the $n - n_0$ moving particles are divided into two subsets according to a Gaussian distribution of mean $n_m/2$ and variance $n_m(1/2)(1/2)$. Splitting up each of these subsets one more time yields the number n_i of particles that will move in each of the four lattice directions.

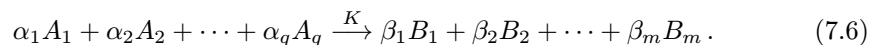
If advection is present, we can also proceed similarly. First, we divide up the moving particle population into two parts: on the one hand, those going to north and east, for instance, and on the other hand, those going south and west. Second, each subpopulation is, in turn, split into two subsets according to the values of the p_i s. Of course, as in traditional lattice gas automata, these splitting operations can be performed simultaneously (in parallel) at each lattice site.

Empirical considerations, supported by theoretical arguments on binomial distributions, show that $n_i = 40$ is a good threshold value in two dimensions, above which the Gaussian procedure can be used. Below this critical value, it is safer to have the algorithm loop over all particles. Note that in a given simulation, important differences in the particle number can be found from site to site and the two different algorithms may have to be used at different places.

7.3. The reaction algorithm

We will now discuss how reaction processes can be implemented in the framework of multiparticle models (see also Ref. 97). Reaction-diffusion phenomena can then be simulated by alternating the reaction process between the different species and then the diffusion of the resulting products, according to the multiparticle diffusion algorithm just described.

A reaction process couples locally the different species A_l , $l = 1, \dots, q$ to produce new species B_j , $j = 1, \dots, m$ according to the relation



The quantities α_l , β_j are the stoichiometric coefficients, and k is the reaction constant.

In order to model this reaction scheme with a multiparticle dynamics, one considers all the q -tuples that can be formed with α_1 particles of A_1 , α_2 particles of A_2 ,

etc. These q -tuples are transformed into m -tuples of B_j particles with probability k . At site \vec{r} and time t , there are

$$\mathcal{N}(\vec{r}, t) \equiv \binom{n_{A_1}}{\alpha_1} \binom{n_{A_2}}{\alpha_2} \cdots \binom{n_{A_q}}{\alpha_q}(\vec{r}, t)$$

ways to form these q -tuples, where $n_X(\vec{r}, t)$ denotes the number of particles of species X present at (\vec{r}, t) . If one of the $n_{A_i} < \alpha_i$ then obviously $\mathcal{N} = 0$.

These techniques offers a natural way to consider all possible reaction scenarios. For instance, in the case of the annihilation reaction $2A \rightarrow \emptyset$, suppose we have three particles (labeled a_1, a_2, a_3) available at a given lattice site. Then, there are three possible ways to form a reacting pair: (a_1, a_2) , (a_1, a_3) and (a_2, a_3) . In principle, all these combinations have the same chance of forming and reacting. However, if (a_1, a_2) react, then only a_3 is left and there is no point in considering (a_1, a_3) or (a_2, a_3) as possible candidates for reaction. Thus \mathcal{N} is the maximal number of possible events, but it is likely that the available particles are exhausted before reaching the end of this list of possible reactions.

The multiparticle reaction rule can therefore be summarized as follows:

- As long as there are enough particles left (i.e. at least α_l of species A_l , for each l), but no more than \mathcal{N} times, choose a Boolean random κ which is 1 with probability k .
- If $\kappa = 1$, remove from each species A_l a number α_l of particles ($n_{A_l} \rightarrow n_{A_l} - \alpha_l$) and add a number β_j of particles to each species B_j , $j = 1, \dots, m$ ($n_{B_j} \rightarrow n_{B_j} + \beta_j$).

This algorithm can easily be extended to a reversible reaction.

When k is very small, we may assume that all the \mathcal{N} q -tuples need to be considered and the above reaction rule can be expressed as

$$\begin{aligned} n_{A_l}(\vec{r}, t + \Delta t) &= n_{A_l}(\vec{r}, t) - \alpha_l \sum_{h=1}^{\mathcal{N}(\vec{r}, t)} \kappa_h, \\ n_{B_j}(\vec{r}, t + \Delta t) &= n_{B_j}(\vec{r}, t) + \beta_j \sum_{h=1}^{\mathcal{N}(\vec{r}, t)} \kappa_h, \end{aligned} \quad (7.7)$$

where κ_h is 1 with probability k .

This algorithm may become quite slow in terms of computer time if the n_X are large and $k \ll 1$. In this case, the Gaussian approximation described in the previous section can be used to speed up the numerical simulations: the number of accepted reactions can be computed from a local Gaussian distribution of mean $k\mathcal{N}(\vec{r}, t)$ and variance $k(1-k)\mathcal{N}(\vec{r}, t)$.

7.3.1. Diffusive annihilation

In order to check that our multiparticle reaction rule captures the true nature of fluctuation and correlation, we simulated the $A + A \rightarrow \emptyset$ reaction-diffusion process,

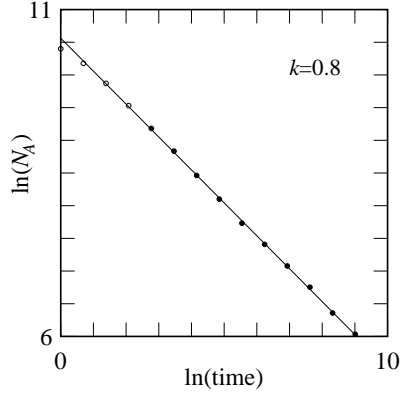


Fig. 61. Time decay of N_A , the total number of A particles in the $A + A \rightarrow \emptyset$ reaction-diffusion process, with the multiparticle method. A non-mean-field power law $t^{-d/2}$ is observed, in agreement with theoretical arguments.

where the A particle is uniformly distributed in the system. This reaction exhibits a non-mean-field decay law in one-dimensional systems [45]: the time evolution of $N_A(t)$ (the number of A particle left in the system at time t) departs from the behavior predicted by the rate equation $\partial_t N_A(t) = -K N_A^2(t)$, whose solution is $N_A(t) \sim t^{-1}$, for large t .

Figure 61 gives the behavior of a simulation performed on a line of 64 536 sites, with an initial number of about 100 particles per site. Diffusion and reaction processes are simulated with our multiparticle algorithms with a probability 1/2 that each particle moves left or right and a reaction probability $k = 0.8$. We observe that the total number of A particles decreases with time as the power law $N_A(t) \sim t^{-1/2}$, which is the correct result in $d = 1$ dimension.

7.3.2. Rate equation approximation

In a mean-field approximation, i.e. when the multipoint correlation functions are factorized as a product of one-point functions and the reaction probability k is much smaller than 1, our multiparticle dynamics gives the expected rate equation given by the mass action law. We define N_{A_i} and N_{B_j} as the average particle numbers per site of species A_i and B_j , respectively.

For the reaction process (7.6), it is possible to show that our multiparticle reaction algorithm yields (in the limit of a large lattice)

$$N_{A_i}(t + \Delta t) - N_{A_i}(t) = -K N_{A_1}^{\alpha_1} N_{A_2}^{\alpha_2} \cdots N_{A_q}^{\alpha_q},$$

$$N_{B_j}(t + \Delta t) - N_{B_j}(t) = K N_{A_1}^{\alpha_1} N_{A_2}^{\alpha_2} \cdots \bar{n}_{A_q}^{\alpha_q},$$

where K is the reaction constant whose expression is

$$K = \frac{k}{\alpha_1! \alpha_2! \cdots \alpha_q!}.$$

This calculation is based on combinatorial arguments and the equiprobability of all configurations with the same number of particles. More details can be found in Ref. 33, 36.

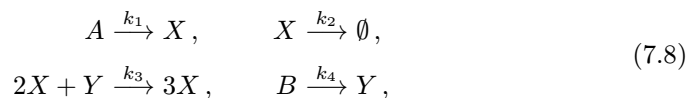
In the limit $\Delta_t \rightarrow 0$, we obtain the usual form of the rate equations for the reaction process under study, namely

$$\begin{aligned}\partial_t N_{A_i}(t) &= -\frac{K}{\Delta_t} N_{A_1}^{\alpha_1} N_{A_2}^{\alpha_2} \dots N_{A_q}^{\alpha_q}, \\ \partial_t N_{B_j}(t) &= \frac{K}{\Delta_t} N_{A_1}^{\alpha_1} N_{A_2}^{\alpha_2} \dots N_{A_q}^{\alpha_q}.\end{aligned}$$

7.4. Turing patterns

In this section, we use our multiparticle reaction-diffusion model to simulate the formation of the so-called Turing structures. Turing [173] was the first to suggest that, under certain conditions, chemicals can react and diffuse so as to produce steady-state heterogeneous spatial patterns of chemical or concentrations [17]. Turing structures are believed to play an important role in biological pattern formation processes, such as the stripes observed on the zebra skin [124]. In contrast to most hydrodynamical instabilities, the structure of Turing patterns is not related to any imposed macroscopic length scales (like the size of the container). Turing patterns exhibit regular structure with an intrinsic wavelength depending on the diffusion constants and reaction rates. Typical examples of inhomogeneous stationary states observed in experiments have a hexagonal or a striped structure [55].

For the sake of simplicity, we consider here only one of the simplest models showing Turing patterns: the Schnackenberg reaction-diffusion model [157] in two dimensions. It describes the following autocatalytic reaction:



where the densities of the species A and B are kept fixed (for instance by external feeding of the system). This situation of having a fixed concentration of some chemical is quite common in reaction-diffusion processes. As a result, there is no need to include all the dynamics of such reagents in cellular automata or multiparticle models. It is usually enough to create randomly a local population of these particles at each lattice site.

Here we consider a two-dimensional multispecies, multiparticle model with alternating reaction and diffusion steps. Instead of varying p_0 in Eq. (7.5), the diffusion coefficient is adjusted by performing ℓ consecutive diffusion steps for a given species. This technique amounts to introducing a different time step $\Delta_{t_m} = \Delta_t/\ell$ for this species and yields $D = \ell\Delta_r^2/4\Delta_t$.

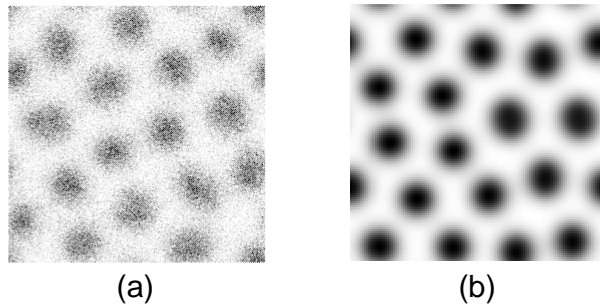


Fig. 62. Turing patterns obtained in the Schnackenberg reaction in the long time regime. (a) Multiparticle model and (b) mean-field rate equations.

The instability of the homogeneous state leading to Turing structures can be understood using the corresponding macroscopic rate equations [124] for the local average densities x and y

$$\begin{aligned}\partial_t x &= k_1 a - k_2 x + k_3 x^2 y + D_x \nabla^2 x, \\ \partial_t y &= k_4 b - k_3 x^2 y + D_y \nabla^2 y,\end{aligned}\tag{7.9}$$

where a and b represent the densities of particles A and B , respectively. A conventional analysis shows that for some values of the parameters, a homogeneous stationary state is unstable towards local density perturbations. Inhomogeneous patterns can evolve by diffusion-driven instabilities providing that the diffusion constants D_x and D_y are not the same. The region of the parameter space (a , b , $D_y/D_x, \dots$) for which homogeneous states of the system are unstable is called the deterministic Turing space.

Figure 62 shows the configuration obtained in the long time regime with our multiparticle model and the corresponding rate equations (7.9). In both cases, a hexagonal geometry is selected. The right panel corresponds to the solution of the rate equations, while the left panel corresponds to the multiparticle simulation. As we can see, the two pictures are quite similar. Although, it is not clear that the multiparticle (which brings fluctuations into play) adds anything compared with the predictions of the mean-field rate equations (which use less computer time) there are some indications [34] that the Turing space may be enlarged when fluctuations are considered.

7.5. A multiparticle fluid

In this section we show a the multiparticle method can also be used to model a hydrodynamic behavior. The key problem is to build the appropriate collision rule. Defining a collision between an arbitrary number of particles which conserve mass and momentum is not an easy task: particles are indivisible and fractions of them cannot be distributed among the lattice directions to satisfy the conservation laws. Furthermore, it is not possible to pre-compute all possible collisions (as we

do in a cellular automaton) because there are an infinite number of configurations. Thus, more sophisticated algorithms should be devised which may slow down the computation of the collision output.

We also would like to define a model in which the viscosity is an adjustable parameter. The approach we propose here is to develop a collision procedure which, on average, obeys the lattice BGK equation for hydrodynamics (see Sec. 4). Thus, we write the evolution rule as

$$f_i(\vec{r} + \Delta_t \vec{v}_i, t + \Delta_t) = f_i(\vec{r}, t) + \mathcal{F}_i(f(\vec{r}, t)),$$

where f_i are integer variable ($f_i \in \{0, 1, 2, \dots, \infty\}$) describing the number of particles entering site \vec{r} at time t with velocity \vec{v}_i . The quantity \mathcal{F}_i is the collision term. As usual, the particle density ρ and velocity field \vec{u} are defined as

$$\rho(\vec{r}, t) = \sum_i f_i(\vec{r}, t), \quad \rho \vec{u}(\vec{r}, t) = \sum_i f_i(\vec{r}, t) \vec{v}_i,$$

where index i runs over the lattice directions.

We now assume that the main effect of the interaction is to restore the local equilibrium distribution (4.7) obtained in the LB formalism

$$f_i^{(0)} = a\rho + \frac{b}{v^2} \rho \vec{v}_i \cdot \vec{u} + \rho e \frac{u^2}{v^2} + \rho \frac{h}{v^4} v_{i\alpha} v_{i\beta} u_\alpha u_\beta. \quad (7.10)$$

Note that f_i is an integer whereas $f_i^{(0)}$ is a real number. The parameters a , b , e and h should be determined according to the geometry of the lattice, with the condition that the Navier–Stokes equation describes the dynamics of the system, and that $\rho(\vec{r}, t) = \sum_i f_i^{(0)}(\vec{r}, t)$ and $\rho \vec{u}(\vec{r}, t) = \sum_i f_i^{(0)}(\vec{r}, t) \vec{v}_i$.

We shall require that, as in the BGK situation, the relaxation to the local equilibrium is governed by a parameter τ . Thus, the number of particles f'_i leaving (after collision) a given site along direction i is

$$f'_i = f_i + \frac{1}{\tau} [f_i^{(0)} - f_i] + \Delta f_i, \quad (7.11)$$

where Δf_i is a random quantity accounting for the fact that (after collision) the actual particle distribution may depart from its ideal value.

In practice f'_i is obtained as follows. Let $N = \sum_i f_i$ be the total number of particles at the given site. We assign to each direction i a weight w_i computed as

$$w_i = \max \left(0, \frac{1}{\tau} f_i^{(0)} + \left(1 - \frac{1}{\tau} \right) f_i \right).$$

From these weights, we define p_i , the probability for a particle to leave the site along direction i , as $p_i = w_i/M$, where $M = \sum_i w_i$ is a normalization constant.

To compute the collision output, we run through each of the N particles and place them in direction i with probability p_i . This gives us a temporary particle distribution \tilde{f}_i which then must be corrected to obtain f'_i , in order to ensure exact momentum conservation.

In our algorithm, \tilde{f}_i is computed as

$$\tilde{f}_i = \sum_{h=1}^N (s_{i-1} \leq r_h < s_i), \quad (7.12)$$

where $(s_{i-1} \leq r_h < s_i)$ is to be taken as a Boolean value which is 1 when the condition is true and zero otherwise. The quantities s_i are defined by $s_i = \sum_{j=1}^i p_j$, $s_0 = 0$ and r_h is a random variable uniformly distributed in $[0, 1]$. It is then easy to check that $(s_{i-1} \leq r_h < s_i) = 1$ with probability p_i .

Therefore, the expectation of \tilde{f}_i is $\langle \tilde{f}_i \rangle = \sum_{h=1}^N p_i$. If none of the p_i is zero, we have $M = N$ and

$$\langle \tilde{f}_i \rangle = \frac{1}{\tau} f_i^{(0)} + \left(1 - \frac{1}{\tau}\right) f_i. \quad (7.13)$$

Note that when N is large enough, Eq. (7.12) can be computed using a Gaussian approximation, as explained for the reaction-diffusion multiparticle model.

While the distribution \tilde{f}_i of outgoing particles obviously conserves the number of particles, Eq. (7.13) shows that it does only conserve momentum on average and some particles must be redirected to ensure exact conservation. The momentum tuning is performed iteratively, according to the following steps

- At each site where momentum is not correctly given by $\sum_j \tilde{f}_j \vec{v}_j$, choose at random one lattice direction i .
- If $\tilde{f}_i \neq 0$ move one particle randomly to an adjacent direction.
- Accept the change if it does not increase the momentum error. It is important to accept modifications which do not improve the error because it may happen that only a two-particle redirection decreases the error.
- Iterate this procedure until the outgoing particle distribution satisfies momentum conservation $\sum_j f'_j \vec{v}_j = \sum_j f_j \vec{v}_j$.

From the way the particles are distributed, we expect that roughly \sqrt{N} of them are misplaced. This gives an estimate of the number of iteration necessary to re-adjust the particle directions.

According to the above discussion, the quantity Δf_i defined in equation (7.11) vanishes on average. This fact is confirmed numerically. Consequently, we write

$$\langle f_i(\vec{r} + \Delta_t \vec{v}_i, t + \Delta_t) \rangle = \frac{1}{\tau} f_i^{(0)}(\vec{r}, t) + \left(1 - \frac{1}{\tau}\right) f_i(\vec{r}, t),$$

where we have used that $f_i(\vec{r} + \Delta_t \vec{v}_i, t + \Delta_t) = f'_i(\vec{r}, t)$, due to the definition of particle motion.

In the limit where the correlations between the f_i 's can be neglected (remember that $f_i^{(0)}$ is a non-linear function of all f_j 's) we may take the average of the above equation and we obtain

$$\langle f_i(\vec{r} + \Delta_t \vec{v}_i, t + \Delta_t) \rangle = \frac{1}{\tau} f_i^{(0)}(\langle \rho \rangle, \langle \rho \vec{u} \rangle) + \left(1 - \frac{1}{\tau}\right) \langle f_i \rangle. \quad (7.14)$$

Equation (7.14) is identical to the usual BGK microdynamics (see Sec. 4), except that now it approximates a multiparticle dynamics in which f_i are integer quantities. Therefore, the standard multiscale Chapman–Enskog expansion [33] can be applied exactly as in the BGK case and the same hydrodynamical behavior emerges: Eq. (7.14) is equivalent to the Navier–Stokes equation with viscosity $\nu = \Delta_t v^2 (C_4/C_2)(\tau - 1/2)$, where C_2 and C_4 are model dependent (different in hexagonal, square or cubic lattices and are defined in Eqs. (4.5) and (4.6)).

The present multiparticle scheme is intrinsically stable. No small fluctuation will be amplified unphysically to make the arithmetic blow up as happens with the LB model when ν becomes too small. Any value of the relaxation parameter τ can be considered without numerical problems but the physical limit of our model when $\tau \rightarrow 1/2$ (or $\tau < 1/2$) has not yet been explored.

We now present some applications of our multiparticle fluid, on a two-dimensional hexagonal lattice and with a population of rest particles. Figure 63 shows the measured velocity profile in a simulation of a Poiseuille flow [171]. Fluid particles are injected on the left side of a channel of length L and width W with a rightward velocity. On the upper and lower channel limits, the usual no-slip condition is imposed, by bouncing back incoming particles in order to produce a zero speed flow at the boundary. We observe a parabolic velocity profile in agreement with the prediction of hydrodynamics.

As a second example, we consider the ballistic annihilation problem $A + A \rightarrow 0$, where particles A evolve according to our multiparticle fluid rule. This is a variant of the diffusive annihilation problem discussed in Sec. 7.3.1: here a hydrodynamic behavior is imposed to the particle instead of a diffusive motion.

When two particles meet at the same site with opposite velocities, they annihilate each other. Thus, before the hydrodynamic collision takes place, our multiparticle dynamics is supplemented by a reaction term which modifies the particle

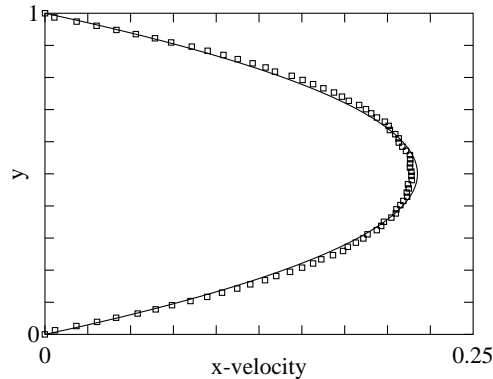


Fig. 63. Velocity profile in a multiparticle Poiseuille flow. The plot shows the horizontal average velocity $\langle u_x(y) \rangle$ as a function of y the vertical position between the upper and lower boundaries. The solid line corresponds to the best parabola fitting the data.

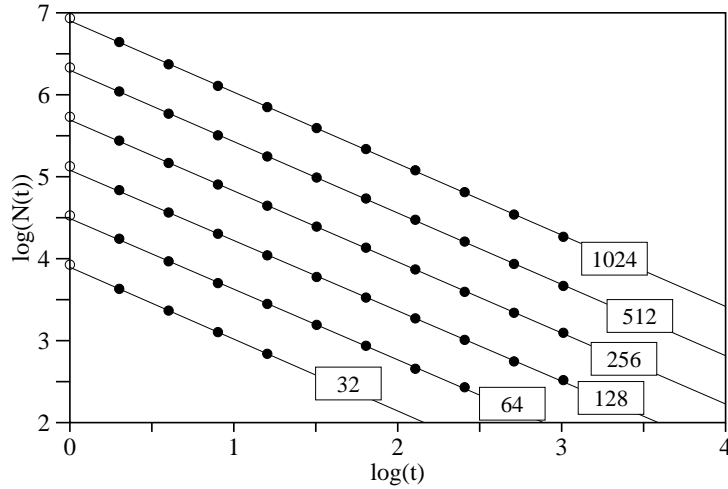


Fig. 64. Decay laws for the ballistic annihilation simulations, using the multiparticle lattice gas model. The various plots correspond to the lattice sizes indicated in the box. The decay exponent x is given by the slopes of the lines which are all within $x = 0.875 \pm 0.005$, except for the smallest lattice.

distributions f_i as $f_i \rightarrow \max(0, f_i - f_{i'})$, where i and i' correspond to opposite velocities ($\vec{v}_i = -\vec{v}_{i'}$). We are interested to measure the number $N(t)$ of A particles left in the system as time goes on. It is known [8, 60, 148, 149] that this quantity obeys a power law $N(t) \sim t^{-x}$. Molecular dynamics simulations [172] predict an exponent x between 0.86 and 0.89 depending on the size of the sample, in a two-dimensional system.

The simulation performed with the multiparticle model fully agrees with this prediction since an exponent $x = 0.87 \pm 0.005$ is found [42]. The simulation time required to obtain this value is several orders of magnitude shorter than a full molecular dynamics computation. The results for the decay law are summarized in Fig. 64.

The decay exponent x depends on the space dimension, as well as the velocity distribution [148, 149]. For one-dimensional systems with particles of velocity $\pm v$, it is found that $x = 1/2$. In two dimensions, the molecular dynamics simulations [172] indicate that the velocity distribution tends to Maxwellian, in the long time regime. It is then interesting to note that our multiparticle model imposes from the very beginning a discrete, truncated Maxwellian velocity distribution (Eq. (7.10)).

8. Wave Model and Fracture Simulation

In the previous sections, the LB approach has been applied to hydrodynamic systems and reaction diffusion processes. Here we show that it can also be used to define a wave dynamics. This section will present the basic aspect of the model, as well as some of its applications.

8.1. The wave model

Wave phenomena, whether mechanical or electromagnetic derives from two conserved quantities Ψ and \vec{J} , together with time reversal invariance and a linear response of the media. The quantity Ψ is a scalar field and \vec{J} its associated current. For sound waves, Ψ and \vec{J} are respectively the density and the momentum variations. In electrodynamics, Ψ is the energy density and \vec{J} the Poynting vector [92].

The idea behind the LB approach is to “generalize” a physical process to a discrete space and time universe, so that it can be efficiently simulated on a (parallel) computer. For waves, this generalization is obtained by keeping the essential ingredients of the real phenomenon, namely conservation of Ψ and \vec{J} , linearity and time reversal invariance. Thus, in a discrete space-time universe, a generic system leading to wave propagation is obtained from the lattice BGK equation

$$f_i(\vec{r} + \Delta_t \vec{v}_i, t + \Delta_t) - f_i(\vec{r}, t) = \frac{1}{\tau} (f_i^{(0)}(\vec{r}, t) - f_i(\vec{r}, t)) \quad (8.1)$$

by an appropriate choice of the local equilibrium distribution

$$f_i^{(0)} = a\Psi + b \frac{\vec{v}_i \cdot \vec{J}}{v^2} \quad \text{if } i \neq 0, \quad \text{and} \quad f_0^{(0)} = a_0\Psi, \quad (8.2)$$

where v is the ratio of the lattice spacing Δ_r to the time step Δ_t , and Ψ and \vec{J} are related to the f_i s in the standard way: $\Psi = \sum_i m_i f_i$ and $\vec{J} = \sum_i m_i f_i \vec{v}_i$. The quantities m_i are the weights associated to each lattice directions and whose value depends on the chosen lattice (here $m_0 = 1$ whatever the lattice is). Note that, here, we make no restriction on the sign of the f_i s which may well be negative in order to represent a wave.

As opposed to hydrodynamics [144], $f_i^{(0)}$ is a linear function of the conserved quantities, which ensures the superposition principle. The parameters a , b and a_0 are computed so that $\Psi = \sum_i m_i f_i^{(0)}$ and $\vec{J} = \sum_i m_i \vec{v}_i f_i^{(0)}$, which ensures conservation of Ψ and \vec{J} .

Following the same derivation as in Sec. 4, we obtain

$$a_0 + aC_0 = 1, \quad b = \frac{1}{C_2},$$

where $C_0 = \sum_{i \geq 1} m_i$ and $\sum_{i \geq 1} m_i v_{i\alpha} v_{i\beta} = C_2 v^2 \delta_{\alpha\beta}$. For the two-dimensional square lattice with rest particle (D2Q5), $m_i = 1$, $C_0 = 4$ and $C_2 = 2$.

Writing the momentum tensor $\Pi_{\alpha\beta}^{(0)} = \sum_i m_i v_{i\alpha} v_{i\beta} f_i^{(0)}$ as $\Pi_{\alpha\beta}^{(0)} = c_s^2 \Psi \delta_{\alpha\beta}$, we obtain

$$a = \frac{c_s^2}{v^2 C_2}, \quad a_0 = 1 - \frac{c_s^2}{v^2} \frac{C_0}{C_2},$$

where c_s is a free parameter giving the wave propagation speed. This parameter can be adjusted locally to model a medium with different refraction indices.

We can now compute the macroscopic behavior of Ψ and \vec{J} , using the procedure of Sec. 4. The main difference is that here, we do not have to neglect the higher

order in \vec{J} , since the dynamics is defined as linear. A straightforward calculations gives

$$\partial_t \Psi + \partial_\beta J_\beta = 0, \quad (8.3)$$

$$\partial_t J_\alpha + c_s^2 \partial_\alpha \Psi + \left(\tau - \frac{1}{2} \right) \left[\Delta_t c_s^2 \partial_\alpha \operatorname{div} \vec{J} - \frac{\Delta_t}{C_2 v^2} T_{\alpha\beta\gamma\delta} \partial_\beta \partial_\gamma J_\delta \right] = 0, \quad (8.4)$$

where $T_{\alpha\beta\gamma\delta} = \sum_i v_{i\alpha} v_{i\beta} v_{i\gamma} v_{i\delta}$. Depending on the lattice, this fourth order tensor may not be isotropic. This is precisely the case of the D2Q5 lattice which is known for giving anisotropic contributions to the hydrodynamic equations. However, this term vanishes when $\tau = 1/2$. This is interesting since the condition $\tau = 1/2$ is required to ensure time reversal invariance, as can be easily checked from Eq. (8.1) with $\vec{J} \rightarrow -\vec{J}$ and $\Psi \rightarrow \Psi$ in relation (8.2).

Equations (8.3) and (8.4) can be combined (space derivative of the second substituted in time derivative of the first). This yields

$$\partial_t^2 \Psi - c_s^2 \nabla^2 \Psi = \left(\tau - \frac{1}{2} \right) \left[\Delta_t c_s^2 \partial_\alpha \operatorname{div} \vec{J} - \frac{\Delta_t}{C_2 v^2} T_{\alpha\beta\gamma\delta} \partial_\beta \partial_\gamma J_\delta \right].$$

With $\tau = 1/2$, we recover the wave equation

$$\partial_t^2 \Psi - c_s^2 \nabla^2 \Psi = 0. \quad (8.5)$$

In hydrodynamic models, $\tau = 1/2$ corresponds to the limit of zero viscosity (see Sec. 4), which is numerically unstable. In our case, this instability does not show up provided we use an appropriate lattice. In the D2Q5 lattice, our dynamics is also unitary [108] which ensures that $\sum_i f_i^2$ is conserved. This extra condition prevents the f_i s from becoming arbitrarily large (with positive and negative signs, since Ψ is conserved). This is no longer the case with the D2Q9 lattice, where numerical instabilities develop for this wave dynamics.

Note that dissipation can be included in our microdynamics. Using $\tau > 1/2$ allows us to describe waves with viscous-like dissipation. This makes sense with the hexagonal lattice D2Q7, where no stability problem occurs when $\tau = 1/2$ and no anisotropy problem appears when the viscosity is non-zero ($\tau > 1/2$).

There is another (and simpler) way to include dissipation in this model, which is suitable for the D2Q5 lattice and appropriate to our purpose of modeling fracture propagation (see Sec. 8.4): absorption on non-perfect transmitter sites can be obtained by modifying the conservation of Ψ to $\sum_i m_i f_i^{(0)} = \mu \Psi$, where $0 \leq \mu \leq 1$ is an attenuation factor. In this way, $\mu = 0$ corresponds to perfect reflection (see Eq. (8.7)), $\mu = 1$ to perfect transmission and $0 < \mu < 1$ describes a situation where the wave is partially absorbed.

In Eq. (8.5), the propagation speed is given by $c_s^2 = av^2 C_2$. For the stability of the numerical scheme we must impose that $a_0 \geq 0$. This yields the larger possible value of a and, thus, the maximum propagation speed of the model is

$$c_{\max}^2 = \frac{C_2}{C_0} v^2$$

126 *B. Chopard, et al.*

(note that v is the speed at which information travels). We define the refraction index n (which may depends on the position) as

$$n(\vec{r}) = \frac{c_{\max}}{c_s(\vec{r})}, \quad n \geq 1.$$

From these results, we may rewrite a and a_0 as

$$a = \frac{1}{C_0 n^2}, \quad a_0 = 1 - \frac{1}{n^2}$$

and Eq. (8.1) reads

$$\begin{aligned} f_i(\vec{r} + \Delta_t \vec{v}_i, t + \Delta_t) &= \frac{\mu}{\tau} \frac{1}{C_0 n^2} \Psi + \frac{1}{\tau C_2 v^2} \sum_j \vec{v}_i \cdot \vec{v}_j m_j f_j - \left(\frac{1}{\tau} - 1 \right) f_i(\vec{r}, t), \\ f_0(\vec{r}, t + \Delta_t) &= \frac{\mu}{\tau} \frac{(n^2 - 1)}{n^2} \Psi - \left(\frac{1}{\tau} - 1 \right) f_0(\vec{r}, t), \end{aligned} \quad (8.6)$$

where μ is the dissipation factor.

For $\tau = 1/2$ and a d -dimensional Cartesian lattice, we have $m_i = 1$, $C_2 = 2$, $C_0 = 2d$ and the above equations reduce to

$$\begin{aligned} f_i(\vec{r} + \Delta_t \vec{v}_i, t + \Delta_t) &= \frac{\mu}{dn^2} \Psi - f_{i'}(\vec{r}, t), \\ f_0(\vec{r}, t + \Delta_t) &= 2\mu \frac{n^2 - 1}{n^2} \Psi - f_0(\vec{r}, t), \end{aligned} \quad (8.7)$$

where i' is defined as the direction opposite to i , i.e. that having $\vec{v}_{i'} = -\vec{v}_i$. When $\mu = 0$, the microdynamics becomes $f_i(\vec{r} + \Delta_t \vec{v}_i, t + \Delta_t) = -f_{i'}(\vec{r}, t)$. This corresponds to a perfect reflection on a mirror site, that is the flux bounces back to where they came from with a change of sign. This is a way to define a boundary condition by tuning the parameter μ on some selected sites.

Since Eq. (8.7) is linear, it can also be expressed using a matrix formulation $f_i(\vec{r} + \Delta_t \vec{v}_i, t + \Delta_t) = \sum_j W_{ij} f_j(\vec{r}, t)$. However, from the point of view of a numerical implementation, Eq. (8.7) implies less computation.

Figure 65 (left) shows a simulation (D2Q5) of Eq. (8.7) in a situation where two media are present. A plane wave is produced in medium M_1 by forcing a sine oscillation for the f_i 's on some vertical line. The wave propagates at speed c_0 till it penetrates in medium M_2 which has the shape of a convex lens. There, propagation speed is set to $c < c_0$. The shape of the lens naturally produces a focusing of the energy when the wave re-enters medium M_1 . In these simulation, $\mu = 1$.

An example of a wave reflected on a parabolic mirror is shown in Fig. 65 (right). Each lattice site in the black region is a perfect reflector with $\mu = 0$. As a result of the collective effect of these mirror sites, we observe that the incoming plane wave concentrates at the focal point of the parabola.

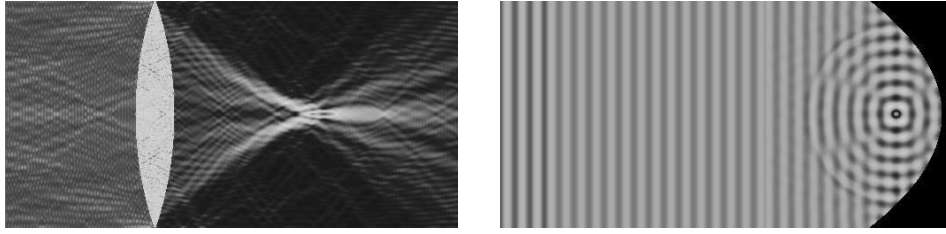


Fig. 65. Simulation with the LB wave model: focusing of light by a convex lens where the propagation speed is smaller than in vacuum (left). Focusing by a parabolic mirror (right).

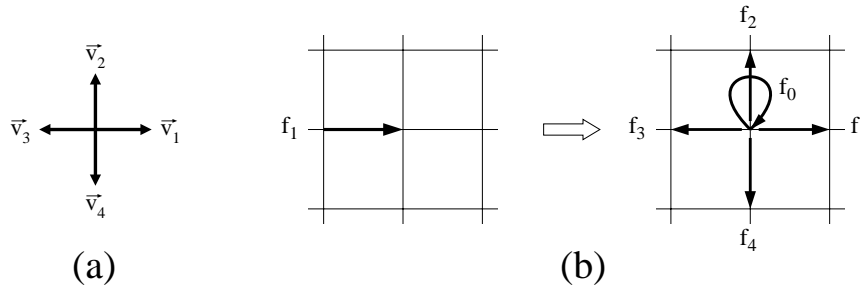


Fig. 66. Scattering of an incoming flux $f_1 = 1$ at a D2Q5 lattice site, according to Eq. (8.7).

A natural interpretation of our LB wave model is to assume that the f_i 's represent some physical fields (a local deformation or deviation from an equilibrium state). These fields propagate on the lattice and are scattered when reaching a site as illustrated in Fig. 66.

The idea of expressing wave propagation as a discrete formulation of the Huygens principle has been considered by several authors [47, 85, 88, 175]. Not surprisingly, the resulting numerical schemes bear a strong similarity to ours. Nevertheless the context of these studies is different from ours and none have noticed the existing link with the lattice BGK approach. Models of Refs. 47 and 175 use a reduced set of conserved quantities, which may not be appropriate in our case. Other models [123, 145] consider wave propagation in a LB approach, but with a significantly more complicated microdynamics and a different purpose.

8.2. Application to mobile communications

The above LB wave model can be used to compute the wave intensity pattern in a system with complicated boundary conditions. Here we consider the problem of predicting the intensity of a wave propagating in a city. This application is relevant to the field of cellular phone and mobile communication devices.

An efficient planning of the deployment of wireless communication networks is based on accurate predictions of radio-wave propagation in urban environments.

Radio waves are absorbed, reflected, diffracted and scattered in a complicated way on the buildings and this constitutes a difficult propagation problem which is studied by various authors [9, 104, 150] and is beyond analytical calculation. Yet, the coverage region of an antenna is a crucial question because the base stations must be placed in appropriate locations so that a complete coverage is guaranteed with a minimum number of cells, each of them no larger than what is allowed by traffic or propagation requirements.

The LB model presented in the previous section (with $n = 1$) produces fast and accurate predictions of the wave propagation in urban environment [40]. The procedure starts by discretizing the building layout by, for example, scanning a city map. Depending on the nature of each pixel (building or not), a different set of coefficients is defined for the microdynamics of the f_i . The value is chosen appropriately after comparison with real measurements performed by Swisscom. A source wave of wave length Λ is simulated at site \vec{r} by imposing a $A(\vec{r}) \sin(2\pi t/T)$ for the $f_i(\vec{r}, t)$ where $T = c/\Lambda$ is the period and $A(\vec{r})$ some chosen amplitude.

The simulation then consists of a synchronized updating of each site, according to the LB microdynamics until a steady state of the signal intensity (defined as the amplitude of Ψ) is reached. A re-normalization scheme $\Psi' = \mathcal{R}(\delta, \Lambda/\Lambda_0)\Psi$ must be then applied in order to account for the three-dimensional geometry of the real propagation problem, and the possibly wrong wavelength Λ chosen for numerical reasons (the wavelength must be large compared to the lattice spacing). In the function \mathcal{R} , the quantity δ is the distance to the source depending on the layout (see Ref. 40) and Λ_0 is the real wavelength concerned by the prediction.

Figure 67 shows a typical simulation of the wave intensity pattern produced by a transmitter located in an urban area. The predictions of the LB model and the renormalization procedure are in good agreements with the corresponding real measurements performed by Swisscom in the real environment.

8.3. Modeling solid body

Whereas LB methods have been largely used to simulate systems of point particles which interact locally, modeling a solid body with this approach (i.e. modeling an object made of many particles that maintains its shape and coherence over distances much larger than the interparticle spacing) has remained mostly unexplored. A successful attempt to model a *one-dimensional* solid as a cellular automata is described in Ref. 30. The crucial ingredient of this model is the fact that collective motion is achieved because the “atoms” making up the solid vibrate in a coherent way and produce an overall displacement. This vibration propagates as a wave throughout the solid and reflects at the boundary.

A 2-D solid-body can be thought of as a square lattice of particles linked to their nearest neighbors with a spring-like interaction. Generalizing the model given in Ref. 30 requires us to consider this solid as made up of two sublattices. We term them black and white, by analogy to the checkerboard decomposition. The

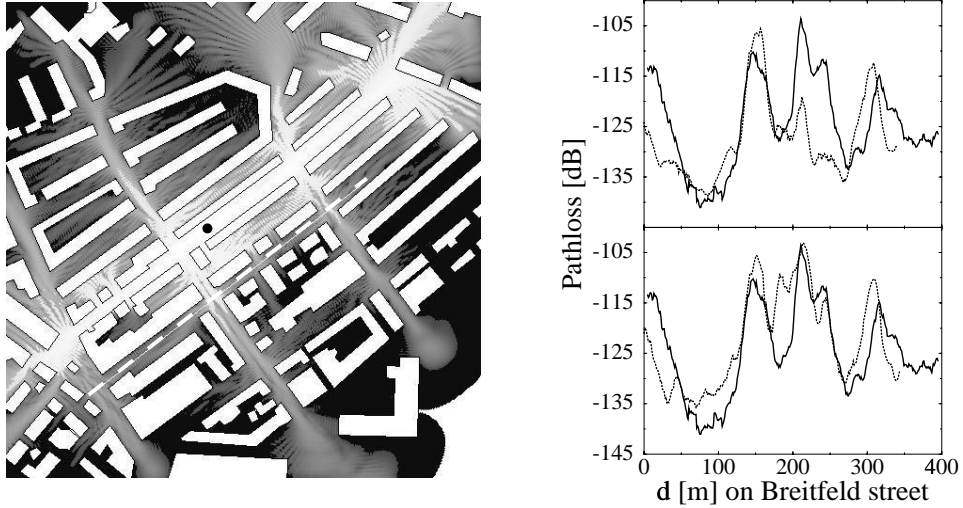


Fig. 67. LB simulation of wave propagation in the city of Bern on a square lattice of size 512×512 . The white blocks represent the buildings, the gray levels indicates the simulated intensity of the wave (decreasing from white to black) and the dot marks the position of the source. The plots show the measured and computed intensity along the street which is indicated by the dotted white line. Two types of boundary conditions were applied for the sites limiting the buildings in the discretized layout: *reflecting* walls in the upper graph and *permeable* walls in the lower graph.

dynamics consists in moving the black particles as a function of the positions of their white, motionless neighbors, and vice-versa, at every other step.

Let us denote the location of a black particle by $\vec{r}_{i,j} = (x_{i,j}, y_{i,j})$. The surrounding white particles will be at positions $\vec{r}_{i-1,j}$, $\vec{r}_{i+1,j}$, $\vec{r}_{i,j-1}$ and $\vec{r}_{i,j+1}$. We define the separation to the central black particle as (see Fig. 68)

$$\begin{aligned}
 \vec{f}_1(i, j, t) &= \vec{r}_{i,j}(t) - (\vec{r}_{i-1,j}(t) + \vec{h}), \\
 \vec{f}_2(i, j, t) &= \vec{r}_{i,j}(t) - (\vec{r}_{i,j-1}(t) + \vec{u}), \\
 \vec{f}_3(i, j, t) &= \vec{r}_{i,j}(t) - (\vec{r}_{i+1,j}(t) - \vec{h}), \\
 \vec{f}_4(i, j, t) &= \vec{r}_{i,j}(t) - (\vec{r}_{i,j+1}(t) - \vec{u}),
 \end{aligned} \tag{8.8}$$

where the \vec{f}_i are now vector quantities, and $\vec{h} = (r_0, 0)$ and $\vec{u} = (0, r_0)$ can be thought of as representing the equilibrium length of the horizontal and vertical spring connecting adjacent particles. With this formulation, the coupling between adjacent particles is not given by the Euclidean distance but is decoupled along each coordinate axis (however, a deformation along the x -direction will propagate along the y -direction and conversely). This method makes it possible to work with a square lattice, which is usually not taken into account when describing deformation in a solid because, with the Euclidean distance, the y -axis can be tilted by an angle α without applying any force. The breaking of the rotational invariance is expected not to play a role in the fracture process we shall consider below.

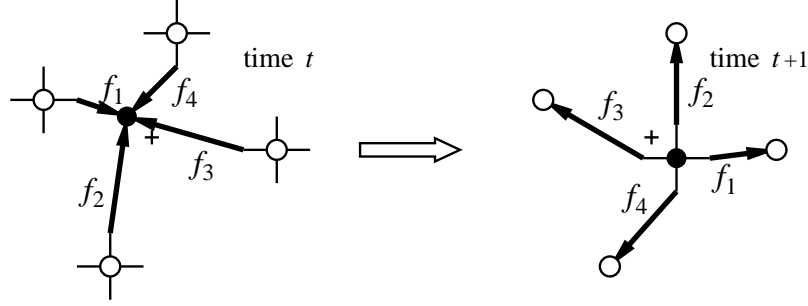


Fig. 68. Illustration of the way the f_i s are defined. The cross indicates the location of the geometrical center of mass of the four white particles. At the next iteration, the black particle jumps to a symmetrical position with respect to this point.

The locations $\vec{r}_{ij}(t+1)$ of the black particles is obtained by updating the corresponding \vec{f}_i s by Eq. (8.7), with $n = 1$ and for $i > 0$. Next, the quantities \vec{f} are interpreted as the deformations seen by the white particles,

$$\begin{aligned}\vec{f}_1(t+1) &= \vec{r}_{i+1,j} - (\vec{r}_{ij}(t+1) + \vec{h}), \\ \vec{f}_2(t+1) &= \vec{r}_{i,j+1} - (\vec{r}_{ij}(t+1) + \vec{u}), \\ \vec{f}_3(t+1) &= \vec{r}_{i-1,j} - (\vec{r}_{ij}(t+1) - \vec{h}), \\ \vec{f}_4(t+1) &= \vec{r}_{i,j-1} - (\vec{r}_{ij}(t+1) - \vec{u}).\end{aligned}\tag{8.9}$$

Then, the same procedure can re-applied to move the white particles.

It turns out that Eq. (8.7) (with $n = 1$ and $i \neq 0$) is equivalent to moving the particles to a symmetric location with respect to $(1/4)[\vec{r}_{i-1,j} + \vec{h} + \vec{r}_{i+1,j} - \vec{h} + \vec{r}_{i,j-1} + \vec{u} + \vec{r}_{i,j+1} - \vec{u}]$ (i.e. the center of mass of the neighbors, as shown in Fig. 68).

Indeed, in this case the new location of the particle will be

$$\vec{r}_{i,j}(t+1) = \vec{r}_{ij} + 2(\vec{r}_{CM} - \vec{r}_{ij}) = \frac{1}{2}[\vec{f}_1 + \vec{f}_2 + \vec{f}_3 + \vec{f}_4].\tag{8.10}$$

If this expression is substituted into Eq. (8.9), it is easy to check that, for instance,

$$\vec{f}_1(t+1) = \frac{1}{2}[\vec{f}_1 + \vec{f}_2 + \vec{f}_3 + \vec{f}_4] - \vec{f}_3\tag{8.11}$$

and similarly for $\vec{f}_2(t+1)$, $\vec{f}_3(t+1)$ and $\vec{f}_4(t+1)$. This shows that the dynamics given in Eq. (8.11) is identical to the LB wave model described in relation (8.7) for $n = 1$ and $f_0 = 0$.

The momentum \vec{p}_{ij} associated to the motion of particle (i, j) is then

$$\vec{p}_{ij} \equiv \vec{r}_{ij}(t+1) - \vec{r}_{ij}(t) = -\frac{1}{2}[\vec{f}_1 + \vec{f}_2 + \vec{f}_3 + \vec{f}_4]$$

which is the conserved quantity $\vec{\Psi}$ introduced in the LB wave model.

At the boundary of the domain a different rule of motion has to be considered since the particles may have less than four links. With the interpretation of the rule as a symmetrical motion with respect to

$$\vec{r}_{CM} = \frac{[(\vec{r}_{i-1,j} + \vec{h})n_e + (\vec{r}_{i+1,j} - \vec{h})n_w + (\vec{r}_{i,j-1} + \vec{u})n_s + (\vec{r}_{i,j+1} - \vec{u})n_n]}{(n_e + n_w + n_s + n_n)},$$

where n_e , n_w , n_s and n_n are Boolean variables indicating the presence or absence of a neighbor along the east, west, south and north directions, the evolution rule can be written down for particles missing some of their links, either because they are at the boundary of the domain or because some links are broken, as described below.

8.4. Fracture

An interesting application of our LB solid body model is the study of a fracture process. How things break is still an important problem in science for which one lacks a theory and no satisfactory understanding is yet achieved [114].

The key idea when using our approach as a model of a dynamic cracks is to assume that a bond linking two adjacent atoms may break if the local deformation exceeds some given threshold. This threshold can possibly be different for each bond and spatial disorder can be introduced in this way. Once a bond is broken, the atoms on each side of the crack behave as free ends. A broken link weakens the material because a local deformation can no longer be distributed uniformly among the four neighbors. Usually, the next bond to break is the nearest neighbor of an already broken bond.

A typical experiment which is performed when studying fracture formation is to apply a stress by pulling in opposite ways the left and right extremities of a solid sample. A small notch (artificially broken links) is made in the middle of the sample to favor the apparition of the fracture at this position. Once a given strain is reached, a crack forms and propagates from that notch through the bulk, breaking the system in one or multiple pieces. The fracture is perpendicular to the direction of the stress. This situation is illustrated in Fig. 69 where each dot shows the position of an atom.

The shape of the fracture we obtain is qualitatively similar to what is observed in real experiment [114]. Several situations can be reproduced, depending on the value of the model parameters. It is found that adding some attenuation in the motion (i.e. having $\mu < 1$) yields fractures with less branching. Figure 70 shows some of the simulation results. In Fig. 70(b) no damping of the wave is included while, in Fig. 70(a) a damping factor $\mu = 0.92$ is added. Figures 70(c) and 70(d) have less disorder than Figs. 70(a) and 70(b) in the sense that the breaking threshold varies weakly over space. The damping in Fig. 70(d) is $\mu = 0.91$, slightly stronger than in Fig. 70(c) ($\mu = 0.92$). The stretching rate (i.e the displacement of the solid boundary at each time step) is the same for all experiments. In the above simulations, once the fracture starts propagating, the external stress is turned off.

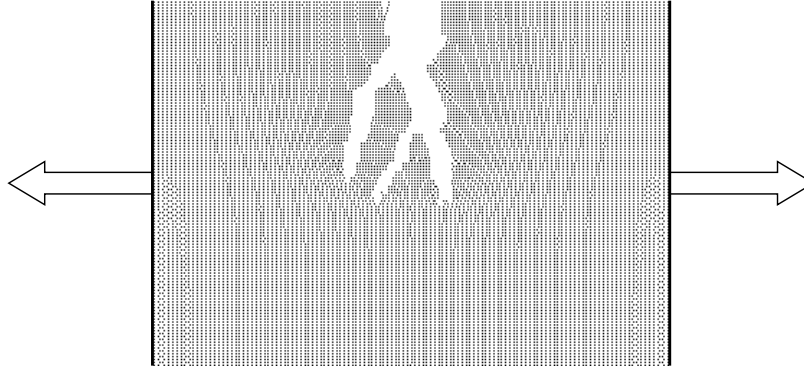


Fig. 69. Fracture simulation obtained in a LB solid with 128×128 atoms when applying an opposite force on both sides of the sample.

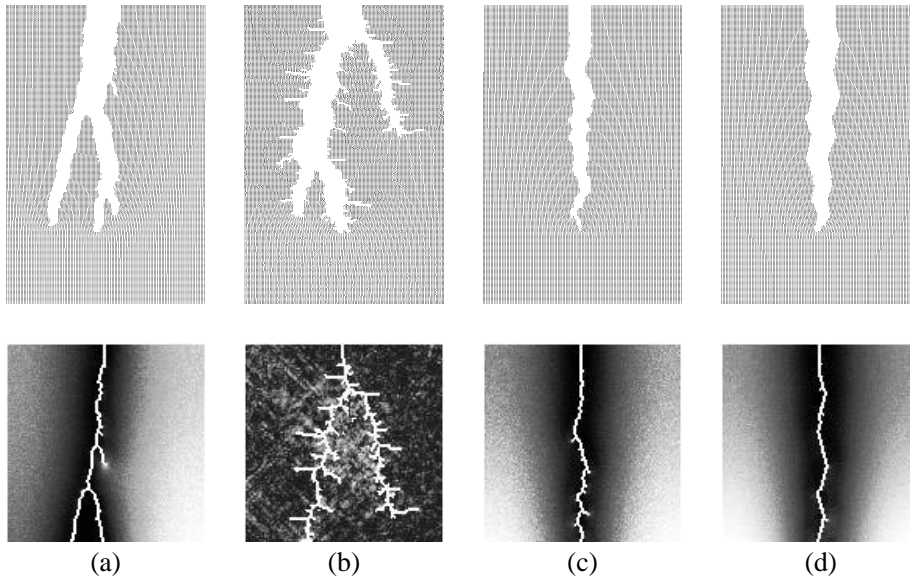


Fig. 70. Fracture (top) and the corresponding map of the broken bond (bottom) for several runs with different parameters.

We have measured the propagation speed of the fracture by recording the location of the crack tip $l(t)$ for each time step. In case of branching we consider the most advanced crack. Figure 71 shows the average velocity $v(t) = l(t)/t$ of the propagation fracture as a function of time. These measurements made from our simulation are in qualitative agreement with experimental data. In particular the crack speed is slower than the speed of sound (which is here $c_0 = 1/\sqrt{2}$ in lattice units) and it is faster when the fracture is complex.

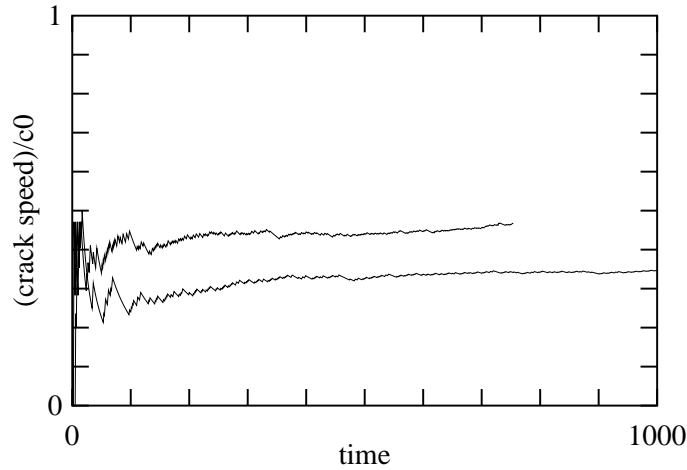


Fig. 71. Crack propagation speed measured in the LB fracture simulation. The upper and lower curves correspond to the fractures shown in Figs. 70(b) and 70(d), respectively.

8.5. Wave localization

In this section, we consider another problem for which the LB wave model is useful: propagation in disordered media. Our purpose is not to derive new physical properties but, rather, to show how the LB approach can be easily applied to study a difficult problem such as wave localization. Note also that this type of approach has been considered for this problem by other authors [175].

A coherent, but by no means complete understanding of the problem of waves in *disordered* media has only emerged recently [161]. Disordered media means here that the waves are supposed to undergo multiple scattering and the problem is quite different from the case of propagation in an urban medium, as considered in Sec. 8.2. The two problems are not logically separated but the treatment of radio wave propagation in urban areas involves obstacles with typical sizes much larger than the wavelength. Thus, it is rather a diffraction problem, involving departures from geometrical optics caused by the finite wavelength of the waves and actual scattering analysis enters the game only once the small scale roughness of the buildings or the corners are taken into account.

For the scattering of waves by systems whose characteristic sizes are small compared to the wavelength, it is convenient to think of the incident fields as inducing a response that oscillates in definite phase relationship with the incident wave and radiates energy in directions other than the direction of incidence. If the medium contains such randomly distributed small scatterers, the picture of multiple scattered waves is very different from, no more, that we normally associate with waves. Although the medium is a purely elastic, the wave can have a diffusive-like behavior or become localized, showing up no more spatial periodicity or possibility for transport.

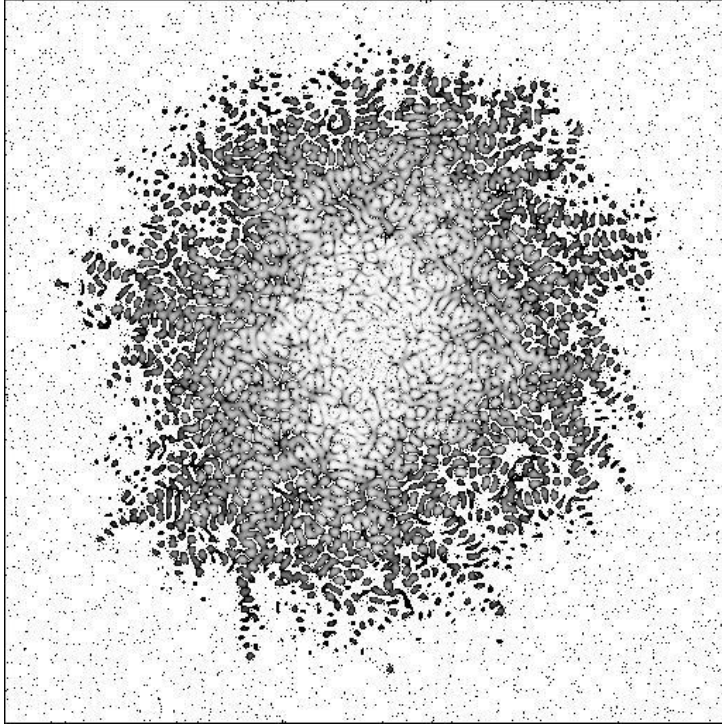


Fig. 72. Snapshot of energy propagation pattern in a random medium composed of a background of refraction index $n_0 = 1$ and containing 2% of randomly distributed scatterers (black dots), all with $n_1 = 10$. The source is placed at the center of the sample and oscillates with a period of 16 time steps. The pattern shows large fluctuations and the diffusive, or sub-diffusive, behavior only emerges after an averaging over the configurations.

Our wave propagation model is particularly well adapted to investigate numerically wave propagation in random media beyond what is analytically possible. Here we consider a two-dimensional medium with two different refraction indices n : the background sites have a value of $n_0 = 1$, whereas the randomly distributed scatterers have $n_1 > 1$.

Different media may be designed. For instance we could choose a different value of n for each scatterer, or even a different value of n for each lattice site. Figure 72 shows the typical pattern of energy issued from a point source located in a random medium composed of 2% of scatterers. Note that the dynamics of our model is time-reversal invariant and that the new propagation pattern we observe is not due to some form of dissipation.

The pattern shows large fluctuations and further analysis or comparison with classical diffusion involve an averaging over different spatial configurations. To avoid the excess of computation generated by an averaging process over successive configuration, we consider a two-dimensional system with a one-dimensional symmetry. The averaging is achieved by a reduction over the “irrelevant” dimension.

We consider the propagation of the energy issued from a “line-pulse” in a two-dimensional long strip-like medium (typically of size 4096×64). The line source is placed in the middle and radiates synchronously two oscillations of a wave with a given period $T = 6$. Two free parameters determine the medium: ρ the density of randomly distributed scatterers and n_1 the scattering strength, or refraction index of the scatterers.

In order to extract the propagation properties of a wave traveling in such a disorder media, we study the average behavior of the square root of the energy distribution second moment

$$\Pi(t) = \sqrt{\int A^2(\vec{r}, t) r^2 d^2 r},$$

where r is the distance to the source and A the amplitude of the wave at position \vec{r} . Thus Π is.

The results are shown in Fig. 73. It can be seen that for the homogeneous medium, a pure wave propagation is characterized, as expected, by $\Pi(t) \propto t$. For random non-dissipative media the dynamics switches to a behavior given by $\Pi(t) \propto \sqrt{t}$ which is typical of a diffusive transport regime. The cross-over is smooth and happens earlier in the case of increasing disorder, or increasing scattering strength.

For the sake of comparison we also show the behavior of $\Pi(t)$ in the case of true diffusion, with the model discuss in Sec. 6.3.2. However, for the diffusion case, Π must be changed: instead of the “energy” A^2 we take the local field value $\Psi = \sum_i f_i$. The good agreement between classical diffusion and wave diffusion (or weak localization) is shown in Fig. 73.

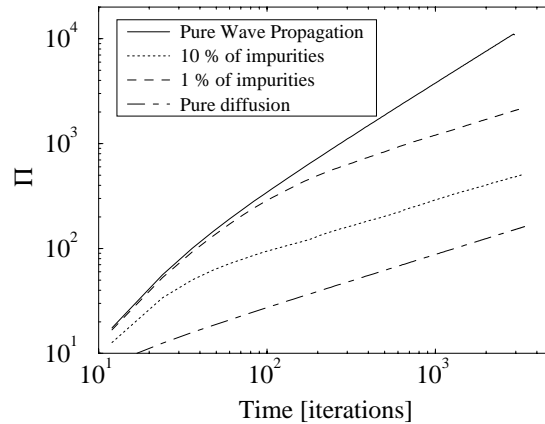


Fig. 73. Transition from the wave to the diffusive transport in a 1-dimensional geometry. The strip-like domain size is 4096×64 and the refraction index ratio of background sites over impurities is $1/10$. The square root of the second moment of the energy distribution Π is plotted as a function of time. Between the two extreme cases, homogeneous medium and pure diffusion, we observe a smooth transition for random media (1% and 10%) from the wave regime $\propto t$ to the diffusive regime $\propto t^{1/2}$.

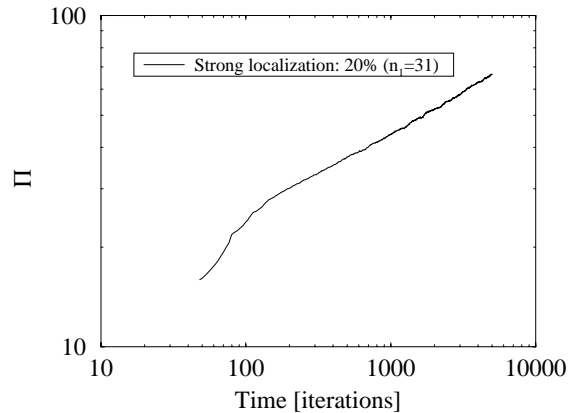


Fig. 74. Sub-diffusive (or localized) behavior obtained with a stronger disorder: $n_1 = 30$ and an impurity density of 20%. We have $\Pi \propto t^\alpha$ with $\alpha \approx 0.24$.

Strong localization is presented in Ref. 161 as a tendency for the diffusion coefficient to fall towards 0. The measurement of the quantity Π with a significant increase of the amount of disorder shows a behavior $\Pi \propto t^\alpha$ where $\alpha < 1/2$, as illustrated in Fig. 74.

It is interesting to note that, when the reflexion index n_1 is large, the scatterers behave as energy conserving reflectors (i.e. with $\mu = 0$ and $n = 1$ in Eq. (8.7)). Thus, each site has $\mu = 1$ with probability $1 - \rho$ and $\mu = 0$ with probability ρ . If the averaging process over propagation patterns is replaced by a spatial averaging of the disorder (i.e. the averaging is done before propagation is simulated), we obtain that the strong localization case behaves as a propagation in an absorbing media with $\mu = 1 - \rho$.

References

- [1] Aharonov, E. and Rothman, D., Non-Newtonian flow (through porous media): A lattice Boltzmann method, *Geophys. Res. Lett.* **20**, 679–682 (1993).
- [2] Alexander, F., Chen, S. and Sterling, J., Lattice Boltzmann thermohydrodynamics, *Phys. Rev.* **E47**, 2249–2252 (1993).
- [3] Antal, T., Droz, M., Magnin, J. and Rácz, Z., Derivation of the Matalon–Packer law for Liesegang pattern, *J. Chem. Phys.* (to appear).
- [4] Bahr, D. and Rundle, J., Theory of lattice Boltzmann simulation of glacier flow, *J. of Glaciology* **41**(139), 634–640 (1995).
- [5] Bandini, S., Serra, R. and Liverani, F. S. (eds.), *Cellular Automata Research Towards Industry* (Springer-Verlag, London, 1998).
- [6] Bandini, S. and Worsch, T. (eds.), *Theoretical and Practical Issues on Cellular Automata* (Springer-Verlag, London, 2001).
- [7] Banks, E., *Information Processing and Transmission in Cellular Automata*, Tech. rep. (MIT, 1971), MAC TR-81.
- [8] Ben-Naim, E., Redner, S. and Leyvraz, F., *Phys. Rev. Lett.* **70**, 1890 (1993).
- [9] Bertoni, H. L., Honcharenko, W., Maciel, L. R. and Xia, H., Uhf propagation prediction for wireless personal communications, *IEEE Proc.* **82**(9), 1333–1359 (1994).

- [10] Bhatnager, P., Gross, E. and Krook, M., A model for collision process in gases, *Phys. Rev.* **94**, 511 (1954).
- [11] Binder, K. and Heermann, D., *Monte Carlo Simulation in Statistical Physics* (Springer-Verlag, 1992).
- [12] Boghosian, B. and Collaborators (eds.), *Proceedings of the 7th Conference on Discrete Simulation of Fluid Dynamics*, Vol. 9, *Int. J. Mod. Phys. C.* (Oxford, 1998).
- [13] Boghosian, B., Coveney, P. and Emerton, A., A lattice-gas model of microemulsions, *Proceedings of the Royal Society of London* **452**, 1221–1250 (1996).
- [14] Boghosian, B., Yepez, J., Alexander, F. and Margolus, N., Integer lattice gases, *Phys. Rev.* **E55**, 4137–4147 (1997).
- [15] Bonetti, M., Noullez, A. and Boon, J.-P., Lattice gas simulation of 2-d viscous fingering, in *Cellular Automata and Modeling of Complex Physical Systems*, Manneville, P., Boccara, N., Vichniac, G. and Bideau, R. eds. Proceedings in Physics 46 (Springer Verlag, 1989), pp. 239–241.
- [16] Boon, J.-P. (ed.), Advanced research workshop on lattice gas automata theory, implementations, and simulation, *J. Stat. Phys.* **68**(3/4), 000 (1992).
- [17] Boon, J.-P., Dab, D., Kapral, R. and Lawniczak, A., Lattice gas automata for reactive systems, *Phys. Rep.* **273**, 55–148 (1996).
- [18] Brieger, L. and Bonomi, E., A stochastic cellular automaton model of non-linear diffusion and diffusion with reaction, *J. Comp. Phys.* **94**, 467–486 (1991).
- [19] Brito, R. and Ernst, M., Propagating staggered wave in cellular automata fluids, *J. Phys.* **A24**, 3331 (1991).
- [20] Broadwell, J., Shock structure in a simple discrete velocity gas, *Phys. Fluids* **7**, 1243 (1964).
- [21] Brørs, B., Numerical modeling of flow and scour at pipelines, *Journal of Hydraulic Engineering* **125**(5), 511–523 (1999).
- [22] Burks, A., Von neumann’s self-reproducing automata, in *Essays on Cellular Automata*, Burks, A. ed. (University of Illinois Press, 1970), pp. 3–64.
- [23] Cahn, J. and Hilliard, J., *J. Chem. Phys.* **28**, 258 (1958).
- [24] Calvin, P., d’Humières, D., Lallemand, P. and Pomeau, Y., Cellula automata for hydrodynamics with free boundaries in two and three dimensions, *C.R. Acad. Sci. Paris, II* **303**, 1169 (1986). Reprinted in *Lattice Gas Methods for Partial Differential Equations*, Doolen, G. ed. (Addison-Wesley, 1990), p. 415.
- [25] Chen, H., Chen, S. and Matthaeus, W., Recovery of Navier–Stokes equations using a lattice-gas Boltzmann method, *Phys. Rev.* **A45**, R5339–5342 (1992).
- [26] Chen, S., Diemer, K., Doolen, G., Eggert, K., Fu, C., Gutman, S. and Travis, B., Lattice gas automata for flow through porous media, *Physica* **D47**, 72–84 (1991).
- [27] Chen, Y. *et al.* (eds.), *The 9th International Conference on the Discrete Simulation of Fluid Dynamics, Tokyo, 1999*, Vol. 129, Computer Physics Communications (2000).
- [28] Chen, Y. and Ohashi, H., Several improvements on the lattice bgk simulation of fluid flows, in *Proceedings of the Discrete Simulation of Fluid* (1996).
- [29] Chen, Y., Ohashi, H. and Akiyama, M., Thermal lattice BGK model without non-linear deviations in macrodynamic equations, *Phys. Rev.* **E50**, 2776–2783 (1994).
- [30] Chopard, B., A cellular automata model of large scale moving objects, *J. Phys.* **A23**, 1671–1687 (1990).
- [31] Chopard, B. and Droz, M., Cellular automata approach to non-equilibrium phase transitions in a surface reaction model: Static and dynamic properties, *J. Phys.* **A21**, 205 (1987).

- [32] Chopard, B. and Droz, M., Cellular automata model for heat conduction in a fluid, *Phys. Lett.* **A126**, 476 (1988).
- [33] Chopard, B. and Droz, M., *Cellular Automata Modeling of Physical Systems* (Cambridge University Press, 1998).
- [34] Chopard, B., Droz, M., Cornell, S. and Frachebourg, L., Cellular automata approach to reaction-diffusion systems: theory and applications, in *Cellular Automata: Prospects in Astrophysical Applications*, Perdang, J. and Lejeune, A., eds. (World Scientific, 1993), pp. 157–186.
- [35] Chopard, B., Dupuis, A. and Luthi, P., A cellular automata model for urban traffic and its application to the city of Geneva, in *Traffic and Granular Flow '97*, Schreckenberg, M. and Wolf, D. eds. (Springer-Verlag, Singapore, 1998), pp. 153–168.
- [36] Chopard, B., Frachebourg, L. and Droz, M., Multiparticle lattice gas automata for reaction-diffusion systems, *Int. J. of Mod. Phys.* **C5**, 47–63 (1994).
- [37] Chopard, B., Herrmann, H. and Vicsek, T., Structure and growth mechanism of mineral dendrites, *Nature* **353**, 409–412 (1991).
- [38] Chopard, B., Luthi, P. and Droz, M., Microscopic approach to the formation of Liesegang patterns, *J. Stat. Phys.* **76**, 661–677 (1994).
- [39] Chopard, B., Luthi, P. and Droz, M., Reaction-diffusion cellular automata model for the formation of Liesegang patterns, *Phys. Rev. Lett.* **72**(9), 1384–1387 (1994).
- [40] Chopard, B., Luthi, P. and Wagen, J., A lattice Boltzmann method for wave propagation in urban microcells, *IEE Proceedings — Microwaves, Antennas and Propagation* **144**, 251–255 (1997).
- [41] Chopard, B., Luthi, P. O. and Queloz, P.-A., Cellular automata model of car traffic in two-dimensional street networks, *J. Phys.* **A29**, 2325–2336 (1996).
- [42] Chopard, B., Masselot, A. and Droz, M., A multiparticle lattice gas model for a fluid. application to ballistic annihilation, *Phys. Rev. Lett.* **81**, 1845–1848 (1998).
- [43] Chopard, B., Masselot, A. and Dupuis, A., A lattice gas model for erosion and particles transport in a fluid, in *Proceedings of the LGA '99 Conference*, Tokyo, Vol. 129, Y. C. *et al.* ed., Computer Physics Communications (2000), pp. 167–176.
- [44] Cornell, S., Droz, M. and Chopard, B., Role of fluctuations for inhomogeneous reaction-diffusion phenomena, *Phys. Rev.* **A44**, 4826–32 (1991).
- [45] Cornell, S., Droz, M. and Chopard, B., Some properties of the diffusion-limited reaction $nA + mB \rightarrow C$ with homogeneous and inhomogeneous initial conditions, *Physica* **A188**, 322–336 (1992).
- [46] Cornille, H., Exact (2+1)-dimensional solutions for two discrete velocity Boltzmann models with four independent densities, *J. Phys.* **A20**, L1063–1067 (1987).
- [47] de Toro Arias, S. and Vanneste, C., A new construction for scalar wave equation in inhomogeneous media, *J. Phys. I France* **7**, 1071–1096 (1997).
- [48] Dee, G., Patterns produced by precipitation at a moving reaction front, *Phys. Rev. Lett.* **57**, 275–278 (1986).
- [49] d’Humières, D. and Lallemand, P., Lattice gas models for 3d hydrodynamics, *Europhys. Lett.* **2**, 291 (1986).
- [50] Doolen, G. (ed.), *Lattice Gas Method for Partial Differential Equations* (Addison-Wesley, 1990).
- [51] Doolen, G. and Al. (eds.), *The 10th International Conference on the Discrete Simulation of Fluid Dynamics*, Santa Fe, 2000, *J. Stat. Phys.* (2002), p. 107.
- [52] D’Ortona, U., Cieplak, M., Rybka, R. and Banavar, J., Two-color non-linear cellular automata: Surface tension and wetting, *Phys. Rev.* **E51**, 3718–3728 (1995).

- [53] Drossel, B. and Schwabl, F., Self-organized critical forest-fire model, *Phys. Rev. Lett.* **69**, 1629 (1992).
- [54] Droz, M., Magnin, J., Zrinyi, M. and Chopard, B., Effect of dissociation on Liesegang systems, *J. Phys. Chem.* (1999).
- [55] Dufiet, V. and Boissonnade, J., Conventional and unconventional turing patterns, *J. Chem. Phys.* **96**, 664 (1991).
- [56] Dupuis, A., *Simulateur Micro-Cellulaire Parallèle de Trafic Routier Urbain et Application à la Ville de Genève*, Tech. rep., CUI (University of Geneva, 1997), master disertation.
- [57] Dupuis, A., *From a Lattice Boltzmann Model to a Parallel and Reusable Implementation of a Virtual River*, PhD thesis, CUI (University of Geneva, 1211 Geneva 4, Switzerland, 2002).
- [58] Dupuis, A. and Chopard, B., Lattice gas modeling of scour formation under submarine pipelines, *J. Comp. Phys.* (2001), submitted.
- [59] Dupuis, A. and Chopard, B., Lattice gas modeling of scour formation under submarine pipeline, *J. Comp. Physics* **178**, 161–174 (2002).
- [60] Elskens, Y. and Frisch, H., *Phys. Rev.* **A31**, 3812 (1985).
- [61] Farmer, D., Toffoli, T. and Wolfram, S. (eds.), *Cellular Automata, Proceedings of an Interdisciplinary Workshop*, Physica D (Los Alamos, North-Holland, 1984), Vol. 10.
- [62] Ferrante, A., Karlin, I. and Öttinger, H., Perfect entropy functions of the lattice Boltzmann method, preprint (1999).
- [63] Filippova, O., Succi, S., Mazzocco, F., Arrighetti, C., Bella, G. and Hnel, D., Multi-scale lattice Boltzmann schemes with turbulence modeling, *J. Comput. Phys.* **170**, 812–829 (2001).
- [64] Fisch, R., Gravner, J. and Griffeath, D., Threshold-range scaling of excitable cellular automata, *Statistics and Computing* **1**, 23 (1991).
- [65] Flekkoy, E., Lattice BGK models for miscible fluids, *Phys. Rev.* **E47**, 4247–4257 (1993).
- [66] Frisch, U., d’Humières, D., Hasslacher, B., Lallemand, P., Pomeau, Y. and Rivet, J.-P., Lattice gas hydrodynamics in two and three dimension, *Complex Systems* **1**, 649–707 (1987). Reprinted in *Lattice Gas Methods for Partial Differential Equations*, Doolen, G. ed. (Addison-Wesley, 1990), p. 77.
- [67] Frisch, U., Hasslacher, B. and Pomeau, Y., Lattice-gas automata for the Navier–Stokes equation, *Phys. Rev. Lett.* **56**, 1505 (1986).
- [68] Galam, S., Social paradoxes of majority rule voting and renormalization group, *J. Stat. Phys.* **61**, 943–951 (1990).
- [69] Galam, S., Chopard, B., Masselot, A. and Droz, M., Competing species dynamics: Qualitative advantage versus geography, *Eur. Phys. J.* **B4**, 529–531 (1998).
- [70] Garboczi, E., Permeability, diffusivity and microstructural parameters: A critical review, *Cement and Concrete Res.* **20**, 591–601 (1990).
- [71] Gardner, M., The fantastic combinations of John Conway’s new solitaire game life, *Scientific American* **220**, 120 (1970).
- [72] Gravner, J. and Griffeath, D., Threshold grouse dynamics, *Trans. Amer. Math. Soc.* **340**, 837 (1993).
- [73] Grosfil, P., Boon, J.-P. and Lallemand, P., Spontaneous fluctuation correlation in thermal lattice gas automata, *Phys. Rev. Lett.* **68**, 1077 (1992).
- [74] Grunau, D., Chen, S. and Eggert, K., A lattice Boltzmann model for multi-phase fluid flows, *Phys. Fluids* **A5**, 2557–2562 (1993).
- [75] Grunau, D., Lookman, T., Chen, S. and Lapedes, A., Domain growth, wetting and scaling in porous media, *Phys. Rev. Lett.* **71**, 4198–4201 (1993).

- [76] Gunstensen, A., Rothman, D., Zaleski, S. and Zanetti, G., Lattice Boltzmann model of immiscible fluids, *Phys. Rev.* **A43**, 4320–4327 (1991).
- [77] Gunton, J. and Droz, M., *Introduction to the Theory of Metastable and Unstable States* (Springer Verlag, 1983).
- [78] Guo, Z., Zheng, C. and Shi, B., Discrete lattice effects on forcing terms in the lattice Boltzmann method, *Phys. Rev.* **E65**, 046308 (2002).
- [79] He, X. and Luo, L.-S., Lattice Boltzmann model for the incompressible Navier–Stokes equation, *J. Stat. Phys.* **88**, 927–944 (1997).
- [80] He, X. and Luo, L.-S., *A priori* derivation of the lattice Boltzmann equation, *Phys. Rev.* **E55**, R6333–R6336 (1997).
- [81] Hensch, H. K., *Crystals in Gels and Liesegang Rings* (Cambridge University Press, 1988).
- [82] Hensch, H. K., *Periodic Precipitation* (Pergamon Press, 1991).
- [83] Higuera, F., Jimenez, J. and Succi, S., Boltzmann approach to lattice gas simulations, *Europhys. Lett.* **9**, 663 (1989).
- [84] Higuera, F., Jimenez, J. and Succi, S., Lattice gas dynamics with enhanced collision, *Europhys. Lett.* **9**, 345 (1989).
- [85] Hoeffler, W. J. R., The transmission-line matrix method. theory and applications, *IEEE Trans. on Microwave Theory and Techniques MTT-33*, Vol. 10 (Oct. 1985), pp. 882–893.
- [86] Holme, R. and Rothman, D., Lattice gas and lattice Boltzmann models of miscible fluids, *J. Stat. Phys.* **68**, 409–429 (1992).
- [87] Hou, S., Sterling, J., Chen, S. and Doolen, G., A lattice Boltzmann subgrid model for high Reynolds number flows, *Fields Institute Communications* **6**, 151–166 (1996).
- [88] Hrgovčić, H. J., Discrete representation of the n -dimensional wave equation, *J. Phys.* **A25**, 1329–1350 (1991).
- [89] Inamuro, T., Yoshino, M. and Ogino, F., A non-slip boundary condition for lattice Boltzmann simulations, *Phys. Fluids* **7**(12), 2928–2930 (1995).
- [90] I.S.I. and Monaco, R. (eds.), *Discrete Kinetic Theory, Lattice Gas Dynamics and Foundations of Hydrodynamics* (World Scientific, 1989).
- [91] Jablczynski, K., La formation rythmique des précipités: Les anneaux de Liesegang, *Bull. Soc. Chim. France* **33**, 1592 (1923).
- [92] Jackson, J., *Classical Electrodynamics* (John Wiley, 1975).
- [93] Jensen, B., Large-scale vortices in the wake of a cylinder placed near a wall, in *Second International Conference on Laser Anemometry — Advances and Applications* (Strathclyde, UK, September 1987), pp. 153–163.
- [94] Kadanoff, L., McNamara, G. and Zanetti, G., From automata to fluid flow: Comparison of simulation and theory, *Phys. Rev.* **A40**, 4527–4541 (1989).
- [95] Kandhai, D., *Large Scale Lattice Boltzmann Simulation: Computational Methods and Applications*, PhD thesis (University of Amsterdam, Amsterdam, The Netherlands, 1999).
- [96] Kapral, R. and Showalter, K. (eds.), *Chemical Waves and Patterns* Kluwer Academic, 1995).
- [97] Karapiperis, T. and Blankleider, B., Cellular automata model of reaction-transport process, *Physica* **D78**, 30–64 (1994).
- [98] Karlin, I., Gorban, A., Succi, S. and Boffi, V., *Phys. Rev. Lett.* **81**, 6 (1998).
- [99] Károlyi, A. and Kertész, J., Hydrodynamics cellular automata for granular media, in *Proceeding of the 6th Joint EPS-APS International Conference on Physics Computing: PC '94*, Gruber, R. and Tomassini, M. eds. (1994), pp. 675–681.

- [100] Kárpáti-Smidróczki, E., Bki, A. and Zrinyi, M., Pattern forming precipitation in gels due to coupling of chemical reaction with diffusion, *Colloid. Polym. Sci.* **273**, 857–865 (1995).
- [101] Keener, J. and Tyson, J., The dynamics of scroll waves in excitable media, *SIAM Rev.* **34**, 1–39 (1992).
- [102] Kjeldsen, S., Gjörsvik, O., Bringaker, K. and Jacobsen, J., Local scour near offshore pipelines, in *Second International Conference on Port and Ocean Engineering under Arctic Conditions* (University of Iceland, Iceland, 1973), pp. 308–331.
- [103] Kobayashi, D., Studies of snow transport in low-level drifting snow, *Contributions from the Institute of Low Temperature Science Series A* **24**, 1–58 (1972).
- [104] Kürner, T., Cichon, D. J. and Wiesbeck, W., Concepts and results for 3d digital terrain-based wave propagation models: An overview, *IEEE Jour. on Selected Areas in Communications* **11**(7), 1002–1012 (1993).
- [105] Lallemand, P. and Luo, L.-S., Theory of the lattice Boltzmann method dispersion, dissipation, isotropy, Galilean invariance, and stability, *Phys. Rev.* **E61**, 6546–6562 (2000).
- [106] Lin, C.-L. and Lai, Y., Lattice Boltzmann method on composite grids, *Phys. Rev.* **E62**(2), 2219–2225 (2000).
- [107] Livi, R., Ruffo, S., Ciliberto, S. and Buiatti, M. (eds.), *Chaos and Complexity* (World Scientific, 1988).
- [108] Luthi, P., *Lattice Wave Automata: From Radio Wave to Fracture Propagation*, PhD thesis, Computer Science Department, University of Geneva, 24 rue General-Dufour, 1211 Geneva 4, Switzerland, 1998.
- [109] Luthi, P. O., Preiss, A., Ramsden, J. J. and Chopard, B., A cellular automaton model for neurogenesis in drosophila, *Physica* **D118**, 151–16 (1998).
- [110] Luthi, P. O., Ramsden, J. and Chopard, B., The role of diffusion in irreversible deposition, *Phys. Rev.* **E55**, 3111–3115 (1997).
- [111] Mange, D. and Tomassini, M. (eds.), *Bio-Inspired Computing Machines: Towards Novel Computational Architectures* (Press Polytechniques et Universitaires Romandes, 1998).
- [112] Manneville, P., Boccara, N., Vichniac, G. and Bideau, R. (eds.), *Cellular Automata and Modeling of Complex Physical Systems*, Proceedings in Physics 46 (Springer Verlag, 1989).
- [113] Mao, Y., Seabed scour under pipelines, in *Seventh International Conference on Offshore Mechanics and Arctic Engineering* (Houston, Texas, February 1988), pp. 33–38.
- [114] Marder, M. and Fineberg, J., How things break, *Physics Today* (September 1996), pp. 24–29.
- [115] Martis, N. and Chen, H., Simulation of multicomponent fluids in complex 3d geometries by the lattice Boltzmann method, *Phys. Rev.* **E53**, 743–749 (1996).
- [116] Masselot, A., *A New Numerical Approach to Snow Transport and Deposition by Wind: A Parallel Lattice Gas Model*, PhD thesis, CUI, University of Geneva, 1211 Geneva 4, Switzerland, 2000.
- [117] Masselot, A. and Chopard, B., A lattice Boltzmann model for particle transport and deposition, *Europhys. Lett.* **42**, 259–264 (1998).
- [118] Masselot, A. and Chopard, B., Snow transport and deposition: A numerical model, *J. of Glaciology* (1998), submitted.
- [119] Matalon, R. and Packter, A., *J. Colloid Sci.* **10**, 46 (1955).
- [120] Mathur, B. and Ghosh, S., Liesegang rings-part I: Revert system of Liesegang rings, *Kolloid-Zeitschrift* **159**, 143 (1958).

- [121] McNamara, G. and Zanetti, G., Use of the Boltzmann equation to simulate lattice-gas automata, *Phys. Rev. Lett.* **61**, 2332–2335 (1988).
- [122] Mei, R., Luo, L.-S. and Shyy, W., An accurate curved boundary treatment in the lattice Boltzmann method, *Journal of Computational Physics* **155**, 307–330 (1999).
- [123] Mora, P., Lattice Boltzmann phonic lattice model, *J. Stat. Phys.* **68**, 591–609 (1992).
- [124] Muray, J., *Mathematical Biology* (Springer-Verlag, 1990).
- [125] Nagel, K. and Herrmann, H., Deterministic models for traffic jams, *Physica* **A199**, 254 (1993).
- [126] Nagel, K. and Schreckenberg, M., Cellular automaton model for freeway traffic, *J. Physique I (Paris)* **2**, 2221 (1992).
- [127] Naitoh, T., Ernst, M. and Dufty, J., Long-time tails in two-dimensional cellular automata fluids, *Phys. Rev.* **A42**, 7187 (1990).
- [128] Nakasian, A. and Karlin, I., private communication (1999).
- [129] Nannelli, F. and Succi, S., *J. Stat. Phys.* **68**, 401 (1992).
- [130] Nie, X., Qian, Y.-H., Doolen, G. and Chen, S., Lattice Boltzmann simulation of the two-dimensional Rayleigh-Taylor instability, *Phys. Rev.* **E58**, 6861–6864 (1998).
- [131] Orszag, S. and Yakhot, V., Reynolds number scaling of cellular automata hydrodynamics, *Phys. Rev. Lett.* **56**, 1691–1693 (1986).
- [132] Ostwald, W., *Lehrbuch der Allgemeinen Chemie* (Engelman, Leipzig, 1897).
- [133] Pearson, J. E., Complex patterns in a simple system, *Science* **261**, 189–192 (1993).
- [134] Peng, G. and Herrmann, H., Density waves of granular flow in a pipe using lattice-gas automata, *Phys. Rev.* **E49**, R1796–R1799 (1994).
- [135] Peng, G., Xi, H., Duncan, C. and Chou, S.-H., Lattice Boltzmann method on irregular meshes, *Phys. Rev.* **E58**, R4124–R4127 (1998).
- [136] Peng, G., Xi, H., Duncan, C. and Chou, S.-H., Finite volume scheme for the lattice Boltzmann method on unstructured meshes, *Phys. Rev.* **E59** (1999), to appear.
- [137] Perdang, J. and Lejeune, A. (eds.), *Cellular Automata: Prospect in Astrophysical Applications* (World Scientific, 1993).
- [138] Piasecki, J., *Echelles de temps multiples en théories cinétique*, Cahiers de physique, Press polytechniques et universitaire romandes (1997).
- [139] Pires, A., Landau, D. and Herrmann, H. (eds.), *Computational Physics and Cellular Automata* (World Scientific, 1990).
- [140] Prager, S., Periodic precipitation, *J. Chem. Phys.* **25**, 279 (1956).
- [141] Press, W., Flannery, B., Teukolsky, S. and Vetterling, W., *Numerical Recipes: The Art of Scientific Computing* (Cambridge University Press, 1989).
- [142] Propp, J., Trajectory of generalized ants, *Math. Intelligencer* **16**(1), 37–42 (1994).
- [143] Qian, Y., d’Humières, D. and Lallemand, P., Lattice BGK models for Navier–Stokes equation, *Europhys. Lett.* **17**(6), 470–84 (1992).
- [144] Qian, Y., Succi, S. and Orszag, S., Recent advances in lattice Boltzmann computing, in *Annual Reviews of Computational Physics III*, Stauffer, D. ed. (World Scientific, 1996), pp. 195–242.
- [145] Qian, Y.-H. and Deng, Y., A lattice bgk model for viscoelastic media, *Phys. Rev. Lett.* **79**, 2742–2745 (1997).
- [146] Reggia, A., Armentrout, S., Chou, H.-H. and Peng, Y., Simple systems that exhibit self-directed replication, *Science* **259**, 1282 (1993).
- [147] Renda, A., Bella, G., Succi, S. and Karlin, I., Thermohydrodynamic lattice BGK schemes with non-perturbative equilibria, *Europhys. Lett.* **41**, 279–283 (1998).
- [148] Rey, P., Droz, M. and Piasecki, J., *Phys. Rev.* **E57**, 138–145 (1998).
- [149] Rey, P., Frachebourg, L., Droz, M. and Piasecki, J., *Phys. Rev. Lett.* **75**, 160 (1995).

- [150] Rizk, K., Wagen, J.-F. and Gardiol, F., Ray tracing based path loss prediction in two microcellular environments, in *Proceedings IEEE PIMRC'94* (The Hague Netherlands, Sept. 1994), pp. 210–214.
- [151] Rosensweig, R., Magnetic fluids, *Scientific American* 124–132 (1982).
- [152] Rothman, D., Immiscible lattice gases: new results, new models, in *Cellular Automata and Modeling of Complex Physical Systems*, Manneville, P., Boccara, N., Vichniac, G. and Bideau, R. eds., *Proceedings in Physics* 46 (Springer Verlag, 1989), pp. 206–231.
- [153] Rothman, D. and Keller, J., Immiscible cellular automaton fluids, *J. Stat. Phys.* **52**, 275–282 (1988).
- [154] Rothman, D. and Zaleski, S., Lattice-gas models of phase separation: Interface, phase transition and multiphase flows, *Rev. Mod. Phys.* **66**, 1417–1479 (1994).
- [155] Rothman, D. and Zaleski, S., *Lattice-Gas Cellular Automata: Simple Models of Complex Hydrodynamics*, Collection Aléa (Cambridge University Press, 1997).
- [156] Schadschneider, A. and Schreckenberg, M., Cellular automaton models and traffic flow, *J. Phys.* **A26**, L679 (1993).
- [157] Schnackenberg, J., Simple chemical reaction systems with limit cycle behaviour, *J. Theor. Biol.* **81**, 389 (1979).
- [158] Schreckenberg, M., Schadschneider, A., Nagel, K. and Ito, N., Discrete stochastic models for traffic flow, *Phys. Rev.* **E51**, 2939 (1995).
- [159] Selkov, E., Self-oscillation in glycolysis: A simple kinetic model, *Eur. J. Biochem.* **4**, 79 (1968).
- [160] Shan, X. and Chen, H., Simulation of non-ideal gases and liquid-gas phase transitions by the lattice Boltzmann equation, *Phys. Rev.* **E49**, 2941–2948 (1994).
- [161] Sheng, P., *Introduction to Wave Scattering, Localization, and Mesoscopic Phenomena* (Academic Press, 1995).
- [162] Smagorinsky, J., General circulation experiments with the primitive equations: I. The basic equations, *Mon. Weather Rev.* **91**, 99–164 (1963).
- [163] Smith, D., On Ostwald's supersaturation theory of rhythmic precipitation (Liesegang rings), *J. Phys. Chem.* **81**, 3102 (1984).
- [164] Stewart, I., The ultimate in anty-particle, *Scientific American*, 88–91 (1994).
- [165] Succi, S., *The Lattice Boltzmann Equation, For Fluid Dynamics and Beyond* (Oxford University Press, 2001).
- [166] Succi, S., Amati, G. and Benzi, R., *J. Stat. Phys.* **81**, 5 (1995).
- [167] Succi, S., Vergassola, M. and Benzi, R., Lattice-Boltzmann scheme for two-dimensional magnetohydrodynamics, *Phys. Rev.* **A43**, 4521 (1991).
- [168] Swift, M., Orlandini, E., Osborn, W. and Yeomans, J., Lattice Boltzmann simulations of liquid-gas and binary fluid systems, *Phys. Rev.* **E54**, 5051–5052 (1996).
- [169] Toffoli, T. and Margolus, N., *Cellular Automata Machines: A New Environment for Modeling* (The MIT Press, 1987).
- [170] Tolman, S. and Meakin, P., Off-lattice and hypercubic-lattice models for diffusion-limited aggregation in dimension 2–8, *Phys. Rev.* **A40**, 428–37 (1989).
- [171] Tritton, D., *Physical Fluid Dynamics* (Clarendon Press, 1988).
- [172] Trizac, E., private communication.
- [173] Turing, A., The chemical basis of morphogenesis, *Phil. Trans. Roy. Soc. London* **B237**, 37 (1952).
- [174] Ulam, S., Random processes and transformations, *Proc. Int. Congr. Math.* **2**, 264–275 (1952).
- [175] Vanneste, C., Sebbah, P. and Sornette, D., A wave automaton for time-dependent wave propagation in random media, *Europhys. Lett.* **17**, 715 (1992).

- [176] Vichniac, G., Simulating physics with cellular automata, *Physica* **D10**, 96–115 (1984).
- [177] Vicsek, T., *Fractal Growth Phenomena* (World Scientific, 1989).
- [178] Wagner, A., *Europhys. Lett.* **44**, 144 (1998).
- [179] Weiss, G., Random walks and their applications, *American Scientist* **71**, 65 (1983).
- [180] Weiss, G. (ed.), *Contemporary Problems in Statistical Physics*, SIAM (1994).
- [181] Wells, J., Janecky, D. and Travis, B., A lattice gas automata model for heterogeneous chemical reaction at mineral surfaces and in pores network, *Physica* **D47**, 115–123 (1991).
- [182] Whitehouse, R., *Scour at Marine Structures* (Thomas Telford Publications, London, 1998).
- [183] Witten, T. and Sander, L., Diffusion-limited aggregation, *Phys. Rev.* **B27**, 5686 (1983).
- [184] Wolf, D. and Collaborator (eds.), *Traffic and Granular Flow '97*, Springer (to appear).
- [185] Wolf, D., Schreckenberg, M. and Bachem, A. (eds.), *Traffic and Granular Flow* (World Scientific, 1996).
- [186] Wolf-Gladrow, D. A., *Lattice-Gas Cellular Automata and Lattice Boltzmann Models: An Introduction*, Lecture Notes in Mathematics, 1725 (Springer, Berlin, 2000).
- [187] Wolfram, S., Cellular automaton fluid: Basic theory, *J. Stat. Phys.* **45**, 471 (1986).
- [188] Wolfram, S., *Theory and Application of Cellular Automata* (World Scientific, 1986).
- [189] Wolfram, S., *Cellular Automata and Complexity* (Addison-Wesley, Reading, Massachusetts, 1994).
- [190] Yukawa, S., Kikuchi, M. and Tadaki, S., Dynamical phase transition in one-dimensional traffic flow model with blockage, *J. Phys. Soc. Jpn.* **63**(10), 3609–3618 (1994).
- [191] Zanetti, G., Hydrodynamics of lattice-gas automata, *Phys. Rev.* **A40**, 1539–1548 (1989).
- [192] Zeldovitch, Y., Barrenblatt, G. and Salganik, R., The quasi-periodical formation of precipitates occurring when two substances diffuse into each other, *Sov. Phys. Dokl.* **6**, 869 (1962).
- [193] Ziff, R., Fichthorn, K. and Gulari, E., Cellular automaton version of the ab_2 reaction model obeying proper stoichiometry, *J. Phys.* **A24**, 3727 (1991).
- [194] Ziff, R., Gulari, E. and Barshad, Y., Kinetic phase transitions in an irreversible surface-reaction model, *Phys. Rev. Lett.* **56**, 2553 (1986).
- [195] Zou, Q., Hou, S., Chen, S. and Doolen, G., An improved incompressible lattice Boltzmann model for time-independent flows, *J. Stat. Phys.* **81**, 35–49 (1995).